POLITECNICO DI MILANO

Scuola di Ingegneria Industriale e dell' Informazione
Corso di Laurea Magistrale in Ingegneria Fisica

Charge Order Discommensurations and Fluctuations in Cuprate Superconductors studied by Resonant Inelastic X-ray Scattering

Relatore: Prof. Giacomo Claudio GHIRINGHELLI

Tesi di Laurea Magistrale di:
Giovanni DE VECCHI   852477

Anno Accademico 2016 - 2017

to Federica,

Contents

List of Figures

List of Tables

Abstract (Italiano)

Il seguente elaborato descrive, dal punto di vista sperimentale, l'ordine di carica nei cuprati superconduttivi. La peculiarità che contraddistingue i cuprati dai superconduttori BCS, è l'alta temperatura critica che caratterizza la transizione di fase allo stato superconduttivo in questi materiali. Dato che al momento una teoria in grado di descrivere in maniera esaustiva questo fenomeno di superconduttività anomala ancora non esiste, è necessario raccogliere più informazioni possibili riguardo la fenomenologia dei cuprati. In particolare, è dimostrato che l'ordine di carica è intimamente connesso con la superconduttività, essendo queste due fasi anti-correlate fra loro (ovvero i due stati di ordine competono fra loro). Inizialmente sono introdotti in breve i cuprati, caratterizzati da forti correlazioni elettrone e elettrone, e più nel dettaglio le onde di densità di carica e le differenze che le caratterizzano nelle diverse famiglie di cuprati. In seguito si discute una teoria basata sulla presenza di "discommensurazioni" nella fase del parametro d'ordine delle modulazioni di carica. La commistione tra questi salti di fase (le discommensurazioni) e domini dove invece la periodicità è commensurata al sottostante reticolo cristallino, possono essere responsabili del particolare valore assunto dal vettore d'onda medio dell'ordine di carica. Nello stesso capitolo vengono descritte delle simulazioni che ripercorrono e cercano poi di estendere, le conseguenze di salti di fase coerenti o meno fra i diversi domini dove la periodicità della modulazione è invece ben definita. Inoltre sono presentati dei modelli che cercano di riprodurre, in diverse condizioni, la relazione tra le immagini dello spazio reale, ottenute da misure STM, e le configurazioni di picchi nello spazio reciproco, che si ottengono mediante esperimenti di scattering. Nel capitolo successivo sono sottolineati gli aspetti fondamentali dello scattering risonante dei raggi x a bassa energia e viene sinteticamente descritta la strumentazione (in dotazione presso ID32 ad ESRF) utilizzata per compiere le misure descritte nel capitolo finale. Ivi sono presentati i risultati di un recente esperimento, volto alla ricerca della temperatura di "onset" dell'ordine di carica nel $NdBa_2Cu_3O_{6+\delta}$. I risultati ottenuti costituiscono un elemento di novità rispetto a quanto si ritiene comunemente essere l'origine dell'ordine di carica nei cuprati. Infatti i dati dimostrano che lo stato di pseudogap (che caratterizza la fermiologia dei cuprati un largo intervallo di drogaggi per temperature minori di T*) non è direttamente collegato con le modulazioni di carica, in quanto T* e la temperatura di onset non coincidono, diversamente da quanto invece suggerito da precedenti misure, che inducevano a pensare che l'ordine di carica fosse una conseguenza dello stato di pseudogap. Nel campione meno drogato dei due misurati, si può in aggiunta constatare la presenza di due picchi di carica di diversa natura che evolvono in maniera indipendente al cambiare della temperatura. Questi due aspetti emergenti dall'attenta analisi dei dati sperimentali, sono discussi in luce del lavoro teorico del gruppo del Professor Grilli. Nello stesso capitolo sono anche descritti la procedura e i metodi utilizzati per il trattamento dei dati sperimentali grezzi.

Abstract (English)

This thesis concentrates on the ordered phase, involving the charge degree of freedom, present in superconducting cuprates. Charge order appears, together with high temperature superconductivity, when the parent compounds are doped, both with electrons and with holes. These two ordered states compete, but at the same time they are intimately connected since experimental results demonstrate the ubiquitous character of charge order in superconducting cuprates. Therefore, it is of paramount importance the complete phenomenological description of electronic density modulations, to understand the real mechanism driving the pairing of electrons. The present work tackles the problem showing the results of simulations and of the analysis of experimental data. A brief introduction reports the main physical properties of cuprate parent compounds and the general features of charge order in this class of materials. The following chapter discusses the implications of a recent theory, which is based on the idea that the overall periodicity of the charge modulations, as measured by scattering probes, comes from the interplay at microscopic level of commensurate domains and localized phase defects: the "discommensurations". In particular, we focus on the relationship between the charge order pattern in the real space and the peaks it generates in the reciprocal space, in order to shed light on the link between the outcomes of the STM real space measurements and the output of diffraction and scattering experiments (like Resonant Inelastic X-ray Scattering, RIXS). I also briefly present the physical properties of the resonant x-rays scattering mechanism and the instrumentation used to perform this kind of experiments, in connection with the results presented in the final chapter, obtained in a recent experiment at the synchrotron radiation facility (ESRF, Grenoble). In this final part of the thesis, we discuss the motivations for this experiment, the methods employed for the analysis of the data and the consequences of the results achieved. The main reason pushing this research is the precise measurement of the onset temperature for the charge order in $NdBa_2Cu_3O_{6+\delta}$, defined as the temperature at which the charge order becomes visible. The unequalled resolution of the instrumentation used, gave us the possibility to detect charge order at higher temperatures than those usually reported in literature, in particular higher than the pseudogap temperature T* (defined as the temperature at which a peculiar gap opens in the in the spectrum of superconductive cuprates). This experimental finding is of paramount importance, since it challenges the theories based on the correlation between charge order and the pseudogap regime. Moreover, in the underdoped sample measured, two different kinds of peaks related to charge order are clearly visible: one peak is narrow and temperature dependent, while the other (displaced in the reciprocal space) is broad and almost temperature independent. These novel experimental results are discussed following the theoretical framework provided by the group of Prof. Grilli.

Sommario

L'elaborato seguente si concentra sull'ordine di carica presente nei cuprati. Questi materiali sono la famiglia più famosa di superconduttori ad alta temperatura critica e la ricerca su di essi è spinta non solo dall'interesse per la Fisica in sé e per sé ma anche da ovvie ragioni tecnologiche e applicative. L'ordine di carica, o modulazione della densità di carica, è un fenomeno esotico che vede la variazione periodica dell'occupazione degli stati elettronici di valenza. La sua scoperta non è legata ai cuprati, in quanto onde di densità di carica erano già note prima in altri materiali (come i dicalcogenoidi [1]), mentre la predizione teorica di questo fenomeno fisico risale agli anni 30 dello scorso secolo ad opera del fisico Rudolf Peierls [2]. Nei cuprati l'ordine di carica assume un carattere prettamente bidimensionale, essendo legato alla fisica 2D dei piani di CuO_2 che ospitano la superconduttività anomala. Alcuni ricercatori attribuiscono particolare importanza a queste modulazioni, ritenendo che esse siano il principale attore nel definire il diagramma di fase dei cuprati [3]. Infatti, alcune delle ragioni della loro importanza risiedono nel fatto che esse sono sempre presenti in tutti i superconduttori a base di ossido di rame, sia nel caso in cui vengano drogati con elettroni sia con buche. Inoltre superconduttività e ordine di carica sono intimamente legati, dato che competono fra loro ma allo stesso tempo sono presenti contemporaneamente in un intervallo di drogaggi molto esteso del diagramma di fase. Infine la relazione tra stato di pseudogap e onde di carica è una questione estremamente dibattuta, che questa tesi nel capitolo finale affronta in riferimento ai dati sperimentali raccolti nel mese di maggio a ESRF. In connessione con l'"ubiquità" dell'ordine di carica nei cuprati, è necessario precisare che in realtà esistono due manifestazioni di questo fenomeno, che possiedono caratteristiche diverse: da un lato abbiamo l'ordine a "strisce" di carica unidirezionali che si realizza nei composti a base di lantanio e è particolarmente intenso e dunque non troppo arduo da identificare (è questo il motivo per cui fu scoperto per primo attraverso esperimenti di diffrazione da neutroni [4]). Dall'altro lato la carica di valenza si organizza in maniera differente in tutte le altre famiglie di cuprati superconduttivi e la sua natura è in questo caso molto più elusiva. In effetti ci sono voluti diciassette anni, dopo la scoperta delle strisce, per ottenere una prova sperimentale diretta dell'ordine di carica in uno dei cuprati non a base di lantanio. Nello specifico la dimostrazione di questa altra faccia dell'ordine di carica, è dovuta al lavoro del gruppo del Prof. Ghiringhelli e del Prof. Braicovich sul $YBa_2Cu_3O_{6+\delta}$ [5], pubblicato nel 2012. Questa fondamentale scoperta non solo ha messo in luce la presenza di modulazioni di carica in una configurazione diversa dall'ordine a strisce, ma ha anche rinnovato l'interesse verso questo fenomeno fisico che di lì a poco altre misure sperimentali nelle altre classi di cuprati drogati, avrebbero dimostrato essere una caratteristica generale del diagramma di fase di questi materiali. È importante sottolineare che questa scoperta è stata possibile grazie all'utilizzo dello scattering risonante di raggi x a bassa energia dalla soglia di assorbimento L_3 del rame presente nei piani superconduttivi. Infatti l'utilizzo della risonanza consente di avere un'amplificazione di ordini di grandezza per il segnale proveniente dalla carica di valenza che forma queste modulazioni, cosa necessaria, dato che in condizioni non risonanti il rapporto tra segnale proveniente dalla modulazione di carica e quello proveniente dai livelli profondi imperturbati è

proporzionale al rapporto tra gli elettroni di valenza coinvolti (gli stati 2p dell'ossigeno) e il numero di cariche dello ione nel reticolo cristallino. Inoltre la compresenza in generale di ordine di carica e superconduttività indica il fatto che lo studio del primo è necessario alla completa descrizione del meccanismo di pairing superconduttivo.

In questa tesi contribuisco in due modi alla discussione attuale riguardo l'ordine di carica. In primo luogo presento delle simulazioni del parametro d'ordine nello spazio reale, analizzando la possibile compatibilità di un ordine di carica affetto da discommensurazioni di fase con le misure di microscopia e con i dati provenienti da misure di scattering di raggi x. A partire da questo lavoro preliminare traiamo delle importanti conseguenze che ci aiutano a capire la relazione tra le manifestazioni dell'ordine di carica nello spazio reale e nello spazio reciproco. In particolare, sfruttando il potente mezzo della trasformata di Fourier, grazie a queste simulazioni siamo in grado di discutere la connessione tra le misure nello spazio reale ottenute mediante STM e i pattern di picchi dello spazio reciproco misurati grazie al RIXS. Nella seconda parte dell'elaborato analizzo i recenti dati RIXS ottenuti da misure su due campioni di $NdBa_2Cu_3O_{6+\delta}$ al variare della temperatura. I trend sperimentali estratti a seguito dell'analisi dei dati sono poi confrontati con le predizioni teoriche del gruppo del Prof. Grilli e del Prof. Di Castro.

Questa tesi è basata su risultati sperimentali ottenuti presso la linea di luce ID32 dell'European Synchrotron (ESRF) a Grenoble, analizzati attraverso attenti fitting e simulazioni. Il capitolo 1 fornisce una breve presentazione della superconduttività ad alta temperatura critica nei cuprati, seguita da un più esaustivo excursus sull'ordine di carica nei cuprati. Il capitolo 2 discute, seguendo un recente articolo di Mesaros et al. [6], la teoria delle discommensurazioni di fase, come meccanismo in grado di giustificare il particolare valore della periodicità delle modulazioni di carica, e riporta alcune simulazioni computazionali riguardanti lo stesso argomento. Nella seconda parte dello stesso capitolo sono presentati i risultati di altri modelli volti a indagare l'effetto del confinamento spaziale sull'ordine di carica. Questo secondo tipo di simulazioni è mosso da alcuni dati RIXS ottenuti in gennaio 2017 ad ESRF. Il terzo capitolo tratta brevemente le proprietà fisiche e le peculiarità del RIXS alla soglia L_3 del rame, sia da un punto di vista sperimentale e fenomenologico, sia presentandone una possibile derivazione teorica. Nel medesimo capitolo viene anche descritto l'apparato strumentale necessario per attuare questa tecnica sperimentale, con particolare riferimento al nuovo strumento ERIXS (European-RIXS) attualmente in dotazione presso ID32 ad ESRF, completamente progettato dal gruppo del Prof. Ghiringhelli e Braicovich, del quale ho personalmente assistito al funzionamento durante la mia esperienza di tesi. Nel quarto ed ultimo capitolo sono discussi e presentati i risultati sperimentali introdotti poco sopra. Mi sono soffermato sulle motivazioni, ovvero la ricerca della temperatura di onset per le modulazioni di carica nel $NdBa_2Cu_3O_{6+\delta}$ e sulla descrizione del metodo utilizzato per l'analisi dei dati. I trend e le analisi effettuate sono lette in modo tale da evidenziare eventuali connessioni tra quanto suggerito dai nostri dati sperimentali e differenti spiegazioni teoriche.

Introduction

The present work focuses its attention on charge order in cuprates. Cuprates are the most famous family of high temperature superconductors and the research on these materials is spurred not only by the interest in their physics per se, but also by their obvious technological and engineering implications. Charge order or charge density modulation, is an exotic phenomenon, involving a periodic variation of the occupation of the valence electronic states. It was discovered in other materials (such as dichalcogenides [1]) before cuprates and first predicted by Rudolf Peierls in 1930s [2]. In cuprates this interesting phenomenon takes a bidimensional character, tightly connected to the CuO_2 planes physics. Some researchers argue that they actually "rule" [3] the phase diagram of superconducting cuprates. In fact, some of the reasons why this phenomenon is of paramount importance in this class of materials are: its competition with superconductivity, its ubiquitous presence throughout all the cuprate families (both hole and electron doped) and its possible relation with the pseudogap regime. Regarding the ubiquitous presence of this instability in cuprates, it must be pointed out that there exist two different manifestations of charge density waves. On one side, we have the stripe ordered La-based family of cuprates, in which charge order is present in the form of unidirectional "stripes". In this family, the charge density modulation is particularly strong, which helped the discovery [4]. On the other side, charge arranges in a different way in all other high-T_c superconducting cuprates and here the nature of this phenomenon is more elusive. In fact, it took about seventeen years from the discovery of stripe order, to achieve the first direct observation of charge order in another compound, not belonging to the 214 family. Specifically, the first direct proof of charge order different from stripes, came in 2012 by the group of Prof. Ghiringhelli and Prof. Braicovich, who discovered its presence in $YBa_2Cu_3O_{6+\delta}$ [5]. This experimental finding, which has been possible thanks to the unprecedented properties provided by Resonant Inelastic X-ray Scattering (RIXS), renewed the interest towards this ordering phenomenon and the discovery of charge instability in all other superconducting cuprates followed relatively quickly. The ubiquity of charge order among the copper-based superconductors stresses its intertwined character with high temperature superconductivity and also its relevance in order to understand the pairing mechanism leading to superconducting properties in CuO_2 planes. Thus, the complete understanding of charge order is essential to the ultimate comprehension of the anomalous superconductivity in copper oxides.

In this thesis, I contribute to the current study of charge order in cuprates in two ways. I present simulations of the real space order parameter analyzing the possible compatibility of a discommensurate charge density wave pattern with the microscopy and x-ray scattering data. From this preliminary work, we draw some useful insights about the relationship between the real space and the reciprocal space manifestations of this phenomenon. In particular, these simulations combined with the useful tool represented by the Fourier analysis, are useful to understand the link between data from STM measurements (probing directly the charge modulations in the real space) and those from RIXS (which as other scattering techniques, provides information in the momentum space). In the second part I analyze some recent RIXS data on $NdBa_2Cu_3O_{6+\delta}$

measured as function of the sample temperature and some previous results on YBCO. The experimental trends are then compared with theoretical predictions by Grilli and Di Castro.

This thesis is based on experimental results obtained at the beam line ID32 of the European Synchrotron (ESRF) in Grenoble, analyzed by careful fittings and simulations. Chapter 1 gives a brief phenomenological introduction of high temperature superconductivity in cuprates, followed by a more exhaustive discussion about the charge order phase, which appears upon doping the insulating antiferromagnetic parent compounds. Chapter 2 discusses, following a recent work by Mesaros et al. [6], the theory of phase locking discommensurations and reports the results of some computational simulations about this topic. In the second part of this chapter I show the outcomes of another set of simulations meant to assess the effect of confinement on charge order. This second work was motivated by some RIXS results obtained in January 2017 at ESRF. Chapter 3 presents in short, the resonant inelastic x-ray scattering process at the Cu-L_3 absorption edge, both from a theoretical and phenomenological point of view, highlighting the special properties that make this technique the most used probing mechanism for superconducting cuprates. I also briefly describe the experimental setup used during the experiment of May of this year at (ESRF), to which I participated. There, we put the accent on the characteristics of the new ERIXS (European-RIXS) spectrometer, designed by the group of Prof. Ghiringhelli and Prof. Braicovich at Politecnico di Milano. In the fourth and last chapter, we finally present the motivations, the analysis methods and the results of the experiment introduced above. In particular, we concentrate on the concept of "onset temperature" for the charge modulations in $NdBa_2Cu_3O_{6+\delta}$. In this chapter, I also present in short, the possible connections of our findings with the different theoretical explanations of charge instability in cuprates.

Chapter 1

Charge Density Waves in Cuprates

1.1 High Temperature Superconductivity

High Temperature Superconductivity (HTS) is a popular topic of condensed matter physics still searching for an answer. One (and possibly the most famous) class of materials where HTS takes place are cuprates, where it was first discovered by Bednorz and Muller in 1986 [7]. Cuprates comprehend different families of materials with an astonishing variety of new and mysterious properties, all sharing the common feature of CuO_2 planes where the high temperature superconductivity takes place. A theory explaining the phenomenology of HTS does not exist yet, thus experimental research trying to give the most complete picture of all the intertwined physical facts happening in cuprates is of paramount importance to shed light on its fundamental causes.

In this thesis, we will concentrate on cuprates. Regarding the experimental technique, among all the different methods providing useful information about these materials, we focus mainly on Resonant Inelastic X-ray Scattering (henceforth RIXS, whose properties are better discussed in chapter 3), which relies on a photon in – photon out probing mechanism. In particular, there are two different regimes of X-ray energies now used to perform RIXS: hard X-rays and soft X-rays. Here we deal with soft X-ray photons, living in the range of energies between 400 and 1000 eV, since they give us the possibility to selectively excite the Cu-L_3 absorption edge of copper atoms of the CuO_2 planes located around 931 eV, therefore selectively yielding useful information about the properties of these physical systems [8]. One of the principal properties of RIXS, which has been largely exploited in the results presented in the following, is the energy resolution: in fact, conversely to the Resonant X-ray Scattering (RXS) which supplies an energy integrated signal, RIXS gives selective information about the energy of the different excitations probed. Finally, both RIXS and RXS (as other diffraction techniques) are directly sensitive to charge and spin and provide also the dispersion in the momentum-space of the excitation probed.

Besides the physical importance of the subject per se, HTS is fundamental for its technological and scientific applications owing to the high critical temperature at which the superconductive state appears.

1.1.1 Cuprates: Strong Correlations and High Temperature Superconductivity

High temperature superconductivity broke the common assumption within the BCS framework that the maximum of Tc is bounded to 30 K (actually the conventional superconductor MgB_2 pushed this limit to 39 K). In fact, as it is possible to see in Figure 1.1, new experimental discoveries completely changed the landscape of superconductivity, with the record for Tc set to 165 K by HgBaCaCuO in high pressure conditions.

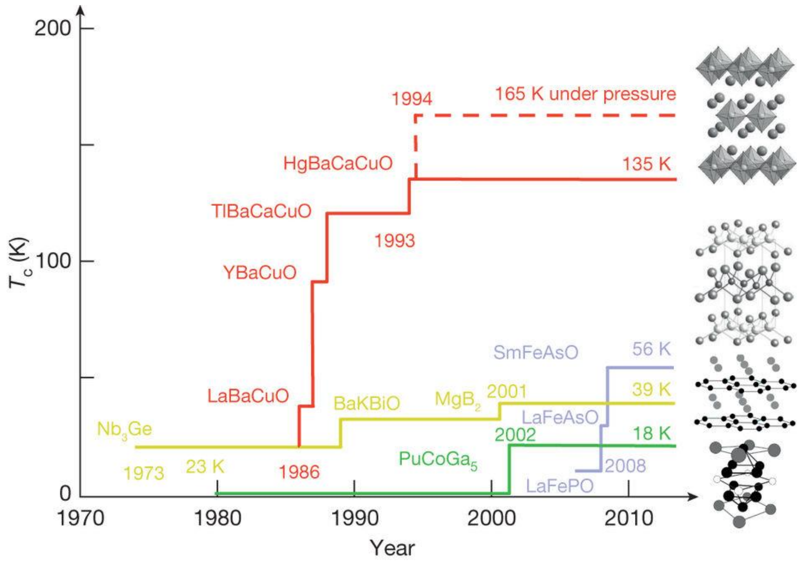

Figure 1.1: Critical temperature versus time. Images on the right show the crystal structure. Yellow: record for the conventional superconducting critical temperature. Green: heavy fermions (with low Fermi energies) superconductors. Purple: iron superconductors. Red: record high critical temperature found in cuprates (the dashed red line represents high pressure conditions). Figure reproduced for Ref. [9].

The cuprate parent compounds (i.e. the not doped initial chemical species) were the least likely materials where one would expect to find superconductivity. Indeed, in these insulating copper oxides the reigning interaction is repulsion between electrons driving antiferromagnetism and not the attractive correlation driving normal superconductivity. For this reason, causing their bad conductivity at T>Tc (2 orders of magnitude smaller than in normal metals), cuprates in the normal state are called "strange metals". This name defines properties which are in general shared among highly correlated electron systems not uniquely related to high temperature superconductivity [9]. The conventional quantum theory of electronic properties of solids fails in the description of strongly correlated oxides, among which cuprates are the most studied both for HTS and for the manifold of exotic physical phenomena they show.

The phenomenology of correlated electrons in copper oxides is based on large hopping barriers which prevent the jump of electrons between one copper site and another. Copper atoms in the superconducting plane (see Figure 1.2) of the parent compound are ionized once, with an odd integer number of electrons per atom. In any case the hole left in the Cu atoms presents a spin degree of freedom: the virtual hopping process between different Cu atoms produces, coupled with the Pauli exclusion principle, the antiferromagnetic structure in stoichiometric parent compounds: the result is a "Mott insulator" [9] encompassing insulating (2 eV gap) and antiferromagnetic properties (to be precise cuprates are charge transfer insulators, since the Coulomb repulsion involving electrons happens between the positive anion Cu^{1+} and the cation O^{2-}, rather than between two atoms of the same specie as it is the case for NiO). The failure of Fermi liquid models to describe these systems is stressed by the fact that under a conventional band theory they should behave like a metal, having an odd number of electrons per copper site. Increasing the doping and lowering the temperature (i.e. going outside of the "strange metal" portion of the phase diagram where insulating properties are still dominant) the behavior of these materials becomes akin to the one of a normal metallic electron system described by Fermi liquid theory. Nonetheless, they always show peculiar properties in their fermiology, since also in the "Fermi liquid" regime (see Figure 1.3) they present peculiar features like the pseudogap and Fermi surface reconstructions. In the end, the predominant antiferromagnetic, strong correlated character inherited by the parent compounds, facilitates the formation of breaking symmetry orders and local phase segregation lead by strong, short-ranged electron interactions in the real space [9].

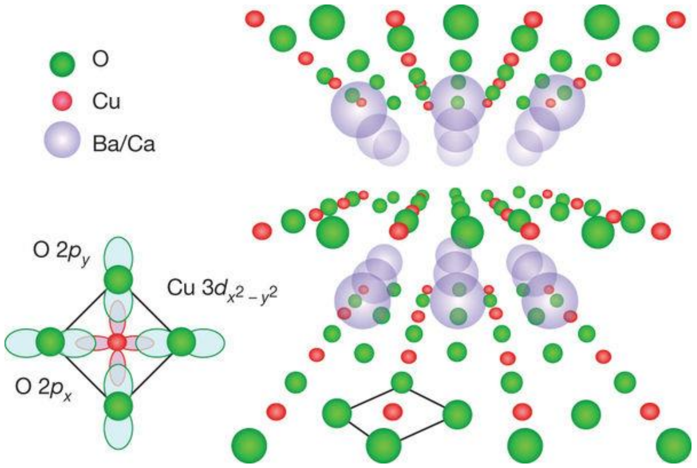

Figure 1.2: Crystal structure of the superconductive CuO_2 planes in cuprates, most of the times separated by an insulating, electronically inert buffer layer. The inset shows the principal orbital, which after hybridization constitute the electronic structure of the planes: the hole of copper $\boldsymbol{3d_{x^2-y^2}}$, oxygen $\boldsymbol{2p_x}$, $\boldsymbol{2p_y}$. Figure reproduced from Ref. [9].

To obtain the superconductive behavior in cuprates it is first necessary to modify their properties through doping: the CuO_2 planes are doped by changing the chemical composition of the spacer layer between different copper oxide layers, thus adding extra holes (hole-doping see Figure 1.3) or electrons (electron-doping). The doping level at which the critical temperature is maximum is called optimal doping. Cuprates samples with a doping level smaller or bigger than the optimal are respectively called underdoped and overdoped. After doping antiferromagnetism quickly disappears but dynamical magnetic fluctuating order is much stronger than in other conventional metals. The strong magnetic coupling (J≈140 meV) driving these fluctuations, is the reason for the appearance of spin excitations also in the non-magnetic state: the paramagnons [8].

To additionally complicate the picture, being non-stoichiometric compounds, the doped cuprates are chemically "dirty" and present a huge amount of structural disorder which plays a relevant role in all of the excitations and ordered states occurring in cuprates. Furthermore, it strongly hampers the already complicated theoretical description. In any case d-wave superconductivity appears to be rather insensitive to this spatial inhomogeneity, differently from the conventional s-wave state.

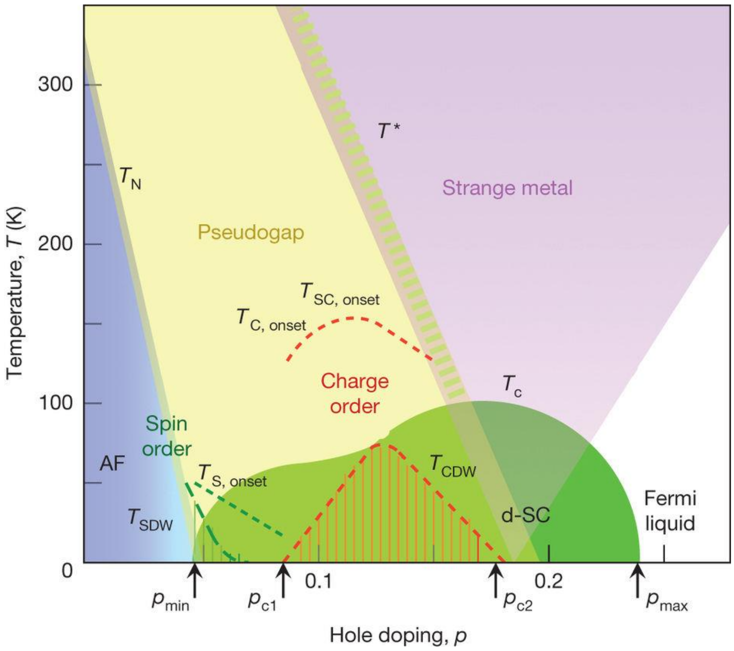

Figure 1.3: Phase diagram for hole-doped cuprates showing all the different orders in cuprates as a function of temperature and doping. AF and d-SC represent the regions of the antiferromagnetic and the d-wave superconductive state respectively, with their critical temperature T_N and T_C. The subscript "onset" indicates the region where the precursor order becomes visible: $\boldsymbol{T_{S,onset}}$ (green dotted line), $\boldsymbol{T_{C,onset}}$ and $\boldsymbol{T_{SC,onset}}$ (for both red dotted line) show respectively temperature at which spin, charge and superconducting fluctuations appear. T* indicates the pseudogap regime. Quantum critical points are indicated by arrows, while T_{CDW} and T_{SDW} indicate the two striped areas where the charge order and the spin incommensurate density waves are fully established. Figure reproduced for Ref. [9].

The pseudogap regime shown in Figure 1.3, is one of the most unclear phenomenological manifestations of the superconducting cuprates. On one hand, different probing techniques yield apparently contradicting results, on the other, this region of the phase diagram present the greatest number of different features all interconnecting one each other and creating an extremely complicated variety of scenarios. The most striking experimental fact is that both angle resolved electron spectroscopy (ARPES) and scanning tunnel spectroscopy (STS) suggest the presence of a discontinuous Fermi surface in the reciprocal space. In fact, gapped electronic excitations appear in the antinodal region (as opposite to the nodal region identified by the diagonal direction of the bidimensional momentum space), leading to a discontinuity between the doping dependent Fermi arcs of the nodal region (where zero energy hole-particle excitations hint the presence of a common metal-like Fermi surface) and the gapped antinodal portion of the momentum-space. Increasing the doping these Fermi arcs become larger and occupy all the momentum space. Researchers think that the Fermi arcs now visible are just the front part of supposed Fermi pockets formed after a reconstruction, possibly driven by charge order, in this way solving the problem of the bad defined Fermi surface [9].

To sum up, cuprates show a rich spectrum of properties and excitations involving spin, charge, orbital and lattice degrees of freedom. Some of these fundamental features will be discussed throughout the thesis. In particular, all the next session is dedicated to the analysis of charge order which is the main topic on which the work concentrates. Charge order manifests itself in the form of charge density waves throughout all the various families of cuprates. In Table 1.1 all the cuprate compounds with which we will deal are listed, together with their abbreviation.

Abbreviation	Formula	Category
LSCO	$La_{2-x}Sr_xCuO_4$	214 Family
LNSCO	$La_{2-x-y}Nd_ySr_xCuO_{4+\delta}$	
LBCO	$La_{2-x}Ba_xCuO_4$	
LESCO	$La_{2-x-y}Eu_ySr_xCu_2O_{4+\delta}$	
Bi2212	$Bi_2Sr_2CaCu_2O_{8+\delta}$	Bi-based
Bi2201	$Bi_{2-y}Pb_ySr_{2-z}La_zCuO_{6+\delta}$	
Hg1201	$HgBa_2CuO_{4+\delta}$	Hg-based
NCCO	$Nd_{2-x}Ce_xCuO_{4+\delta}$	Electron doped
Na-CCOC	$Na_xCa_{2-x}CuO_2Cl_2$	
YBCO	$YBa_2Cu_3O_{6+\delta}$	123 Family
NBCO	$NdBa_2Cu_3O_{6+\delta}$	

Table 1.1: List of the cuprate compounds mentioned throughout the text with the corresponding abbreviated name. The only electron doped compound mentioned here is NCCO. The doping levels can be varied in these materials by changing the values of specific elements as indicated by the subscripts x, y and δ.

1.2 Charge Density Waves

1.2.1 Introduction

The great importance of Charge Density Waves (CDW) is due to the fact that they are a ubiquitous feature of superconducting cuprates [10]. Therefore, a deep understanding of the working mechanism of high temperature superconductivity requires also a detailed study of CDW, since the two phenomena are clearly intertwined.

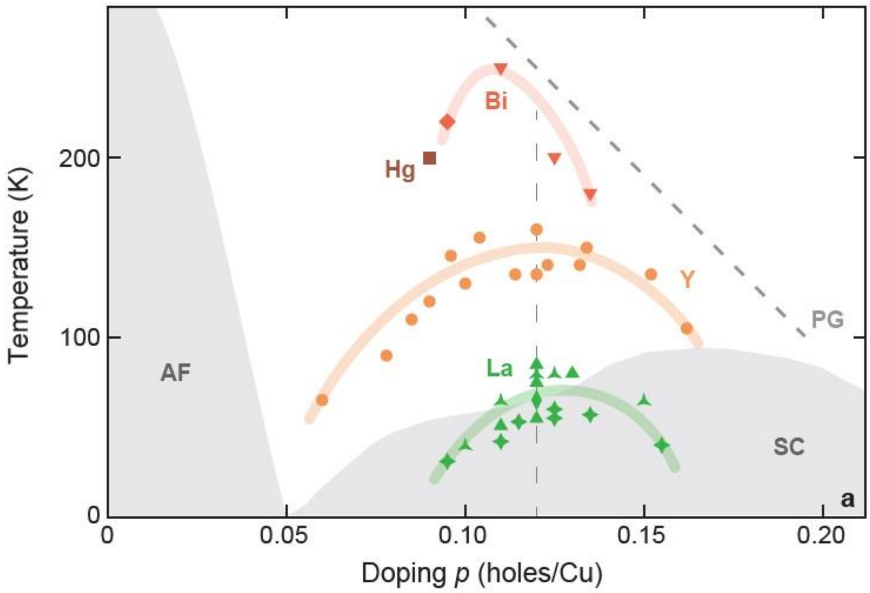

Figure 1.4: Onset temperature of the CDW versus hole-doping level for all the cuprate families. The vertical dashed line indicates the doping level of 12%. The shaded area represents the antiferromagnetic (AF), the superconductive (SC) and the pseudogap (PG) regions of the phase diagram for the YBCO. Figure readapted from Ref. [10].

CDW are one example of spontaneous symmetry breaking taking place in strongly correlated electron systems, which allows the total energy to decrease. In particular, upon changing the doping, a new type of charge order breaking the translational symmetry of the system arises: charges arrange in a periodic modulation incompatible with the lattice periodicity, around a doping level of 1/8 holes per Cu atoms (see the doping levels where charge order is present in Figure 1.3 and the range of the peak of the onset temperature in Figure 1.4). The formation of CDW in a wide range of doping levels around this value is a general feature of high temperature superconducting cuprates, as it is possible to see in Figure 1.4. In the following, we will mainly discuss results related to hole doping, however it has been recently discovered that this instability takes place also in the electron doped side of the phase diagram, confirming the ubiquitous character of the phenomenon in high temperature superconducting cuprates. The nature of charge density waves in these materials is determined by the interplay between the O-2p orbitals, pushing for itinerancy and delocalization of charge, and Cu-3d states, which account for the antiferromagnetic and insulating properties, given their localized nature. This competition can be tuned by changing the hole doping level thanks to a different concentration of oxygen atoms, rare earths elements or metals with different electron affinity (see Table 1.1). The result are patches of coherent unidirectional charge density modulations distributed in the CuO_2 planes with dimensions of several unitary lattice sided (for instance in the case of Bi2212 the correlation length is of order of 30 Å [10]).

A general feature of the charge density modulations in cuprates is the fact that they are quasi-static, for instance, they are located at zero energy loss within the experimental resolution for RIXS. Furthermore, they can be detected by such slow probing techniques as scanning tunnel microscopy (STM) and nuclear magnetic resonance (NMR). So, taking into account also the RIXS resolution, the energy associated to the charge fluctuations can be fixed to an upper bound of 20meV [11]. STM experiments confirm that they are a phenomenon involving orbitals in a wide range of energies (as wide as 40 meV [12]). This is confirmed by the Fourier transform of the differential conductance (g=dI/dV) of various STM images taken with different bias voltages: all the spectra in the momentum-space show that every peak maintains the same position (in particular the one related to charge order) and also that the ratio between the intensities of different peaks is conserved within the same spectrum, when the bias changes [13], [12]. To better illustrate, since the differential conductance at a given bias voltage (V_{bias}) between the sample and the STM tip is proportional to the local density of states at that energy distance (eV_{bias}) from the Fermi level, we can conclude that the equal modulation we see at different biases indicates all those orbitals are involved in the CDW in the same manner.

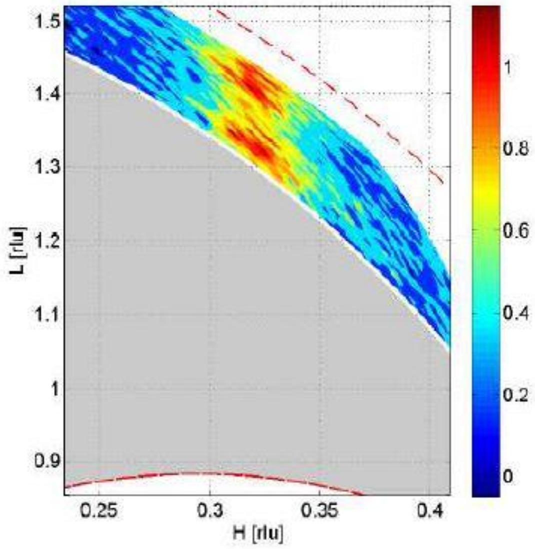

Figure 1.5: Energy integrated spectra after background subtraction (the background is assumed to be represented as the scans at 200 K). The CDW peak is weakly dispersing along the L direction, indicating a small coupling of different planes. In fact, the intensity of the peak retains its value even at different L coordinates and the position of the peak doesn't vary. Red dashed lines indicate the maximum values reachable in the experimental configuration adopted. The grey area indicates a range of the reciprocal space where data were severely contaminated by a diffusive noise. Figure reproduced from Ref. [11].

CDWs show a clear two-dimensional character: they live inside the bi-dimensional CuO_2 planes with a null or negligible coupling with other layers of the material, as demonstrated by Figure 1.5 where we can see that the peak associated to the CDW in the H direction, is not dispersing with the L direction of the reciprocal space. This demonstrates that a low coupling exists between different planes for the charge modulation instability. The previous statement justifies the fact that the simulations showed in the next chapter have been carried out in a bi-dimensional domain. Moreover, to prove that this symmetry breaking phenomenon occurs inside the CuO_2 planes, we cite the example of YBCO reported by Ghiringhelli et al. [5], where it is demonstrated how the resonant X-ray signal comes from the copper atoms in the planes rather than from the chain reservoir sites. This has been proved thanks to one of the most important features of RIXS spectroscopy: elemental and also chemical selectivity. In fact, by slightly changing the photon frequency we are able to selectively access different chemical environments for the same atomic specie, as it is the case for YBCO. In particular, by tuning the photon energy exactly to the Cu-L_3 absorption edge of the copper atoms belonging to the CuO_2 planes we can detect the signal by the CDW, while no signal is measurable if we set the energy of the incoming photon equal to the resonance of copper in the charge reservoir chains. Another peculiar feature of RIXS gives us certainty about the fact that the incommensurate peak visible at 0.31 r.l.u.[1] in YBCO is related to charge instead of spin order. Indeed, Ghiringhelli et al. demonstrated by analyzing the polarization of the outcoming beam (see chapter 3) that the peak is related to charge excitations, which do not require the polarization of the scattered photon to change, and no to magnetic excitations, which instead cause a 90° rotation of the polarization of the X-rays.

1.2.2 Historical overview

1.2.2.1 Commensurate stripes: 214 family

The first observation of charge order in cuprates took place in the family of La-based compounds [4]. This family of cuprates displays charge order in terms of stripes, which actually include both charge and spin order (see Figure 1.6). In fact, the doped holes in La compounds percolate inside the CuO_2 planes and arrange in a periodic structure of unidirectional chains yielding characteristic peaks in the reciprocal space. The characteristic wavevector of the charge modulation (2δ) increases linearly with the doping till the value of 0.25 r.l.u. ($4a_0$ period of the modulation) reached at a doping level of 0.125, when it saturates [11], [14]. This behavior has been theoretically explained, in the frame of strong real space correlations, as the tendency of the extra-charges provided by the doping holes to organize into half-filled stripes with a spacing between one each other dependent on the doping level: this explains the evolution of 2δ with the doping, which determines the

---

[1] From now on we will interchangeably use reciprocal lattice units (r.l.u.) or the actual value of $2\pi/a,b,c$ (where a,b and c represent the basis vectors of the unitary cell of the crystal, expressed in Å, respectively along x,y and z directions), when referring to vectors in the reciprocal space. In particular, we will use, following the convention, for the components of an arbitrary vector of the reciprocal space: $Q = (H; K; L) = (2\pi/a; 2\pi/b; 2\pi/c)$. For cuprates a and b are directed as Cu-O bonds of the superconducting plane and given the mostly bidimensional character of the excitations discussed we will often forget the component directed along z of the reciprocal space, concentrating on the CuO_2 planes.

concentration of stripes. This mechanism stops when the doping level of 12.5% is reached: at this point the super-lattice does not vary anymore and the extra-charges introduced fill the existing stripes, causing the wavevector of the modulation to assume a constant behavior versus doping [15], [16]. At the same doping of 12.5% (where the number of stripes saturates) the phase diagram also shows a dip in the Tc curve, indicating a possible competition between charge order and superconductivity (see Figure 1.3, Figure 1.4).

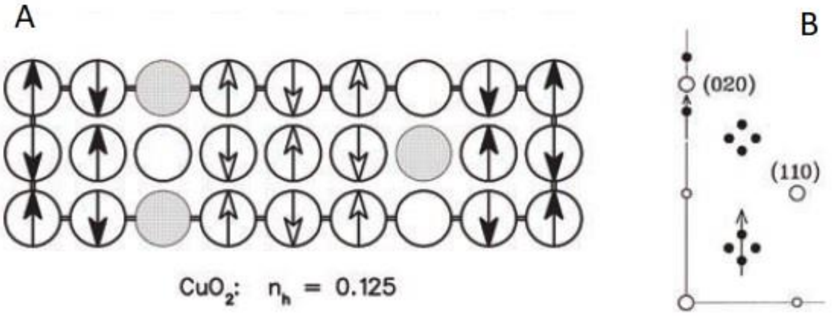

Figure 1.6: Stripe order in 12.5% hole-doped $La_{1.6-x}Nd_{0.4}Sr_xCu_2O$. (A) real space representation of the stripes: circles represent Cu sites; grey circles show the position of holes. Arrows indicate the direction of spins on the $3d^9$ Cu atoms. (B) reciprocal space representation of the 2D neutron scattering data: white circles represent Bragg peaks, black circles for the charge and spin satellites. Readapted from Ref. [4].

Concerning the magnetic order, as it is possible to see in Figure 1.6.A, charge stripes separate different undoped antiferromagnetic (AF) domains, which organize with a doping dependent periodicity (the wavevector of this super-modulation is δ) which is twice the periodicity of the charge order in the real space and is dictated by the density of stripes, working as boundaries for the AF domains. This super-periodicity imposed by stripes to the antiferromagnetic order produces a splitting of the AF peak into four different satellites located at (0.5,0.5±δ), (0.5±δ,0.5) r.l.u. (see in Figure 1.6.B). Finally, the stripe order is strictly unidirectional (as opposite to the checkerboard pattern), static and characterized by the fundamental relation between charge and spin wavevectors: $\delta_{charge}=2\delta_{spin}$. The experimental techniques employed in the first experiments to show the evidence of stripes, used neutrons as probing particle. While neutrons are sensitive to spin interactions they are not able to give direct information about charge order. Therefore, they can directly detect the pattern of spin moments of the cuprates but they give only an indirect information about the charge periodicity by imaging the lattice distortion caused by this modulation.

1.2.2.2 Charge order in Bi-based compounds

After great technological improvements, also the STM technique has been used to probe the details of the charge density waves in cuprates. While neutrons require huge crystalline samples due to their low scattering cross-section, STM on the other side, needs a very clean and defect free exposed surface. So, its adoption has been limited to few high temperature superconducting materials, belonging to the Bi-based family, thanks to their natural atomically flat planes. A significant feature of STM is that it is compatible with the application of external magnetic fields, allowing the introduction of another significant degree of freedom in the landscape of the possible experimental variables (as will be discussed in the paragraph 1.2.4). The first proof of the existence of charge modulations in materials different from La-based family came from the work of Hoffman et al. in 2002 [17]. Following the discovery by Hoffman et al. in Bi2212, the next material where charge order has been found was Na-CCOC: as already pointed out in previously both these two materials present charge modulations involving orbitals in a wide range of energies, as confirmed by the investigation using different STM bias voltages. Subsequent studies of the doping dependence of the wavevector in $Bi_{2-y}Pb_ySr_{2-z}La_zCuO_{6+\delta}$ (Pb-Bi2201) and in Bi2212 pointed out a possible connection of CDW instability with the antinodal region of the Fermi surface [18] [6], therefore suggesting that the possible driving mechanism for the charge modulation could be k-space, Fermi liquid based weak correlations (in chapter 2 an alternative point of view indicating strong real space interactions as the cause of charge instability will be presented).

At this point charge order had been discovered in La-based, Ca-based and Bi-based compounds, but still there was no direct proof of its existence in the 123 family of superconductors (like $(Y,Nd)Ba_2Cu_3O_6$ compounds). There were though some indirect evidences based on quantum oscillation measurements at low temperatures and high magnetic fields, pointing toward a reconstruction of the Fermi surface driven by "a density wave phase" [19], and based on the similarity of Seebeck and Hall coefficients of YBCO with those of LESCO [10]. Nevertheless, till the moment in which NMR measurements in high magnetic fields [20] confirmed the charge nature of this wave (no spin order linked to this instability was seen), nobody knew whether this "density wave phase" was related to charge or to another kind of excitation. Furthermore, Wu et al. [20] pointed out that this charge density wave freshly discovered also in YBCO, exhibited a unidirectional, static character likely due to the same $4a_0$ periodicity typical of the stripe structure. They went on declaring the competing nature of the interplay between charge order and superconductivity also in YBCO and deeming the CDWs as an intrinsic property of superconducting planes of copper oxides.

1.2.2.3 Incommensurate charge order: 123 family

A turning point came with the direct observation in the reciprocal space at zero magnetic field applied of charge order in (Y,N)BCO by Ghiringhelli et al. [5], by means of the RIXS technique. The results shown in this article demonstrate that charge order in YBCO assumes characteristics different from the stripe order previously known in other La-based cuprates, since the wavevector of the charge modulation in this material, is equal to 0.31 r.l.u. and therefore is manifestly incommensurate (the real-lattice periodicity is not four nor three unitary cell sides see Figure 1.7). Moreover, no spin order is present together with charge order, confirming the different nature of the instability in 123 family from the case for stripe-ordered cuprates. Referring to Figure 1.7 we can recognize the typical features related to CDWs: (i) they are quasi-elastic within the instrumental resolution and (ii) they are strongly dispersing in the reciprocal space indicating that the modulation assumes a precise wavevector even though the peak is not so sharp as we expect due to the relatively small correlation length characterizing this kind of order. In the work of Ghiringhelli et al. the peculiar properties of RIXS are exploited to prove that this peak is related to charge and that the signal related to CDW comes from the copper sites inside the superconducting planes (Cu2 atoms in Figure 1.7). The first statement is demonstrated by analyzing the polarization dependence of the peak intensity in the outcoming signal thanks to the polarization analyzer (polarimeter) available in the experimental setup: in fact, knowing the polarization in the two different outcoming channels σ' and π' (respectively perpendicular and parallel to the scattering plane) and the polarization of the incident beam (σ in this case), by a comparison with theoretical calculations, it appears that the modulation causing the peak in the reciprocal space is due to charge rather than to spin.

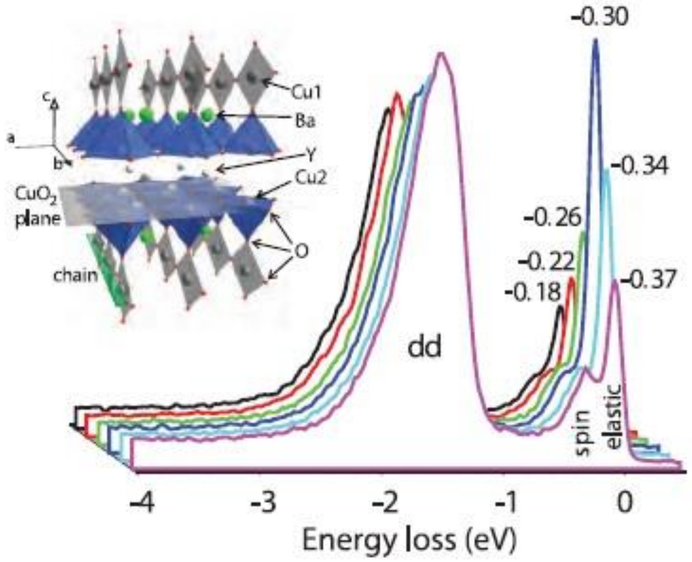

Figure 1.7: Energy-resolved RIXS spectra taken at 15 K of underdoped $Nd_{1.2}Ba_{1.8}Cu_3O_7$ (Tc =65 K) for different values of the H component of the transferred momentum Q = (H, 0, L). The quasi-elastic component, strongly dispersing, has a maximum intensity at H = −0.31 r.l.u., the paramagnons (spin) are visible next to the quasi-elastic peak and the interorbital particle-hole excitations (dd) around 2 eV carry most of the spectral weight. Inset: crystalline structure of YBCO where copper atoms in two inequivalent lattice positions are recognizable. Cu1 atoms belong to the charge reservoir chains, while Cu2 atoms constitute the CuO_2 planes. It is possible to distinguish the signal coming from different lattice positions thanks to their different resonant absorption energy. Figure readapted from Ref. [5].

As already stated in paragraph 1.2.1, it is possible to exploit the different chemical shift in the absorption edge of Cu1 and Cu2 atoms to selectively extract the signal from just one of the two lattice sites. This is possible by tuning the energy of the incoming photon exactly to the resonance energy of the atomic Cu atom we want to excite: the results from this kind of measurement confirm that the signal comes from the superconducting planes. This article also demonstrates that the charge modulations take place in both the two orthogonal Cu-O bonds directions, although with different intensity, as shown by the presence of an analogous peak also along the K direction of the reciprocal space. Therefore, we have another reason to rule out the influence of the Cu1 chains to the CDW signal since in the untwined samples they are aligned along a single direction [11]. Both energy integrated (RXS) measurement and energy resolved (RIXS) data in the quasi-elastic region, present a single peak at the same position in the momentum-space, pointing out that the dispersion comes mainly from the quasi-elastic charge modulation (see Figure 1.7). Another fundamental achievement of this paper is the demonstration that CDW instability can coexist with the superconductivity, albeit they compete. In fact, till that moment it was thought that charge instability required the complete obliteration of the superconductive state (for example thanks to an external magnetic field applied orthogonally to the copper oxide planes), while the results presented are taken at zero applied magnetic field. As we will discuss better in a later paragraph, Ghiringhelli et al. showed that the divergence of the CDW instability, as the temperature is decreased, abruptly reverses upon cooling below the critical temperature of the superconductor, as testified by the decreasing intensity and by the increasing full width at half maximum (FWHM, which is inversely related to the correlation length of the charge order). This further discovery unequivocally confirms the competition between the two symmetry breaking states.

We need to point out though, that it is not obvious to assign the results observed by Ghiringhelli et al. with RIXS experiments at zero applied magnetic field to the same kind of charge instability measured by NMR at high fields. In fact, further measurements performed using both these two techniques (in particular due to the relevance of the presence of an external field, RIXS has been performed in an pulsed magnetic field regime as high as 28 T) identified a phase transition between two types of order triggered by the application of high magnetic fields: the high field phase is characterized by long range modulations with a different period along the c axis and it is intrinsically bidimensional, while the zero field phase presents short range coherence and unidirectional character. Moreover, it has been proved that these two phases coexist at low temperature and high magnetic fields applied [21].

1.2.2.4 Ubiquity of charge density waves

The next step was to find charge order in the last family of hole-doped cuprates left, the Hg-based compounds. In 2014, two years after the discovery by Ghiringhelli et al., Tabis et al. [22] demonstrated the presence of CDW in underdoped Hg1021 below 200 K. The wavevector of the modulation in this material is 0.28 r.l.u. and to be detected the use of resonant experiments was required meaning that the phenomenon is quite weak. Because the Hg family has the record for the highest critical temperature, the weakness of charge modulation in this group could indicate once again an anticorrelation between superconductivity and charge order instability. Tabis et al. found also interesting links between the CDW and other physical properties related to the Fermiology of the material, finally suggesting as common cause for the series of breaking symmetry states appearing in cuprates (antiferromagnetism, charge order and superconductivity), the "short-range antiferromagnetic correlations".

To summarize, the results presented so far for the hole-doped cuprates demonstrated a clear distinction between two different phenomenological manifestations of charge order: stripe-order taking place in La-based compounds and charge modulations taking place in all the other families. The main differences between these two are on one side the fact that in stripe ordered compounds spin order and charge order coexist, while in the other cases they are mutually exclusive, and on the other side the fact that evolution of the wavevector of the modulation has slopes with opposite signs in the two cases: for La-based cuprates the wavevector increases with doping till it saturates at the doping level of 12.5%, whereas in the other cases it decreases with doping hinting to a possible nesting scenario in this case. Charge order instability therefore presents common traits across different cuprates but displays also stark differences.

To prove that CDWs are really a ubiquitous attribute of CuO_2 superconducting planes in cuprates also the electron doped side of the phase diagram has to be checked. The first direct proof of the presence of this kind of instability in the left side of the phase diagram comes from the work by Da Silva Neto et al. who performed RXS measurements on NCCO 14% doped [23]. They found a CDW peak attributable to short ranged correlations (25-35 Å) at a nearly commensurate value (around $0.25*2\pi/a_0$), similar to the periodicity of the modulation found in the hole-doped compounds, suggesting a common origin for the charge order. However also a strong difference was discovered since the charge order in NCCO presents an onset temperature (350-400 K) much higher than the pseudogap temperature, nearly close to the Néel temperature. This achievement rules out a possible connection here of the CDW with the pseudogap and could instead suggest a link with antiferromagnetism.

This last finding reaffirms the ubiquitous character of charge order across different cuprate families, across different levels and mechanisms for doping (for example see the differences between charge reservoir chains in YBCO and the rare-earth doping in La-based compounds) and finally across the two opposite sides of the doping phase diagram (electrons VS holes). Understanding the working principle at the basis of this instability is therefore vital in order to understand the intimate nature of high-temperature superconductivity in cuprates and a challenging task per se.

1.2.2.5 Latest news

Referring to Figure 1.3 and Figure 1.4, we can see how charge modulations live in a finite range of doping values where we can recognize two endpoints which have been associated to a possible quantum critical behavior (see for instance [24]). Moreover, many have argued that the onset temperature of the CDWs in the hole doped part of the phase diagram seems to relate to the pseudogap temperature T* and that their wavevector is compatible with the distance between Fermi arcs tips (as mentioned above) thereby suggesting a possible connection between charge order and the pseudogap regime [25]. Here we report a recent result by Peng et al. [26] seemingly overturning these commonly accepted results. In fact, a strong peak attributable to charge order is found in different overdoped samples of $(Bi,Pb)_{2.12}Sr_{1.88}CuO_{6+\delta}$. The proof that a charge modulation is probed comes once again by the elemental sensitivity of RIXS and by the polarimeter available in the ID32 beamline at ESRF. In fact, the signal coming from this peak in the two crossed polarization channels ($\sigma\pi'$, $\pi\sigma'$, where the symbol ' indicates the polarization of the outcoming beam) is zero within the error bars, so the peak is completely attributable to charge that does not cause changes in the polarization of the incoming photons conversely to spin excitations. On the other hand, lattice displacements are ruled out by looking at the photon energy dependence of the signal: if the lattice were the cause, still a signal with sizable amplitude should be seen upon detuning the photon energy from the Cu L_3 absorption edge. Instead a variation of the intensity of the peak following the X-ray absorption spectroscopy (XAS) line shape is obtained, demonstrating that the signal comes only from charge modulations at the copper sites. Furthermore, since in Pb-doped Bi2201 samples the Cu atoms are located uniquely in the superconducting planes (differently from what happens in the case of YBCO) this new experimental outcome again fosters the bidimensional character of modulations, as a general feature of charge order across cuprates. In the data available, the maximum of the charge peak for the sample OD11K (Tc=11K, p≈0.215) is located both at positive and at negative values along the H direction Q||= (±0.14, 0). The wavevector resulting from the position of these peaks at this and at other two doping levels (p≈0.205, p≈0.23) is in contrast with the available STM measurements which detect a signal with an almost doping independent wavevector of 0.25 r.l.u. till a doping level p≈0.21, but follows linearly the trend achieved by previous RIXS measurements in a lower doping range (even though there is a big jump for the doping levels in the range from p=0.16 to p=0.205). The peak is quasi-elastic, and within the experimental resolution, the upper limit for the energy of the associated excitation can be fixed to 10 meV, as it is the case also for other CDW measurements in other compounds. On the other hand, differently from past data, here we cannot see any chance of finding a nesting wavevector in the Fermi surface compatible with the periodicity of this wave. As well, for sure we cannot make any trivial connection between the onset temperature of the new charge modulation, which is robust till 250 K, and the pseudogap temperature, which goes toward zero in the overdoped regime thereby proving the presence of charge order in absence of pseudogap. Moreover, Peng et al. demonstrate that the integrated intensity of the peak (and therefore the strength of the correlations) is almost constant from 20 K to 250 K, so the onset temperature of this excitations seems to be way higher than 250 K putting this CDW in relation with the charge order displayed by electron doped cuprates, where, as we said, the onset temperature is comparable to the antiferromagnetic transition temperature. To add further details to the extraordinary nature of this new peak, its intensity is twenty times higher than the maximum intensity of the interorbital dd excitation and its width is associated with correlation lengths as high as 40-60 unitary cell sides. To give a reference, the maximum of the CDW intensity in NBCO (where these modulations are stronger than in Bi-based compounds) is of the same order of the dd peak height (see Figure 1.7), while the correlation lengths measured in Bi2201 are one order of magnitude smaller (of order of $6a_0$) for lower doping ranges. Given the differences between this new peak and the old results, in addition to the lack of information, Peng et al. declare it is not possible in this early stages to attribute this charge order to a new phase or to say that it comes from the evolution of the 'normal' charge order state measured in previous RIXS experiments. These experimental findings, even though preliminary and needing for successive confirmation, show how complicated and heterogeneous is the landscape of charge order in cuprates and redesign the CDW part of the phase diagram of Bi2201 (see Figure 1.8). There are no prevailing clues pointing at a precise and common cause for their existence across all the cuprate families. In particular, there are apparently contradicting indications implying the possible driving mechanism could be identified in both real-space strong correlations and reciprocal-space weak Fermi surface couplings. In the next chapter, we will present a theory hinging on the assumption that strong electron-electron correlations are able to explain the charge order as a whole. Figure 1.9 summarizes the doping behavior of the wavevectors of the charge density modulations across all the different hole-doped families of cuprates. This graph, and in particular the range of values assumed by the periodicity in Bi-based compounds, is important for what we are going to discuss in the next chapter, where a theory ascribing the whole CDW landscape to $4a_0$-commensurate periodic modulations is presented.

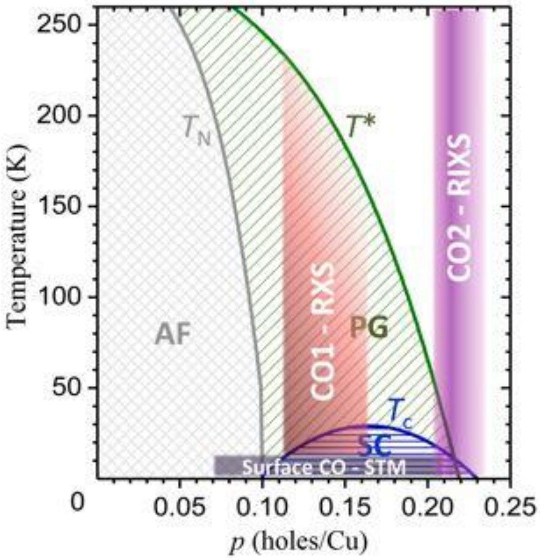

Figure 1.8: Phase diagram of Bi2201. It shows the antiferromagnetic region (AF) delimited by T_N, the pseudogap regime and its associated temperature T* (PG), the superconducting dome (SC) delimited by T_C, all of them reproduced from NMR measurements, and the type of charge order (CO) found in this material. The grey box named Surface CO represents the doping range where CDWs are found by STM, CO1 indicates the doping and temperature ranges where RIXS-RXS have spotted charge modulations till now and CO2 represents the new results outlined. Figure readapted from Ref. [26].

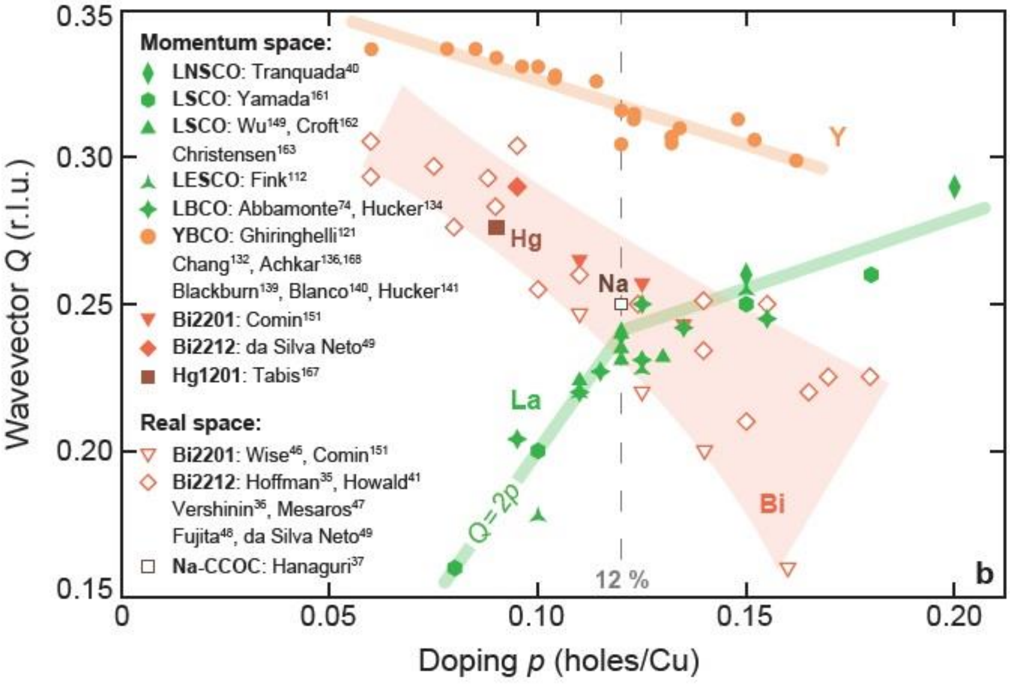

Figure 1.9: Wavevector as a function of doping for all the cuprate families. Full symbols represent experimental data from momentum-resolved probes while empty symbols are for real space measurements. All the lines are guide to the eyes except for the Q=2p line which represents the dependence on doping of the wavevector in the case of perfect stripes half-filled. Figure readapted from Ref. [10].

1.2.3 Real and reciprocal space

As stated throughout this chapter and the next, the duality between real and reciprocal space plays a major role in the story of charge order in cuprates. In fact, on one side we have two opposite probing mechanisms, the STM versus the momentum-space based experimental techniques, and on the other side we have different experimental clues, leading to diverging theoretical explanation depending on the particular characteristic, out of the whole experimental landscape, it is believed the most. We have already anticipated something about the dichotomy between probing techniques and we will speak in greater detail about the different theoretical points of view in the next chapter. Here we outline the principal ingredients of these two sides of the charge order world.

The discovery of charge order in YBCO strongly motivated new theoretical and experimental efforts to find the distinctive signature of charge instability, joining its different manifestation in cuprates families. But, there are still divergences between the real space measurements of Bi-based family and the diffraction and scattering experiments yielding information about the reciprocal space structure of the 123 and La-based families. In particular, the sources of wariness are the different probing depths of the two groups of techniques (a single atomic layer versus 100 nm or more) and a possible different nature for the charge modulations taking place on the surface of Bi-based compounds from the charge order of layers located in the bulk. A work by Comin et al. [25] demonstrates that the nature of the microscopic entities detected in RXS data and STM measurements is the same, by using both these two techniques on La-doped Bi2201. In fact, the peak position achieved by the scattering probe is the same as the Fourier transformed differential conductance data (yielding the local density of states) of STM. The choice of performing the comparison between the two techniques on a Bi-based compound was obliged by the need for the STM of an atomically flat surface which cannot be provided by other families of cuprates. The same evidence is found in Bi2212.

One indication pointing at a unified picture of real space modulations and reciprocal space fermiology (as opposite to an explanation based on real space strong e-e correlations) comes from angle-resolved photoemission spectroscopy (ARPES) results [25]. In fact, the distance between the tips of Fermi arcs in the antinodal region of Fermi surface is closely related to the wavevector of the charge density modulation, seeFigure 1.10. This relationship indicates a possible connection between the charge order and the weak k-space interactions due to the low-energy electronic structure, explaining thus the continuous evolution of the wavevector with the doping. Conversely, recurring values of the periodicity of the charge order close to 0.25 r.l.u. put CDW in a closer relation with theories based upon interactions involving strongly correlated electrons (see next chapter).

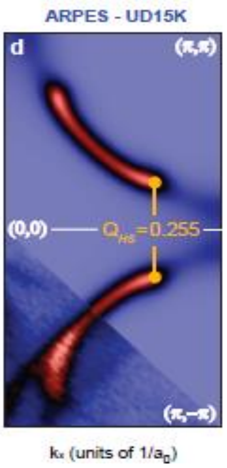

Figure 1.10: Experimental (bottom left) and theoretical Fermi surface for UD15K Bi2201. It is possible to see the Fermi arcs typical of the pseudogap regime, with the yellow wavevector connecting the 'hot-spots' of the antinodal region of the Fermi surface. Readapted from Ref. [25].

1.2.3.1 Form factor

Following as a reference the work of Comin et al. [27], we now outline the role that the unitary entity, periodically repeated to form the 2D lattice of the superconducting planes, has in building up the signal acquired by both STM and RXS: i.e. what yields the form factor in the Fourier space. In the theory of scattering the form factor represents the spectral distribution of wavelengths and energies S(q,ω) associated to the scattering from a single atom or a single unitary cell periodically reproduced to compose the whole lattice. In the case of cuprates CuO_2 planes charge density waves are due to the periodic modulation of the occupation of three different atomic orbitals all located in a close energy range and forming the unitary cell: the $3d_{x^2-y^2}$ Cu orbital and the $2p_x$, $2p_y$ orbitals of oxygen atoms. Since these three orbitals are located in a narrow interval of energies, we cannot a priori neglect the interplay and the mixing of all their contributions, even in the case of RIXS where we are dealing with an orbital sensitive technique.

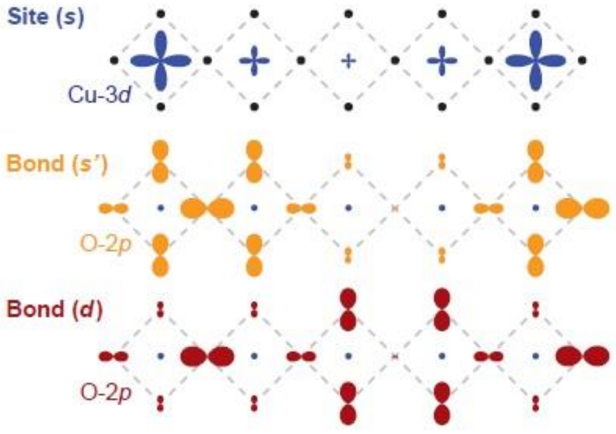

Figure 1.11: Charge modulations given by the three different non-orthogonal bases used to build up the form factor. To each atom of the unitary cell is given a different weight, then the created elementary brick is repeated with multiplied by a periodic function to create the overall periodic modulation of charge giving rise to CDWs. Readapted by Ref. [27].

Looking at Figure 1.11 it is possible to see a particular choice for the form factor basis, whose components display three different kind of symmetry: (i) an s wave built with the central Cu atoms only, (ii) an s' wave involving p_x and p_y oxygen orbital with the same phase, (iii) a d wave composed by both the oxygen orbitals taken with opposite sign and with the maxima shifted by half a wavelength. The amplitudes (look at the dimensions of the colored symbols in Figure 1.11) assigned to the different types of modulation indicate the amount of extra charge present on that particular orbital. Through this basis set it is possible to fully decouple the charge order parameter in the reciprocal space as an independent superposition of these three different terms. Comin et al. exploiting information about the polarization dependence of the RIXS signal and comparing it with their theoretical model have been able to detect as principal component of the form factor of YBCO a d-wave symmetry, while for the stripe-ordered LBCO the best agreement was found using an s'-wave character. Fujita et al. [28] performed a similar analysis using STM to discover that also charge order in Na-CCOC and Bi2212 (which will be discussed in chapter 2) is mainly determined by a d-wave form factor. These results may suggest another intrinsic difference between stripe-ordered cuprates and charge order in the other families.

1.2.3.2 Checkerboard VS unidirectional order

Charge density waves in cuprates are modulations of the orbital occupation along the two orthogonal Cu-O directions. While it has been immediately clear that the kind of order in striped cuprates was compatible only with a unidirectional modulation (the stripes organize locally along just one precise direction), in the other cases it has been more difficult to find out whether charge order presents a unidirectional or checkerboard symmetry. To further complicate the situation, while spin order and charge order integrate one each other in La-based compounds, they are mutually exclusive in Bi-based and 123 families, preventing the possibility of making a direct comparison between the two classes of high Tc-superconductors. Moreover, we could think that the STM, yielding direct access to the real space, would solve the conundrum but this has not been the case till recent years, when this technology made great step forward revealing a prevalent unidirectional order [29]. This was due to the fact that Bi-based compounds, with their intrinsic disorder, blurr the distinction between these two kinds of symmetry [10]. On one side, unidirectional order means that the CDW locally assumes a wavevector directed along just one of the two Cu-O directions, on the other side we have the checkerboard order implying that the charge modulation is locally made by the joint superposition of waves directed in both the two orthogonal directions. That does not mean that the unidirectional order exhibits a peak only in one direction of the reciprocal space because we could have a lot of small independent domains, each one with its own modulation along one of the two different directions, therefore constructing both the two peaks in the Fourier space. Furthermore, the two orders are difficult to distinguish in the real space because if different unidirectional domains overlap, the result is completely analogous to a checkerboard symmetry (see next chapter). The final evidence that the CDW in cuprates are unidirectional came from another work of Comin et al. [30] who demonstrated, by resolving the full momentum structure of YBCO, that the peaks related to charge order along the two directions H and K of the reciprocal space are different (with the peak along K direction being stronger than in H direction), therefore proving that the fourfold D_{4h} symmetry of the checkerboard order is broken in cuprates. This finding rules out the possibility of such a symmetry for the charge density waves. In particular, they showed (see Figure 1.12) that also the width and the evolution of the correlation length in the two dimensions (H and K) of the two peaks ((Q,0) and (0,Q)) is different for the two different axes of the momentum-space, hinting for an independent nature of the modulations along x and y directions. This is the reason why in the next chapter to simulate shape in the real space of the charge order we treat each CDW as an independent excitation living in a finite region of space and possessing a wavevector with a single well defined direction.

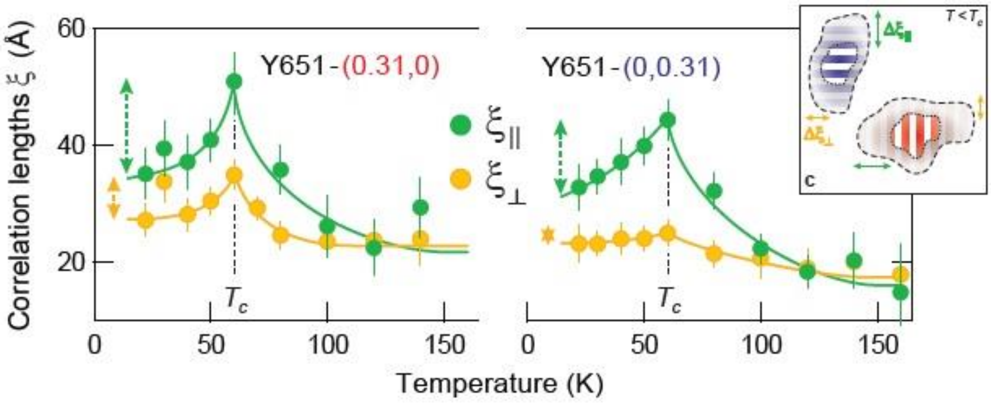

Figure 1.12: Temperature evolution of the correlation length of $YBa_2Cu_3O_{6.51}$ for the parallel (directed the same way as the CDW wavevector) and the orthogonal (orthogonal to the wavevector of the modulation) directions for both the H (0.31,0) and the K (0,0.31) peaks in the reciprocal space (see also the inset). The correlation length is known to be inversely proportional to the width of the peak in the reciprocal space and therefore analyzing the FWHM in the momentum-space we can extract information about the strength of the CDW given by the correlation length. As it is possible to see the orthogonal correlation is in both cases smaller than the parallel suggesting a locking mechanism, dependent on the direction of the wavevector of the modulation, causing this anisotropy. Note though, that the temperature behavior and the absolute value are different for the H and K peak, so the two possible directions of modulation are independent demonstrating a unidirectional order. Readapted from Ref. [30].

1.2.4 Competing orders

The competing nature of the relationship between charge order and superconductivity has been outlined throughout the discussion and results presented till this point. Here we want to summarize and to stress some of the most important points that will be also tackled in later sections of this work. One of the first examples of this competition in non-stripe-ordered compounds, is testified by Hoffman et al. [17], who managed to see bidirectional, four-fold CDW with their STM experimental setup only upon application of a magnetic field of 5 T, inside the vortexes of Bi2212, where the magnetic field had killed the superconductive state. This results confirms the phenomenology previously found in stripe-ordered La-based compounds that CDW and superconductivity try to avoid one each other. The same thing happened with YBCO where the first indications of charge order were retrieved with NMR measurements only after the application of rather high magnetic fields (up to 62 T) [10].

1.2.4.1 Temperature

We can also clearly see this clash by looking at the temperature behavior of the intensity and of the width (see Figure 1.12) of the charge order peak of YBCO in the reciprocal space [11], [5], [30], [31]. In fact, the intensity of the peak increases, upon cooling, till the critical temperature T_c where it reaches a maximum and it suddenly decreases for lower temperatures. A similar non-monotonic behavior is displayed by the FWHM which decreases from high temperatures to T_c assuming its minimum value and then increases again as the temperature goes down. These trends suggest a rivalry between the superconductivity and the charge order: referring to Figure 1.12 it is possible to see that the correlation length (ξ, inversely proportional to the FWHM), which indicates the strength of the CDW, grows outside the temperature range where superconductivity is present upon cooling. Such a behavior hints to the possible formation of a static order when ξ explodes to infinite. But when the superconductive state appears the charge order is suddenly weakened and this supposed divergence never happens. The same can be said for the intensity, which is a measure of the amplitude of the oscillations and also of the proportion between the area covered by charge density waves and the total area of the probed region of the CuO_2 plane (as confirmed by the simulations described in the next chapter).

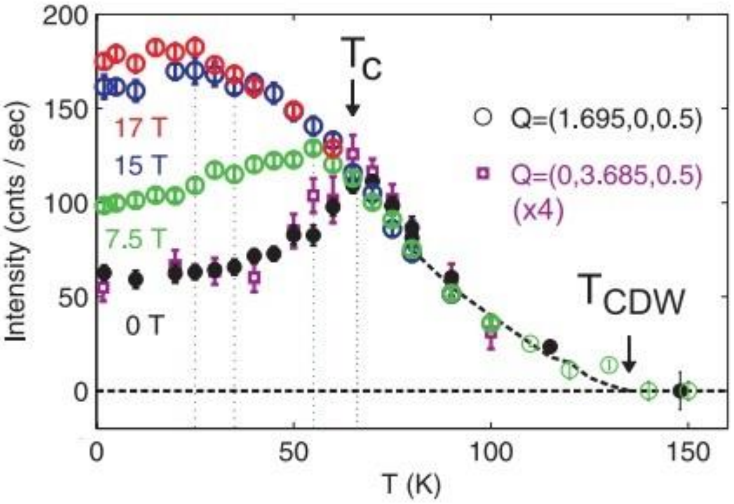

Figure 1.13: Temperature dependence of the intensity of the diffraction peak upon application of external magnetic fields. The decreasing trend below T_c can be reversed upon application of a sufficiently high magnetic field. Square points have been multiplied by a factor of four. Figure readapted by Ref. [32].

Adding another actor, an external magnetic field, it is possible to collect further evidence of the competition between superconductivity and charge order. As a matter of fact, the application of an external magnetic field orthogonal to the superconducting planes weakens or completely obliterates superconductivity. Thus, upon applying a magnetic field it is possible to see a proxy for the behavior of CDWs in absence of the superconductive state. Figure 1.13 shows the results achieved by X-ray diffraction by Cheng et al. [32]: the intensity of the CDW further increases as temperature is lowered below T_c when a magnetic field bigger than 15 T is applied. Cheng et al. also measured the behavior of the width of the peaks in an external magnetic field (result not shown here), finding a trend like that of the intensity: as we increase the magnetic field the width tends to assume a monotonic decreasing behavior with cooling, till it saturates to an almost constant value never reaching zero (that is divergence of the correlation length and complete order never happens). Once again, we are lead to argue that there is a competition between these two ordering phenomena, since the experimental discovery presented here demonstrates that the CDW gets stronger as the superconductivity fades away.

1.2.4.2 Doping

We can find another strong evidence of the competition described above, concentrating on the doping dependence of the phase diagram of hole-doped cuprates. What is observable in most of the different cases, is the fact that the critical temperature T_c around 12% doping level is anomalously low whereas the onset temperature reaches its maximum. On one side, conversely to what we could think, experimental facts show that the onset temperature (displayed in Figure 1.4 for the different cuprate families) scales inversely with the CDW peak intensity and correlation length [10], while one would have expected that the stronger the excitation (higher intensity and larger correlations in the real space) the higher the onset temperature. Indeed, it reaches the highest values for the Bi-based compounds where the strength of the charge order is lower than in other compounds. On the other hand, the suppression of superconductivity around 12% doping level, is higher for the compounds showing stronger CDWs, as it is confirmed by the fact that in some La-based compounds the critical temperature of superconductivity is pushed to zero at p=0.125. Thus, it is not so obvious to find an explanation relating the onset temperature with the strength of the charge order, but it is more evident that superconductivity and charge instability compete, given the anomaly of the critical temperature at a doping level coinciding with the maximum of the onset temperature.

It is worth to mention again the result by Peng et al. [26] who found a charge order peak in Bi2201 way stronger than the usual results achieved in the underdoped region of the phase diagram. In this case charge order has been discovered in the overdoped regime ($p \geq 0.205$), where the superconductivity is very weak since the critical temperature of the samples investigated is smaller than 17K (respectively 17, 11 and 0 K). The correlation length of this new peak is comparable to that of the stripe-ordered CDW in $La_{1.875}Ba_{0.125}CuO_4$ and to the field induced order in YBCO, cases in which charge order is maximum, even though for normal doping levels the strength of charge instability in Bi2201 is weaker than in most of the other compounds. So, this new finding could be again an indication of the competition between superconductivity and charge density waves.

Chapter 2

Simulations

The following section presents simulations and results discussing the topics presented in "*Commensurate $4a_0$-period charge density modulations throughout the $Bi_2Sr_2CaCu_2O_{8+x}$ pseudogap regime*" Mesaros, A. *et al.*, *Proc. Natl. Acad. Sci. USA* 113, 12661 –12666 (2016).

2.1 $4a_0$-period Commensurate CDW in $Bi_2Sr_2CaCu_2O_{8+x}$

Theories based upon r-space strong electron-electron correlations for the electronic structure of hole doped cuprates foresee a $4a_0$ (where a_0 represents the side of the unitary cell of the 2D copper oxide layer) period commensurate charge density modulation (CDM) [6]. On the other hand, experimental measurements of the CDW wavevector, show it increases [33] or decreases [10] continuously with different doping levels. This experimental observation of a continuously changing wavevector upon doping variation, suggests a k-space related behavior of the charge modulation, as opposite to the $4a_0$ period modulation which is theoretically predicted in the framework of a r-space, strongly correlated electron picture. Given the ubiquitous nature of CDM in superconductive cuprates, it is crucial to understand whether the r-space or the k-space character is predominant for CDWs, in order to better understand the driving mechanism for the Cooper pairing in underdoped cuprates.

The greatest difference between theories based on real and reciprocal space is the fact that they predict two different relationships among the different ordering phenomena, taking place in high T_c superconductors. In particular, the k-space point of view expects a competition among ordering phases, while r-space theories predict the intertwined presence of the different phases generated at the same time by microscopic interactions. Following this dichotomy, two possible interpretations for the known experimental results are possible: (i) the wavevector Q of the CDW is truly incommensurate or (ii) the CDW is modulated with a periodicity Q_0 dictated by r-space interactions (locking it to a $4a_0$ periodicity) and the measured value Q_A is the result of the effect of discommensurations and of the disorder superimposed to the coherent charge modulation. The first case is related to a k-space context, in which the evolution of the position of the peaks in the reciprocal space follows the continuous changes of k_F (the Fermi wavevector) with different doping levels. To better illustrate the second option, it has to be said that Mesaros et al. distinguish between a conventionally-defined wavevector Q_A, retrieved from the analysis of experimental data measured by scattering and diffraction techniques, and an intrinsic local wavevector Q_0 (the "real" wavevector of the charge modulation) which is more easily accessible thanks to real space STM measurements. The two (Q_A and Q_0) are different owing to the presence of discommensurations.

2.1.1 STM Measurements and Discommensuration Theory

Compared to other techniques, STM measurements allow to achieve the real space order parameter of the CDW, that is it can probe directly the spatial electronic modulation of the surface states. STM is also powerful because it measures not only the modulus of the periodic distribution of charge but also the phase. This information is a huge enrichment. On the other hand, this method has also major disadvantages: it requires materials whose surface is flat and with no defects, it probes only surface states and it is very slow (as already discussed in the first chapter 1.2.2.2). The first issue restricts the range of cuprates suitable for STM to the Bi-based family only. In fact, cuprates are in general brittle and it is very difficult to achieve a clean and uniform surface. Moreover, the situation is even more complicated since we need a good control of the doping level for the surface layer we are measuring. The second point is associated to one of the intrinsic features of STM. The problem is that the presence of a surface introduces new ingredients to the already complicated task of understanding the ordering phenomena in cuprates. In other words, in principle we are not sure that the CDW we measure in the surface is the same entity we could measure with bulk sensitive probes such as RIXS. This issue has been solved by the work of Comin et al. who demonstrated, comparing RXS and STM data, the equivalence of the excitation probed [25]. Lastly, an STM measurement probes only a tiny region of the space and requires suitable stability in time, temperature and position control.

In Figure 2.1.A is presented a typical STM image representing the d-wave symmetry form factor as: $|\psi_R(r,150\ \text{meV})|=|I(r,150\ \text{meV})|/|I(r,-150\ \text{meV})|$, where I(r,+-150 meV) is the tunnel current measured respectively with a bias of ±150 mV. The oxygen atoms belonging to the same unitary cell present d-wave symmetry (see the section "Form factor" 1.2.3.1). In fact, the atomic orbitals directed along x are out of phase of π compared to orbitals directed along y. In Figure 2.1.B it is possible to see the Fourier transform of the real space order parameter ψ_R.

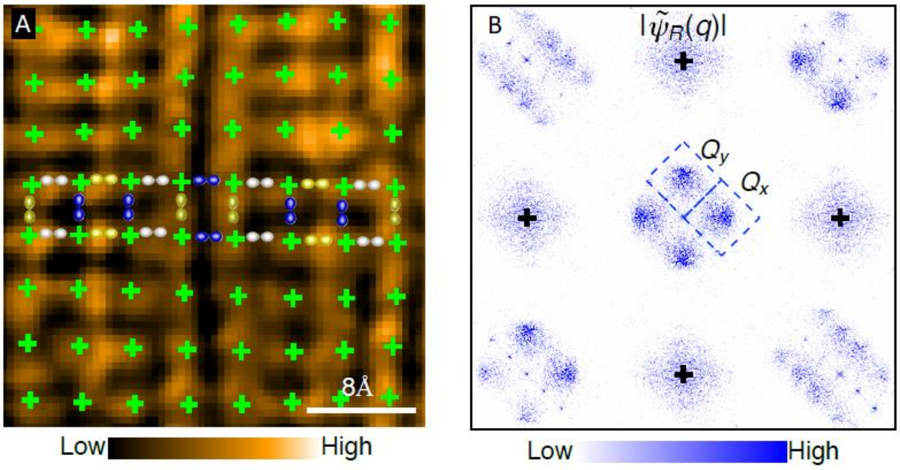

Figure 2.1: d-symmetry form factor. (A) real space charge modulation zoomed to have atomic resolution (see Figure 2.10.A to see modulations in a wider spatial range). Highlighted: Cu atomic positions (green crosses), oxigen p_x and p_y orbitals with a dephasing of π. (B) fourirer transform of the form factor. Inside dashed boxes the peaks related to inter-cell CDW wavevector. Figure readapted from Ref. [6].

Having said about the kind of technique used, the results by Mesaros et al. show that the CDW presents a commensurate character, with a wavevector of 0.25 r.l.u. (even though this experimental achievement is in contrast with many previous results from STM measurements in the same material as testified by Figure 1.9). This observation rules out the interpretation built upon Fermi-liquid interactions for charge modulations. But even if we stick to an explanation based on strong correlations, still the discrepancy between Q_A and Q_0 retrieved by different experimental techniques must be explained. The article points out that the shift in the position is caused by: the discommensurations and the fact that the peaks in reciprocal space are broad and asymmetrical.

2.1.1.1 Discommensurations

Following the definition by McMillan [1], a 'discommensuration' (DC) is a defect in the phase of the charge density modulation (see white vertical stripes in Figure 2.2.B). Different domains are identifiable, where to the space dependent phase determined by the fundamental commensurate wavevector is added a constant, lattice-locked phase shift characteristic of each domain, with a certain relation with the phase shifts of other adjacent domains. If this relation is random the array of additive phase shifts has the only effect of broadening the peak in the reciprocal space, while if there is a coherent relation between adjacent phase slips they cause a variation in the position of the peak at Q_0 equal to the average value of the additive phase constants. To illustrate, we refer to a 1D modulation $\psi(x)$ (see Figure 2.2):

$$\psi(x) \equiv A\, exp\, [i\, \Phi(x)] = A\, exp\, [i\, (Q_0 x + \varphi)] \qquad (2.1)$$

$\Phi(x)$ is the space dependent phase of the 1D wave, Q_0 is the commensurate intrinsic wavevector and φ is the additive lattice-locked constant phase which can assume the discrete set of values: $\varphi/2\pi = 0, 1/4, 2/4, 3/4 + k$, where k in an integer number depending on the coherence of the super-lattice of discommensurations created. To explain the last sentence, we refer to Figure 2.2.B: as it is possible to see the blue solid line (representing $\Phi(x)$ in units of 2π) is the sum of the red dashed line (that is Q_0*x) plus φ. φ is a ladder of piecewise constant values, in the regions corresponding to commensurate domains (colored stripes), joined by straight lines in the region of space where the discommensuration takes place (white stripes), where, as it is possible to see in Figure 2.2.A the modulation has a non-commensurate periodicity due to the effect of φ. In other words, we can say that the wavevector is a piecewise constant function whose value is equal to $0.25*2\pi/a_0$ inside the domains where the CDW is commensurate and equal to an arbitrary value (imposed by the value of φ) in the boundaries where the DC takes place. The space dependent phase $\Phi(x)$ is thus equal to the integral of this piecewise defined function representing the wavevector of the wave in different portions of the surface probed, while φ is equal to $\Phi(x)$ minus Q_0*x. Now for instance, if we want the phase shift to be equal to $+\pi$ from the domain on the left to the adjacent on the right, we are asking φ inside each domain to be equal to $k\pi$, where k is an integer number counting the position of each domain starting from the left. The situation depicted amounts saying that we superimpose to the commensurate wave of the CDW another modulation given by the DCs. This is the reason why we said that the value of k is related to the coherence of the wave: if there is a long-range order among the different discommensurations (i.e. a long chain of equal successive phase slips) then k has full meaning otherwise if one domain has two different values for the phase slips at its boundaries, then we can obtain the same result by choosing k as we want.

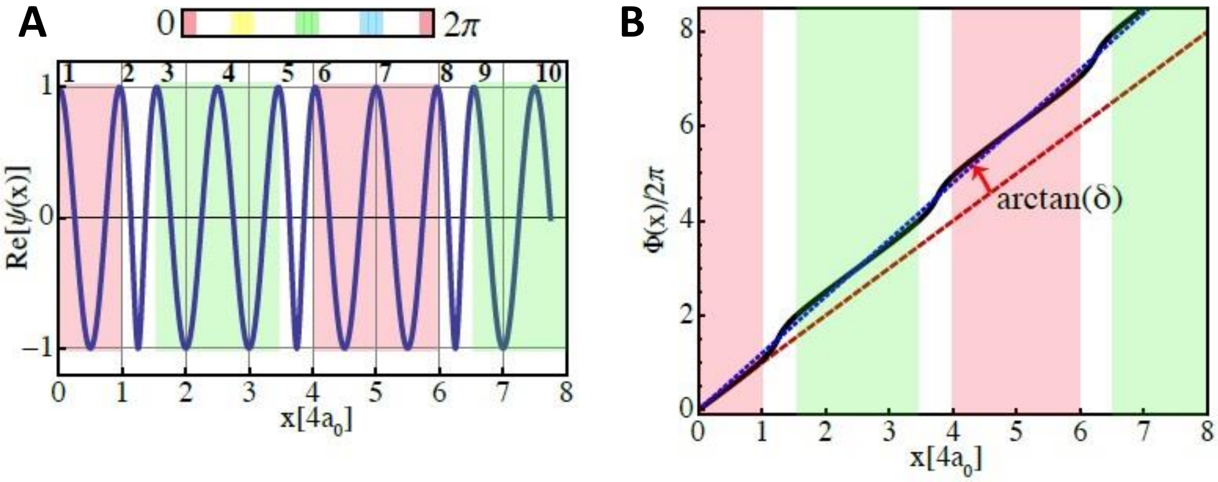

Figure 2.2: (A) representation of the real part of $\psi(x)$ given the choice of the space dependent phase $\Phi(x)$ (B) of the 1D charge density modulation. $\delta=\bar{\boldsymbol{Q}}$-$Q_0$ is the incommensurability. In (B) the blue solid line represents $\Phi(x)$ while the red and the blue dashed lines are respectively equal to Q_0*x and $\bar{\boldsymbol{Q}}$*x. The domains where the additive phase φ assumes a discrete lattice-locked value are represented as the colored stripes (here φ is equal to π or to 0-2π). Note that the slope inside the colored stripes (that is the wavevector of the modulation inside the coherent domains) is equal to $2\pi/4a_0$, while in the white stripes (the boundaries where the DC takes place) it assumes the constant value, that upon integration (i.e. multiplying by x), is required to join continuously the space dependent phase in two adjacent commensurate domains. Figure reproduced from Ref. [6].

Physically, the array of discommensurations allows to accommodate more or less commensurate domains, joined by regions where the wavevector takes values different from those allowed, when the commensurate CDM is frustrated by Fermi surface based tendencies. Through this process, we obtain $\bar{Q}$ as the average wavevector such that the residual phase fluctuations $\tilde{\varphi}=\Phi(x)$-$\bar{Q}x$ average to zero. In other words, $\bar{Q}$ is the slope of the best linear fit of the position dependent phase of the wave (that is the best linear fit of $\Phi(x)$, see blue dashed line in Figure 2.2.B). Mesaros points out that the conventionally defined wavevector Q_A is a bad measure of $\bar{Q}$, which in general could be incommensurate depending on the arrangement of the phase locked domains. If the phase slips of the DC array average to zero, then $\bar{Q}$ = Q_0 (while Q_A obtained by the fitted position of the peak in reciprocal space is often a poor measure of Q_0 [6]). Conversely, if the average of the additive phase constant in different domains (φ) is not zero, then we will have a non-zero incommensurability $\delta\equiv\bar{Q}$ - Q_0. As a final consideration, we point out that here we are focusing just on the disorder related to the phase of the CDW, neglecting the contributions coming from the amplitude disorder in space. Also, the latter source of disorder could provide a super-modulation in the real space which gives relevant effects in the reciprocal space.

2.1.2 Real Space Data Analysis

As mentioned above, the real advantage of STM techniques is the fact that they yield not only the amplitude but also the phase of the Fourier transformed CDM $\tilde{\psi}(q)$, which is not accessible by diffraction probes. On the other side the phase of the modulation in the real space allows to make a map of the DC array and a quantitative assessment of the value of the phase constant inside different domains, referenced to the underlying atomic lattice. Moreover, the knowledge of the phase gives the possibility to implement a new procedure to extract the best linear fit of the phase of the wave ($\bar{Q}$) based on the *demodulation residue minimization* technique [6]:

$$R_q[\psi] \equiv \int \frac{dx}{L} Re[\psi_q^*(-i\partial_x)\psi_q] \qquad (2.2)$$

The equation presented above holds for the 1D case. $R_q[\psi]$ is a functional of ψ depending on q (which in the 1D case presented is just a scalar). After minimizing R_q along the q coordinate we find the value of q_{min} which is a reliable estimation of $\bar{Q}$. ψ_q is the demodulation function, found as $\psi_q(x) \equiv \psi(x)\exp(-iqx)$. Restated in different words, the minimization of R_q is related to the problem of finding q such that the real part of the momentum (found through the application of the derivative operator, besides constant factors) of the function ψ_q is minimum. We want to find the q value of the demodulation ($\exp(-iqx)$) that makes ψ_q as static as possible, that is the same of asking what is the best linear fit for the argument of the CDW, pushing the average value of the residual phase fluctuations to zero.

Extending the procedure to q vectors living in a two-dimensional space (which is the case of layered cuprates), returns a bidimensional R_q which must be minimized both along q_x and q_y coordinates. In reality we will never achieve a value of $|R_q|$ exactly equal to zero, as would happen for the ideal case of a CDW domain with infinite size and perfect coherence. This is due to the finite correlation length of the domains, their different sizes and the asymmetry of the peaks representing the spectral weight in the reciprocal space. The first two characteristics affect the coherence of the CDM and are strictly related with the width of the peak and with its noise. The asymmetrical shape of the peak (joined with its noisy intensity) constitutes a major problem for the fitting, while for the case of the minimization of the demodulation residue it just means we are not able to achieve a minimum equal to zero. In particular, the multiplication of the real space charge density modulation by a complex monochromatic wave having a wavevector equal to q, is equivalent to a translation by the vector q of the peaks in the reciprocal space. q must be such that the peak we want to analyze is translated towards the point (0;0). At this point we introduce a new step useful to reduce the effects of noise. We multiply the shifted spectral intensity by a gaussian function centered in the origin of the reciprocal space (to retain just the contribution of the peak we are interested in, for instance to single out the peak inside the dashed Q_y box of Figure 2.1.B). Therefore, we achieve a distribution in the Fourier space whose first moment is very close to the origin and thus having an almost null momentum. The gaussian (which is the function used to smooth the real space order parameter) has a characteristic length of Λ in the reciprocal space, and it is possible to demonstrate that the procedure is robust to different choices of Λ.

To better clarify, we can concentrate our attention to the dashed box labeled Q_y in Figure 2.1.B. Mesaros et al. argue that the peak of $|\tilde{\psi}(q)|$ (which is the information retrieved by diffraction and scattering probes) is broad and highly asymmetric, leading to a poor fitting and thus to an inaccurate estimation of $\bar{Q}$: that is Q_A (the position achieved from the fitting results). Instead what they do, is to calculate R_q for a range of q values where the magnitude of $|\tilde{\psi}(q)|$ is not negligible (such as the box Q_y in Figure 2.1.B) and to find the q vector for which the modulus of the functional assumes its minimum. The data shown in their article illustrate the fact that there always exists q_{min}, such that $|R_q|$ evaluated in q_{min} consistently parts from the almost constant trend achieved with other q values, assuming a lower value. The value q_{min} thus obtained, is the best estimation of the slope of the linear fitting of the space dependent phase of the modulation (what we called respectively $\bar{Q}$ and $\Phi(x)$ in the 1D example).

Applying all this analytical apparatus to the data from BSCCO at five different hole doping levels (p=0.06, 0.08, 0.1, 0.14, 0.17) Mesaros et al. found out that the wavevectors $\bar{Q}_X$, $\bar{Q}_Y$, minimizing respectively $|R_q|$ for the peaks in the q_x and q_y directions of the reciprocal space (see Figure 2.1.B), are indistinguishable from the commensurate vectors $(2\pi/4a_0;0)$, $(0;2\pi/4a_0)$ and doping independent. This result highlights the fact that the average value of the discommensuration phase slips tends to zero, yielding a commensurate value for $\bar{Q}$. If we image the phase of ψ(r) throughout the space, referencing it to the value of $\bar{Q} * x$ found, it is possible to assess the size of the different domains retaining constant phase inside and the value of this additive phase contribution itself (see Figure 2.10.A). Indeed, it is possible to see that φ assumes only four discrete values $k*\pi/2$, with k=0,1,2,3 (besides the boundary zones between two different domains).

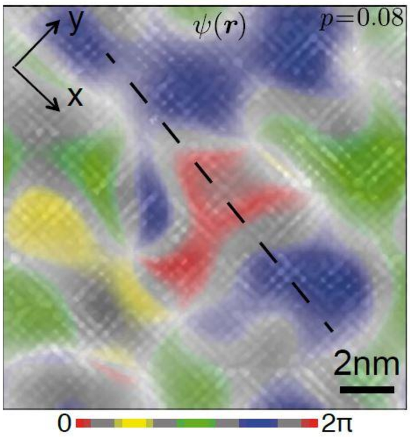

Figure 2.3: Phase of the charge modulation probed by the STM measurement. The phase is referenced to the almost commensurate value retrieved by the demodulation residue technique. Figure reproduced from Ref. [1].

To summarize, the results suggest a commensurate nature for the charge density wave of underdoped $Bi_2Sr_2CaCu_2O_8$. This hints at strong correlations as the mechanism driving CDW formation in this material. The theory of discommensurations embellished with the new phase sensitive technique of demodulation residue minimization, gives the possibility to interpret the data as the result of the competition between Fermi surface weak coupling driven tendencies (which are doping dependent and push towards an incommensurate value of the modulation) and the intrinsic commensurate nature of CDM. The result is a great number of commensurate domains (each one with a discrete value of the additive constant phase φ) arranged in an array, with discommensurations at the boundaries between adjacent domains joining the different values that φ assumes (see Figure 2.3). In the article examined, these conclusions are pushed even forward, since they are supposed to explain the mechanism leading to CDW in all the hole doped cuprates. In fact, referring to NMR results for CDWs in underdoped $YBa_2Cu_3O_{7+x}$ [20] and to reports of a commensurate nature of charge modulations in $YBa_2Cu_3O_{7+x}$ heterostructures [34], the authors affirm that the nature of charge order is commensurate throughout all cuprates. The evidence of this fact in the X-ray diffraction probes is watered down by the effect of discommensurations. In particular, they stress the fact that the continuous evolution of Q_A with doping, found by these experimental techniques, is just the result of a different concentration of defects in the phase pattern of the modulation, which are assembled in such a way that $\overline{Q}$ becomes different from Q_0 (i.e. the value of the DCs doesn't average to zero). They go on claiming that the greatest discrepancy between Q_A and $\overline{Q}$ happens at the lowest doping levels where the density of discommensurations is maximum, causing a higher noise in the peaks of $\tilde{\psi}(q)$ and thus a less reliable fitting. The big advantage of the STM technique is its ability to discern the true $4a_0$ period of the modulation inside the lattice-locked phase domains, even in the case of $\overline{Q}$ different from Q_0, since it can probe tiny regions of the surface of a sample (of the same order of the correlation length of charge order) and imaging the phase (which is necessary to perform the procedure they invented).

As a final remark, we would like to remember though that the results presented here are in disagreement also with other STM measurements. First of all, a doping dependence is found in other STM data (see Figure 1.9) and second, values of the wavevector different from the commensurate value of 0.25 r.l.u. have been measured in Bi-based compounds (for instance 0.21 r.l.u. for Bi2212 and values ranging from 0.25 to 0.31 in Bi2201 [10]).

2.1.3 Results of Simulations and Discussion

2.1.3.1 1D simulations

In this paragraph, we would like to discuss from a different perspective (the point of view of a user of the X-ray diffraction technique) the results by Mesaros et al., previously outlined. Recall that the main assumption, upon which all their theory hinges, is the presence of a 'super-lattice' of discommensurations that causes a shift of the wavevector of the charge density pattern from Q_0 to $\bar{Q}$. The former is equal to $2\pi/4a_0$, which is the commensurate value they think is a universal feature of the CDW in all cuprates, the latter instead is the incommensurate value retrieved as the average value of the space dependent phase throughout a certain region probed. Indeed, the footprint of the X-ray beam impinging on the sample in a RIXS experiment, is several microns wide (4X60 μm^2). So, the signal we retrieve is for sure the average of the contributions coming from a huge number of coherent CDW domains (since we remember that the typical correlation length in BSCCO is 30-40 Å). As mentioned above and as it is possible to see in Figure 2.2.B, in order to achieve an average wavevector different from the commensurate (i.e. to obtain $\delta \neq 0$), we need sizable patches of the CuO_2 planes having discommensurations with equal value between one commensurate domain and another (so we need their average value to be different from zero). In this case, differently from the case in which the additive phase constants sum up to zero and/or are incoherent throughout the space (i.e. the phase slips are not all equal), we have another coherent modulation effect superimposed to the CDW periodicity, provided by the super-lattice of discommensurations. So, the overall wavevector (of the CDW plus the super-lattice modulation) changes its value from Q_0, but satellites peaks must appear together with the main peak correctly centered at $\bar{Q}$, see Figure 2.4.A.

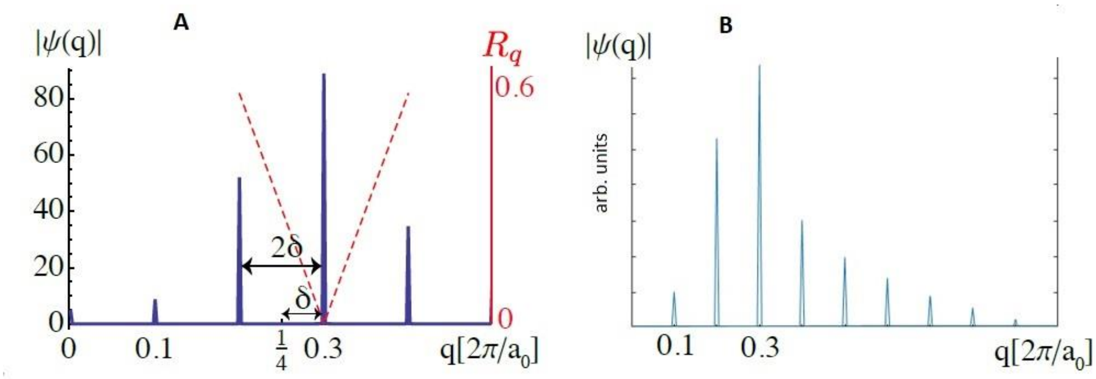

Figure 2.4: (A) Figure reproduced from Ref. [6] representing $|\widetilde{\boldsymbol{\psi}}(\boldsymbol{q})|$ for the 1D case when each discommensuration joins domains with a phase difference of $+\pi$ (see Figure 2.2.B). (B) Simulation reproducing the results of (A) by Mesaros et al.

The spectral density shown in the figure above is the Fourier transform of the real space modulation shown in Figure 2.2.A. We wanted then to find which kind of approximation Mesaros et al. carried out for the phase inside the discommensuration. Figure 2.4.B is the output of the reverse process we did, assuming a value of the phase φ inside the discommensuration region that varies linearly and joins the different constant values of the neighboring commensurate domains, so that the resulting space dependent phase ($\Phi(x)$) is continuous. In other words, $\Phi(x)$ has been found as the integral of a piecewise constant wavevector equal to Q_0 inside the coherent domains and equal to a constant value dependent on both the width of the DC region (the boundary in between two domains) and the difference of the additive phase φ of the two adjacent domains. The agreement between the two spectral densities is quite good. So, from now on, the space dependent phase is assumed to vary linearly from the value at the edge of one domain to the value at the nearest edge of the adjacent domain. This means, if we change our point of view, that the effect of the additive phase φ could be reproduced as the integral of a piecewise constant function equal to zero in the regions where the CDW is commensurate (this gives a constant additive phase inside these domains) and equal to an arbitrary constant value in the regions of the DC. We can therefore look at this latter constant value (called Q_{DC}) as an effective wavevector of the charge modulation inside the DC region. The final value of the average wavevector $\bar{Q}$ will be the weighted average of the wavevector of the charge modulation inside the commensurate region and inside the region of the discommensuration (with the spatial extensions of these two regions being the respective weights in the average).

A critical aspect of this theory is the way it links with the RIXS experimental data. The biggest cause of disagreement is that no satellite peaks are visible in X-ray spectra. Mesaros justifies the absence of these collateral peaks indicating the noise as the cause. In particular, phase (like the DCs), random size of the domains and also amplitude noise (i.e. the amplitude of the modulation varying stochastically in space) are the possible sources of broadening of the spectral density in the reciprocal space.

From the simulations performed turns out that the height of the satellite peaks highly depends on the incommensurability δ. In fact, the bigger the incommensurability, i.e. the difference between the commensurate and the averaged wavevector which is measured, the higher the intensity of the satellites. The sentence stated above can be qualitatively understood in this way: since the $\bar{Q}$ is significantly different from Q_0, we need a strong spectral contribution from other wavelengths to steer the overall wavevector of the charge modulation from Q_0 to match the measured value $\bar{Q}$. Indeed, Q_0 is still assumed to be the main ingredient of the CDW since as it is possible to see in Figure 2.3 the coherent domains occupy the largest part of the probed surface. Following our model (implying a constant value of the wavevector inside the DC region), if we want δ to be big and the size of the discommensuration, where the modulation becomes incommensurate, small compared to the commensurate region, we need Q_{DC} very high due to its low weight in the spatial average.

As said the physical justification of the periodicity of the modulation is the competition between Fermi surface based tendencies (setting the wavelength inside the DC boundaries) and strong correlations imposing a commensurate periodicity of Q_0. In fact, we cannot play mathematical gimmicks such as assuming that the amplitude of the modulation tends to zero inside these 'awkward' boundary regions, because we need their contribution to achieve the shift of the fundamental wavevector in the reciprocal space. In the end, it is a zero-sum game: having fixed the incommensurability δ, if the size of the commensurate domains grows compared to the discommensurations we need a modulation of shorter wavelength there, and we obtain more intense satellites peaks which are not seen in X-ray experimental data. On the other hand, if we want to smooth down the unwanted spectral features around the principal peak at $\bar{Q}$, we can extend the region of the discommensurations. So, a lower frequency for the incommensurate modulation is required (closer to the final value $\bar{Q}$), but in this way the role of the commensurate domains falls behind and the most important actor (at least for the fraction of area occupied) becomes the incommensurate region, betraying the message of the article (see Figure 2.5).

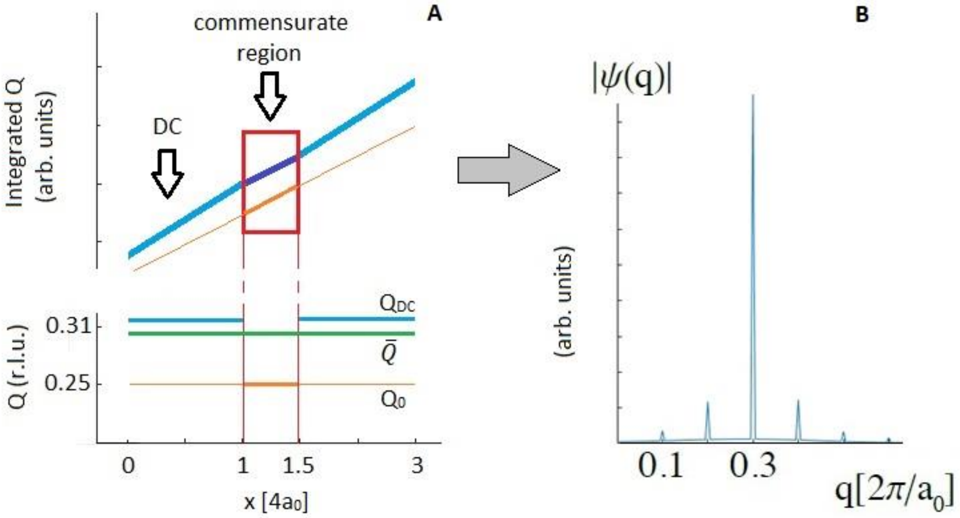

Figure 2.5: (A) larger DC regions: the lower part of the plot shows the piecewise constant wavevector (thick blue and orange lines) which takes the value Q_{DC} inside the discommensuration and Q_0 in the commensurate domain. $\bar{Q}$ (green thick line at 0.3 r.l.u.) is close to Q_{DC} thanks to its higher spatial weight than Q_0. In the upper part of the plot the spatial integration of the wavevector Q is shown. The red square highlights the commensurate region where the wave is commensurate (the purple solid line joining the space dependent phase has the same slope of the orange straight line representing Q_0*x). (B) effect of the larger DC on the spectrum (see Figure 2.4.B): Fourier transform of a complex exponential with a phase equal to the upper part of (A). The value of $\bar{Q}$ wanted is 0.3*2π/a. As it is possible to see, the satellites are decreased because the 80% of the space is covered by the incommensurate modulation whose value is thus close to 0.25*2π/a. In these case, we could say that the commensurate domains assume the role the DCs had before.

The agreement of the theory of Mesaros et al. with the experimental data from X-ray diffraction grows when the value of the incommensurability decreases and when disorder (which broadens the peaks) is introduced. The reason why a lower δ (having fixed the ratio between the DC and the commensurate regions) causes a lower height of the satellite peaks has been discussed above and it has been traced back by simulations to the fact that the value of the wavevector inside the discommensurations is closer to $\bar{Q}$ and therefore to Q_0 (since δ is small). Moreover, if δ is smaller the spacing between the central peak at $\bar{Q}$ and the two nearest neighboring satellites (which have the highest intensity among other spurious peaks and thus are the most annoying even when noise is introduced) decreases being equal to two times the incommensurability itself (see Figure 2.4.A). Now, since the general effect of the disorder (phase, amplitude and domain size disorder have all the same effect on the spectral density see Figure 2.6) is to give broader peaks in the reciprocal space, the principal peak absorbs the two closest peaks and the others get lost in the noise (see Figure 2.6.C).

Referring to Figure 2.6.C we should add that the demodulation residue minimization procedure, though being a very smart and fancy technique, is not so essential for most of the RIXS spectra presented in chapter 4. For sure fully exploiting the additional information coming also from the phase of the CDW increases the precision and the reliability of the analysis, but, at least at low temperature where the signal from the CDW overwhelms the noise, the inconsistency between RIXS data and the discommensuration theory cannot be attributed to poor fitting reasons. In fact, the simulations of the spectral density used by Mesaros et al. to prove the superior ability of the new technique compared to the old fitting procedure cannot be assimilated to a real RIXS spectrum and, as demonstrated by the article itself (see Figure 2.6.C), when the peak is sharp no significant differences are found. So, at least the value of the position retrieved by fitting at low temperature of the RIXS data is a good measure of the position of the peak. In any case the satellites that should be visible if we follow the DC hypothesis are not present.

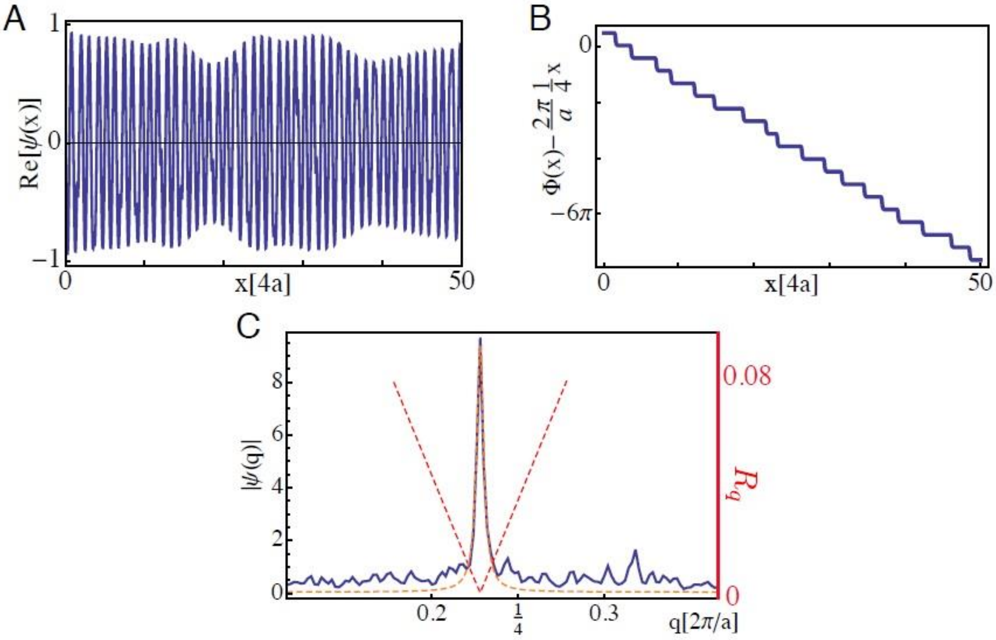

Figure 2.6: (A) real space density $\boldsymbol{\psi}(\boldsymbol{x})$, (B) space dependent phase Φ(x), (C) reciprocal space intensity $|\widetilde{\boldsymbol{\psi}}(\boldsymbol{q})|$ for a CDW with an average wavevector equal to 0.23*2π/a and when amplitude, size and phase noise is introduced. As it is possible to see in this case no satellite peaks are visible. Furthermore, the error between the position of the peak found using the demodulation residue minimization (red dashed line) and the fitting procedure (orange dashed line) is negligible. Figure readapted from Ref. [6].

Moreover, if we concentrate on other materials to assess whether the DCs are ubiquitous in cuprates or not we find the same kind of problems. To be more specific, referring to low temperature data (where the error of the fitting is negligible) of $NdBa_2Cu_3O_6$ and $YBa_2Cu_3O_6$ taken at ESRF and shown in chapter 4, we cannot see the spurious peaks at intervals of 2δ from the central peak, while they should be clearly visible because the incommensurability is quite large (bigger than $0.05*2\pi/a_0$ since the position achieved by the fitting with a Lorentzian line shape is located at values larger than $0.3*2\pi/a_0$). In addition, at low temperature the half width at half maximum of the peak is smaller than the incommensurability, so the peaks should be clearly distinguishable. Even if we assume they were broader than the spacing between them, nevertheless the spectral feature resulting from the overlap should be much broader than the measured signal. It follows that if for $Bi_2Sr_2CaCu_2O_8$ the theory is correct, it could not be true in every situation, due to the absence of the clear tracks left by the super-lattice of discommensurations.

2.1.3.2 2D simulations

To better explore the phenomenology of discommensurations and to assess if extending the concepts explored in one dimension to the two-dimensional case could lead to some unexpected results, also simulations of the CDW real space order parameter in two dimensions are carried out. In particular, the main goal is to try to reconcile the experimental results achieved by the group of Prof. Ghiringhelli with the theory by Mesaros. For this reason, the value of $\bar{Q}$ we want to retrieve is 0.3 r.l.u. and thus the phase jumps between neighboring domains are consequently settled: we want a non-zero average value of φ such that it sums to Q_0 giving the value desired of $\bar{Q}$. So, in this section we do not concentrate too much on the phase noise (random shifts of the phase between neighboring domains), while the noise related to the amplitude is neglected. We will later try to introduce noise in the size of the different domains. The problem of extending the discommensuration patter to a bidimensional space has been tackled in the following ways:

1. First, we assume no size disorder for the domains. So, we divide the control surface in a regular array of rectangles of the same size, with a constant spacing between each other in order to leave the space necessary for the discommensuration to occur. φ, the constant value of the additive phase imposed in each rectangle differs from the four nearest neighboring domains by a fixed amount which can be changed as we like. Following the model explained for the one-dimensional case, we assume a linear behavior of the phase in the region of the DC, such that the value of the phase at the edges of two different domains is continuously joined by a piecewise defined plane of constant slope. In our model ψ(r) is the real part of a complex exponential function whose argument is the sum of the two-dimensional function φ plus Q_0*x or Q_0*y and one excludes the other. In fact, as confirmed by the spectral density distribution of the CDW, where we cannot find peaks along the (1,1) direction (see chapter 1), the charge modulation happens along the x and y directed Cu-O bonds independently. Therefore, the argument of one complex exponential function representing the periodic charge modulation cannot depend on both x and y coordinates. This represents a problem also for the φ described above, since as it is possible to see by looking at Figure 2.7.B it shifts the maximum intensity of $\tilde{\psi}(q)$ away from the q_x axis in contrast with experimental data.

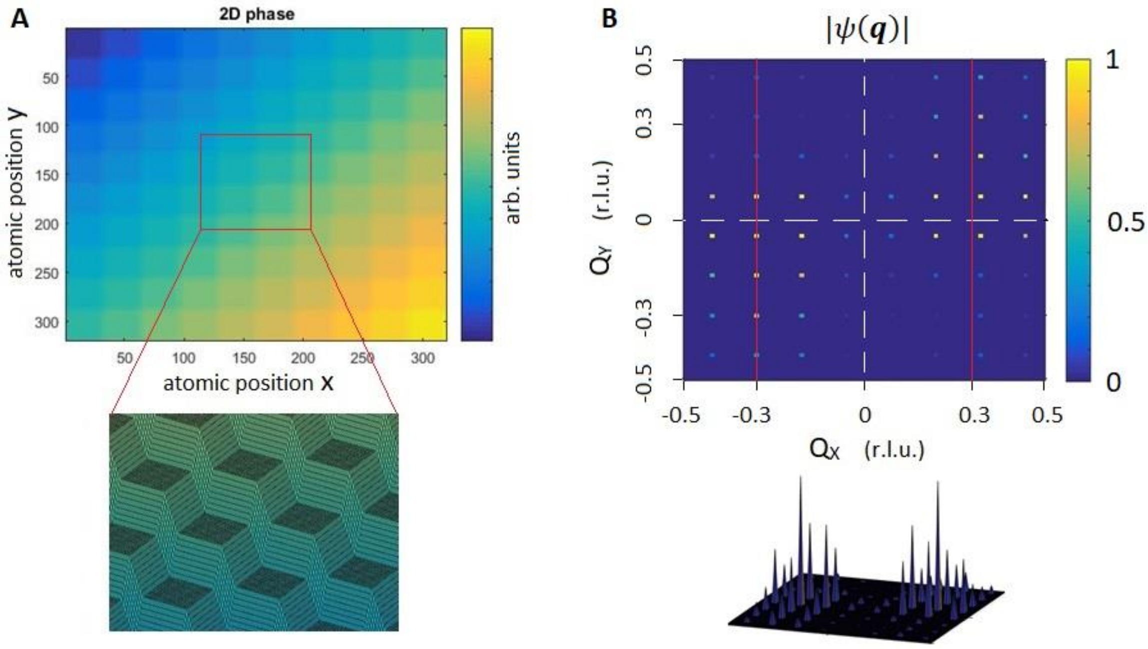

Figure 2.7: (A) additive phase value φ related to the pattern of discommensurations described in point 1. The inset represents a zoom of the phase ladder. From it you can see the subdivision of the control surface in commensurate domains (constant additive phase) and in discommensuration regions (inclined planes). (B) Fourier transform of the real part of a complex exponential function with argument φ + Q0*x. The red lines indicate Qx=0.3 r.l.u. while the white dashed lines indicate the position of the zero. The pattern in the reciprocal space is not perfectly centered with the axes since the matrix representing it is discrete (and even) thus giving alignment problems. The lower part of (B) shows in perspective the spectral density above: a pattern of satellites is clearly visible.

2. As an upgrade to the first model, independent modulations along both x and y directions are introduced. To do this and to maintain at the same time the phase φ described above, we introduce a further subdivision of the control surface. In fact, to every domain is randomly assigned a direction of the commensurate wavevector, directed along q_x or q_y exclusively. In this way, the peaks along both the axes (for negative and positive wavevectors since we imposed a cosine as modulation) of the reciprocal space appear. Further simulations confirm the results achieved in the one-dimensional case: the number and the height of satellites is reduced if the ratio between the area dedicated to discommensurations and the space dedicated to commensurate domains is increased (results are not shown).
3. The next step is to introduce the disorder related to the size of the commensurate domains. As a possible way to model this requirement we divide the control surface in rectangles with different size covering the whole space without leaving any void. To generate this set of rectangles with random size, the following procedure is introduced: the control surface is divides in pixel, each pixel can be equal to one or zero. The result is a sparse matrix of ones, randomly distributed, with zeros elsewhere. The total number of ones to be distributed randomly throughout all the pixels is decided at the beginning; from this number depends the total number of rectangles generated and thus their average area since the area of the control surface remains fixed. We take the matrix described and for each pixel associated with a one (which is like a flag indicating the level inside that pixel is high, whereas

zero indicates the level is low) we calculate its distance from the center of the matrix (if the number of rows or columns is even we cannot find something being really centered and so we take the column or the row labelled with the number resulting from the size in that given direction divided by two, for example if the number of columns is equal to four as central column we take the second). Then, we concentrate on the point whose distance from the center is minimum: the matrix is cut in four submatrices identified by the row and the column associated with this point, which is then changed into a zero (the column and the row where the cut is performed are enclosed in three of the four rectangles). The number of rectangles we get is related to the number of ones of the matrix by the equation N_rectangles=3*N_points+1. This procedure is repeated recursively for all the four matrices thus created in a cascade process till the algorithm receives an empty matrix as input. When the input matrix is empty, the algorithm stops the division process: we have one commensurate domain in which we define the additive phase constant φ. The problem is to join continuously the phase among different commensurate domains, due to their different size. So, instead of discommensurations with a phase varying linearly inside, we achieve a lot of phase jumps and discontinuities. Likely, these discontinuous phase slips are the reason that prevent us from obtaining a shift of the commensurate wavevector to the desired value of $0.3*2\pi/a_0$. In fact, conversely to the cases described above where the shift toward higher wavevectors happens, now our simulations prove that even for a small number of discontinuities of the additive phase the shifting of the reciprocal wavevector is lost (Figure 2.8.B). The array of discommensurations loses its coherence and so it doesn't provide anymore a super modulation which shifts the commensurate periodicity.

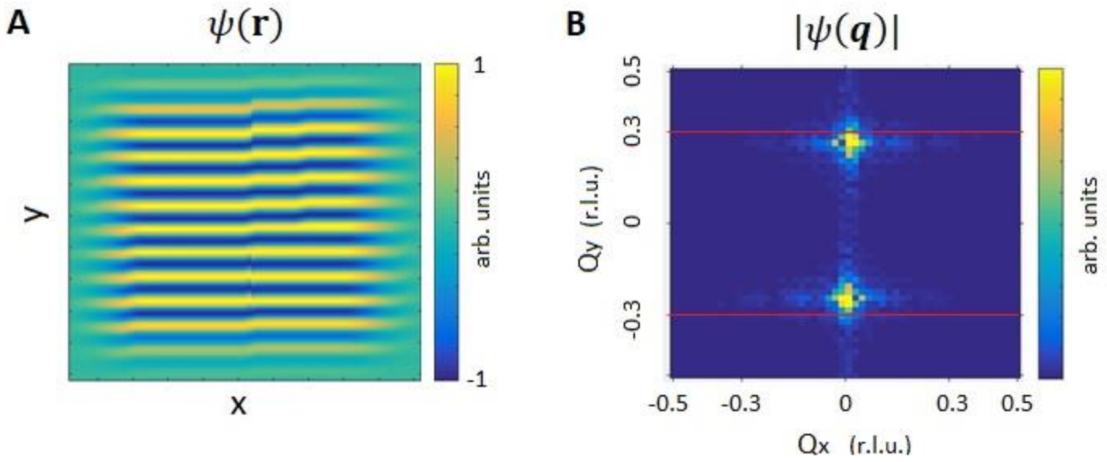

Figure 2.8: (A) real space order parameter under the assumptions outlined. The discontinuities of the phase are visible as "dislocations" in $\psi(r)$. (B) reciprocal space intensity. As it is possible to see the position of the peaks is not shifted towards 0.3 r.l.u. indicated by the red thin lines.

METHODS: our ultimate goal is to simulate the experimental data achieved in two dimensions by the STM measurement (see Figure 2.10.A), thus the complete model used to perform the simulations described above comprehends further assumptions. In fact, we divide the control surface in 'macro-domains' (of random size) characterized by a CDW with a definite direction of the wavevector (along x or along y), see Figure 2.8.A where there is only one macro-domain covering all the control surface. We assume that the CDMs inside different macro-domains are independent one each other. To simulate this independence, we multiplied the modulation inside every macro-domain by a constant envelop with gaussian tails at its boundaries (see the fading intensity at the boundaries of Figure 2.8.A), in order to smooth down the overlap of neighboring CDW. Moreover, a random phase value has been added to the argument of the modulation inside these different macro-domains to be sure the coherence among them is lost. After this division, an additional subdivision of the surface of every macro-domain is performed, following the algorithm described above to create rectangles of random size covering the whole space where the phase takes a definite value and the discommensurations (where feasible) join linearly the phase in different domains.

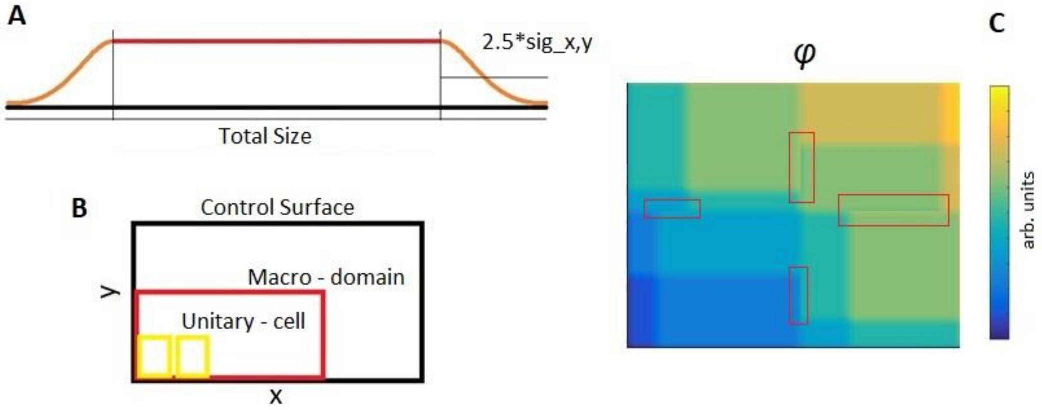

Figure 2.9: (A) envelop of the macro-domain: the gaussian envelop stops at 2.5*$\boldsymbol{\sigma_{x,y}}$ ($\boldsymbol{\sigma_x}$ for the side along x direction and the same for y), after this value the amplitude is assumed to be equal to zero. (B) division of the control surface (black) in macro-domains (red) and unitary cells (yellow). (C) additive phase of the simulation presented in Figure 2.8. Discontinuities of the phase are visible as abrupt jumps of colors between adjacent domains (see the red thin rectangles highlighting four of them) and are the cause for which the average wavevector is not affected (see Figure 2.8.B), even though the additive phase increases in space (from blue in the left-lower corner to yellow in the right-upper corner, see Figure 2.7.A). Note also the random size of the different rectangles as the output of the algorithm described above.

4. Comparing the results of the CDM simulated till now with Figure 2.10.A one of the problems emerging is that the waves directed along x and along y are overlapped in the experimental data while in our model they are kept separated under the assumption of the macro-domains. To overcome this deficit, we run the same simulations described in the previous point two times: once fixing the direction of the wavevector along x and once along y direction. Then we sum the real space modulation. The results are not shown due to the really poor agreement with the experimental data. From this last simulation, it appears clear that the main problem is represented by jumps and discontinuities in the additive phase φ, which cannot be extended smoothly when disorder in the size of the domains is introduced under our assumptions.
5. So, we decide to give up with the coherent lattice of discommensurations and to try just to reproduce the experimental data. As in the two previous cases and coherently with chapter 1 paragraph 1.2.3.2,

the charge modulations are independent entities living inside the envelop shown in Figure 2.9.A. Now the size of each CDW is equal to the macro-domain (which is reduced since it has to accommodate just one coherent domain now, rather than a great number as before) and there is no more need to define the 'unitary-cells' (yellow rectangles in Figure 2.9.B) representing the coherent domains, since φ is constant throughout the macro-domain. Each CDW has its own randomly chosen phase in the range of the four lattice-locked values presented in the first paragraph and its sides vary randomly from a minimum to a maximum value that are tunable parameters of the code. The minimum is constrained by the requirement that only the lateral gaussian tales are present while the surface occupied by the constant part of the envelop is reduced to zero (i.e. the minimum envelop is a gaussian). The maximum is limited by the size of the control surface. The CDW are randomly distributed using a sparse matrix of ones as source for each charge modulation. We allow the overlap of different modulations, which happens with a probability that increases as the density of ones in the sparse matrix increases, by summing the functions describing each one of them. Even though in this way we abandon the possibility of finding a peak at 0.3 r.l.u. in the reciprocal space (if we start from a commensurate value of 0.25 r.l.u.), the agreement with the experimental data is greatly improved as testified by Figure 2.10.

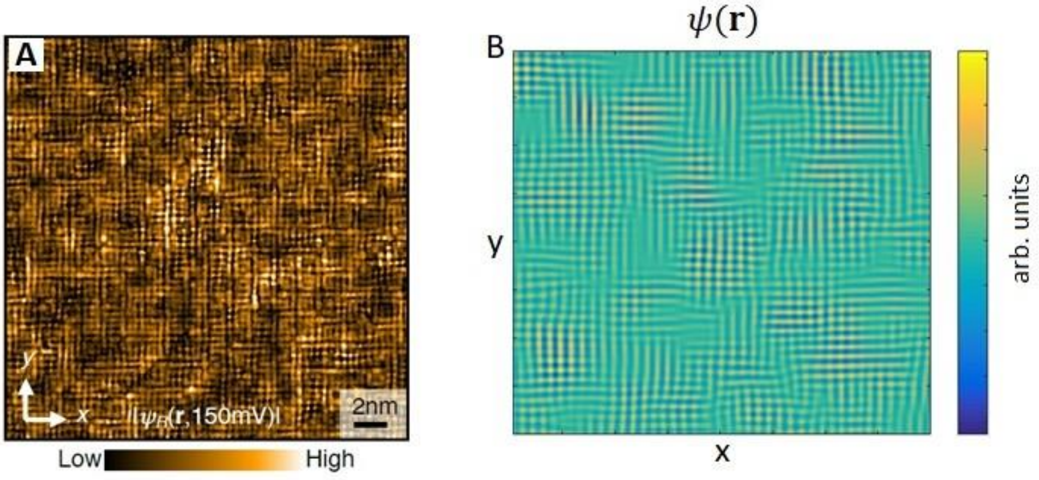

Figure 2.10: (A) experimental data by Mesaros et al. [6], showing the amplitude of the periodic charge density modulation. (B) $\psi(r)$ resulting from the model described in point 5.

Common features of all the models described are found: by changing the parameters to see how the shape of the peaks evolves in the reciprocal space we see a substantial agreement with the trends attained in one dimension. Reducing the size and the number of CDWs the peaks in the reciprocal space broaden. To achieve anisotropy in the reciprocal it is sufficient to set different ranges for the sizes of the modulation in the reciprocal space, i.e. it is sufficient to impose a different coherence length for the x and y directions. In the same way to obtain different peaks in the q_x and in the q_y directions we need to set different sizes for the modulations directed along x, from the CDMs whose wavevector is directed along y.

To summarize, we tried to find the procedure followed by Mesaros et al. in their simulations. After a discussion of how these results merge with the scans achieved by the RIXS technique along high symmetry directions in the reciprocal space, we tried to extend their procedure to the bi-dimensional case, better representing CuO_2 planes where the CDWs live. The product of our model with no disorder in the size of the commensurate domains, still presents the problem related to satellites we discussed in the mono-dimensional case. When randomness in the dimensions of the commensurate domains is introduced, it brings in also an undesired noise in the additive phase. Therefore, the simulations are not able to reproduce the shift of the commensurate wavevector towards values different from 0.25 r.l.u. in the reciprocal space. Then, it is demonstrated how we can achieve a good agreement for the charge modulation in the real space for the case of $Bi_2Sr_2CaCu_2O_8$ presented in Ref. [6] (see Figure 2.10). To do this, it is not necessary to introduce the coherent super-lattice represented by φ whose average value is different from zero. Furthermore, we question the validity of the hypothesis sustaining that the fitting procedure of the peaks found by diffraction techniques introduces a significant error compared to the new demodulation residue minimization.

As a conclusive remark, we stress the fact that the presence of satellites strongly challenges the theory of the coherent array of discommensurations, at least for the cases in which there is a sizable value of the incommensurability. Here we are not discussing the theoretical bases upon which this theory is built, we just point out that referring to Figure 2.7 for the 2D case and to Figure 2.4 for the 1D case (already shown by the article itself), it seems difficult that it can explain a RIXS spectrum (as it should). In fact, even though we assume the narrow satellites to broaden, when they merge all in a single peak (which is a must since in RIXS spectra we cannot see satellites), the width of this resulting peak will be too big compared to the experimental results of scattering techniques.

2.2 Simulation of Confinement Effects on CDW

The following section briefly outlines the results of some simulations performed to assess whether bidimensional confinement affects in some way charge density modulations in $YBa_2Cu_3O_7$.

2.2.1 Introduction

The simulations presented here are meant to evaluate the effect, if any, of quantum confinement on CDW in $YBa_2Cu_3O_7$. This need comes from the controversial results achieved by the group of Prof. Ghiringhelli at ESRF at the beginning of this year. The description of the reasons and the background for the experiment outlined in this section, is taken from the proposal of the experiment itself (Ref. [35]).

The purpose of the beamtime was the study of charge density modulations in $RBa_2Cu_3O_{7-\delta}$ (with R=Y,Nd) nanostructures with size comparable to the CDW correlation length ξ. This experiment should have allowed to assess the evolution of local charge order with the dimensionality of the system [35], thus giving new important information relating the scales of superconductive order and charge order, together with new clues about the interplay between them. In fact, the maximum coherence length of the CDW in YBCO is 10 nm at doping 1/8 and temperature equal to T_c: creating superconductive structures with dimensions of the same order of the correlation length could shed light on the local character of the charge order in the 123 family and, given the ubiquitous character of charge order in cuprates described in the first chapter, also stimulate new research in other compounds. Indeed, the identification and the deep knowledge of the orders taking place in cuprates from many different points of view is crucial for the understanding of superconductivity. Therefore, this experiment aimed at giving an answer (at least in a partial fashion) to these open questions: whether the charge modulation is a dynamical process intertwined with superconductivity or simply a static local order, independent from the superconductive state; the assessment of the spatial distribution of charge order and of the symmetry of the local state; understanding the role of chemical and structural disorder in determining the CDW instability. Relating to this last point we could cite for example, the role the played in $La_{2-x}Sr_xCuO_4$ by the doping with rare earth elements (Nd, Eu) in breaking the perfect square symmetry of CuO_2 plaquettes in the superconducting cuprate planes [10]. In effect, the first proof of stripe order in La-based compounds was found only after Nd-doping of the parent compound LSCO, since the lower size of this rare-earth ion allowed to break the square symmetry which hampered the charge instability to take place. An even stronger signal was measured in Eu-doped LSCO due to the smaller dimension of Eu ions which caused a greater distortion of the parent compound lattice thereby facilitating the occurrence of the broken translational symmetry state induced by the CDW [10]. This example justifies the interest, fostering this experiment, for the structural environment surrounding charge modulations, as a key ingredient in their existence and properties. Moreover, low dimensionality enhances the effects of the locality of charge arrangement, therefore possibly leading to a simplified physical picture [35].

The main goal is to assess the effects of lateral confinement on charge order, but how do they influence the superconductive state? Nawaz et al. [36] demonstrate that the low dimensional patterns created by the group of Chalmers, who produced the samples for this beamtime, leave the superconducting properties of the material untouched. Moreover, the samples brought at ESRF presenter a new amorphous carbon capping, guaranteeing the protection of the nanostructures while leaving unaltered the RIXS signal from the CDW. Characterization of the transport properties of the nanopatterned samples has been performed before and after the experimental session at the synchrotron, ensuring the quality of the active material and that superconductivity has been preserved after the fabrication process and after the measurement process. We anticipate that the results of the experiment where not those expected, since it was not possible to see any signal suggesting the presence of a dispersing CDW as foreseen and hinted by previous trial measurements at ID32 (beamline at ESRF, see chapter 3) on an array of underdoped nanopatterned 65X500 nm^2 YBCO.

While measurements on YBCO thin films (1 and 2 uc) have been already carried out [35], proving the persistence of the signal related to charge order, although weakened, at (0.31, 0, L) (once more demonstrating the two dimensionality of charge instability in cuprates), experiments meant to delve into the effects of lateral in plane confinement have never been performed. RIXS is essential, due to the expected low signal levels for this kind of experiment (as it was the case for thin films): what is important is its ability to resolve in energy between the weak modulation at different values of the in plane transferred momentum $q_{\parallel}$, caused by charge order in the elastic region, and the other inelastic excitations constituting the background. Energy integrated RXS setup is not suitable to perform this kind of experiment, even though the only dispersing signal is the one we want to measure, owing to the low signal to noise ratio levels. In fact, since the inelastic excitations are weakly varying in momentum space, we could in theory use RXS, which provides faster measurements, to detected the quasi-elastic, dispersing CDW from the nanopatterned structures. In reality, we need to be able to concentrate over the elastic region only to extract as much useful information as possible, given the feebleness of the scattered photons by the charge order. Another reason why the special features of ID32 beamline at ESRF are required, is the need for a high energy resolution of the incoming photon beam and an excellent control of the beam position on the sample. In fact, the new ERIXS instrument (which will be presented in the next chapter) at ID32 provides diffractometer quality control of the continuously varying scattering angles and of the beam position over the sample.

The samples brought at ESRF were 30 and 50 nm thick RBCO films grown on a $SrTiO_3$ [100] substrate at two different doping levels: p=0.125 where the CDW is expected to be strongest and p=0.16 where we have the peak of the critical temperature. Also, heavily strained nanostructure films grown on MgO [110] surface were taken to the beamline, to assess a possible interconnection between the role of strain in the 123 family and charge modulations. For each sample four different kind of patterns were present: 50X50 nm^2 and 200X200 nm^2 islands, nanostripes 70X500 nm^2 aligned both along [100] and [110] directions. All these different kinds of structure were fitted in a single slab as homogenous regions of patterning with size 0.5X3 mm^2 (see Figure 2.11). The distances between different nanostructures is kept constant and equal to 100 nm. Furthermore, an unpatterned film has been brought for every type of material and substrate, to provide a reference value of the normal CDW strength. We will refer to these unpatterned samples in chapter 4 where their RIXS spectra will be discussed.

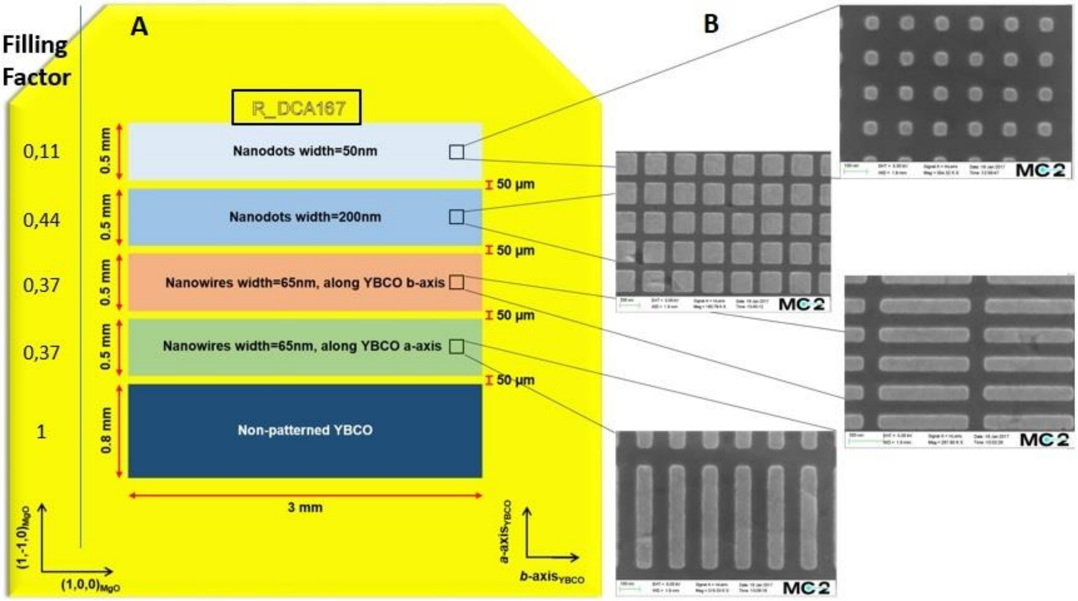

Figure 2.11: (A) Cartoon showing the array of regions containing different patterned structures and the unpatterned region for each material. On the left, you can also see the different values of the filling factor. Photo readapted from HC 2703 logbook. (B) SEM image of the nanopatterned structure (65X500 nm^2) used to prove the presence of the CDW signal. Image taken from Ref. [35].

To summarize, the idea of the experiment is to measure the energy-momentum maps of RBCO at Tc (where the CDW is strongest), to probe the nature and the features of the charge order under later confinement in the superconducting 123 family. ID32 RIXS facility is necessary because of the signal enhancement required to detect the small variation in the elastic signal due to CDW over the bigger background signal from the inelastic excitations. In fact, based on previous indications (for example the measurements on thin films) the signal from the patterned regions might be too weak for other diffraction facilities.

2.2.2 Why the Simulation are Performed?

As mentioned above, unfortunately the measurements on the patterned regions of the material did not give the hoped results. To better explain, the elastic range of the RIXS signal coming from basically all of the measured nanostructures, does not present any kind of dispersing feature hinting at the presence of a CDW. What it is possible to recognize is just the constant elastic background which does not disperse through different momentum values.

Thus, we tried to develop a simple model aiming at finding whether there should be some intrinsic reason for this experimental achievement. In particular, imposing some spatial constraints and using the tool offered by the Fourier transform to switch from the real to the reciprocal space, we want to see whether it is possible to achieve a non-dispersing Fourier transform (at least along the H and K directions of the reciprocal space that were scanned during the experiment) starting from the assumption of static charge density modulations. Since in any of the experimental configurations probed (i.e. for all the sizes of the nanostructures) the side of the superconductive island is larger than the correlation length of the charge modulation, we start from the beginning assuming the presence of the charge modulation. In other words, we can assume that the CDW is not killed from scratch by the too restrictive spatial confinement. Regarding the energy-momentum information retrieved with RIXS, we concentrate on the elastic region only, assuming static modulations in the real space, without time dependence. That is, we make the hypothesis of a zero frequency-energy excitation.

Another possible reason for the absence of the CDWs in the RIXS spectra is the fact that they are really not present. Indeed, one possibility is that during the fabrication process the etching mechanism, used to create the nanopattern, damages also a sizable portion of the sides of the material causing the superconductivity and also the charge order to disappear or to be relegated in an area smaller than the size of the superconducting material. The fact that the measurement of the transport properties gives positive results is for sure an indication of the goodness of the nanostructures, but it doesn't give a complete certainty. This happens because of the different production mechanism employed in the latter case: for example, to perform the resistivity check of one nanodot two opposite sides of it are covered with gold contact pads to provide electric contact. Therefore, the gold contacts may protect from the etching two sides and thus reach directly the inner region where the capping layer effectively protected the material. If this is the case, the transport measurement probes just the smaller channel where the properties of RBCO are preserved, thereby yielding a positive result for the transport properties assessment.

The last possibility we thought about, is the fact that the filling factor is in any case too low to give a sizable signal of the CDW over the elastic reflection. In fact, given the constant spacing of 100 nm between the different nanostructures in both the two directions of the plane (see Figure 2.11.B), it is possible to calculate the filling factor (FF), as the ratio between the superconducting portion of the sample and the substrate, for every type of patterning: FF=1/9 for the 50X50 nm^2 nanodots, FF=4/9 for 200X200 nm^2 islands, FF=0.34 for the nanostripes 70X500 nm^2 wide (see Figure 2.11.A on the left). So, always less than half of the total area is covered by superconducting material, if we assume no damage at all from the fabrication process. Moreover, as we will see in chapter 4, the MgO substrate plays a relevant role in shaping the surface of the material. The [110] direction on which the RBCO is grown induces not only strain, but also a reconstruction with a consequent super-modulation. Thus, the peak for the unpatterned film (which is the only region giving a consistent signal) in the reciprocal space doubles and we can see two replicas of the same peak at a different wavevector from the usual one. This strange surface effect could possibly add some contribution to the elastic peak, adding some further complication to the situation.

2.2.3 Assumptions and Model

Even though in our model we are not able to reproduce the elastic signal, which instead plays a major role in the experiment described, nevertheless we assume that charge order is present and we perform some simulations to see whether it is intrinsically hampered by the particular geometrical constraints imposed by the patterned structure or not.

Starting from the last bidimensional model developed in the previous section of this chapter and from what written in chapter 1 about the nature of charge modulations, the following assumptions are made: (i) unidirectional symmetry of charge modulations (see paragraph 1.2.3.2), (ii) constant envelop with gaussian tails for the charge density wave (see Figure 2.9.A), (iii) no discommensurations are taken into account, the wavevector of the modulation coincides with the position of the peaks in the reciprocal space (if any): the phase of every coherent charge wave is independent from others (no super-lattice of phase slips is introduced), (iv) minimum size for each coherent domain below which no CDW can be present and (v) to add some new ingredient we assume that the charge modulation can tunnel with a certain wavelength (which in this model has been treated as an independent parameter to be chosen when running the simulations) outside of the quantum well. In other words, to keep the model as simple as possible, we regarded charge modulations as independent quasi-particles. Therefore, they are seen as normal modes of the system and the spatial overlap of two different modulations results just in a sum of their effects (the values of their real wavefunctions simply sum up). The hypothesis of tunneling (which in this model is not driven by any particular physical requirement related to the peculiar nature of the charge order in cuprates) can be justified as a consequence of the previous assumption of the quasi-particle nature of CDW. We also introduced it trying to enrich the range of possible outcomes from our simulations.

After the description of the of the local properties assumed for the single charge modulations we go on describing how they are arranged in every single nanostructure of RBCO, which is actually treated as a potential well where the charge order can exist, conversely to the inert substrate where CDWs can just penetrate with an exponentially decreasing wavefunction. The number and the spatial distribution of the CDWs throughout the control surface, is controlled by a sparse matrix of ones (where the dimensions of the sparse matrix coincide with the number of points over which the region of the superconducting nanostructure is defined). As in the previous section, each one of this matrix represents a source for one charge density modulation. The lateral dimensions of each excitation are retrieved as a random number chosen in a fixed range of values. The maximum and the minimum value of the four different ranges, coming from the four combinations given by the two possible directions of the wavevector (q_x and q_y) times the two lateral dimensions of the rectangular envelop of the CDW, are initial parameters to be given as input to the code. If the distance between a source of CDW and the side of the RBCO nanostructure is smaller than the lateral side of the envelop (determined randomly within the relative range of allowed values) there are two possibilities as outlined in Figure 2.12: (i) the wavevector of the modulation is parallel to the side of the RBCO domain: in this case the lateral dimension of the charge modulation is cut in a way such that the CDW fits inside the domain, approaching the boundaries of the material with zero amplitude. In other words, we impose that the point where the exponential envelop of the gaussian tail begins is far exactly 2.5σ from the side of the nano-box (in fact, we make the assumption that at 2.5σ the amplitude is zero). If the source is closer than 2.5σ, then it is shifted inside, in such a way that its distance from the boundaries becomes exactly 2.5σ. (ii) if instead the wavevector of the modulation is orthogonal to the side of the RBCO domain, we allow the CDW to tunnel outside the allowed perimeter, where its amplitude behaves as a decreasing exponential till a distance equal to 5λ (where λ is an input of the code) and then is put equal to zero. Finally, the dimensions of the quantum dot of active material cannot be smaller than a gaussian, representing the minimum size allowing the existence of a charge modulation.

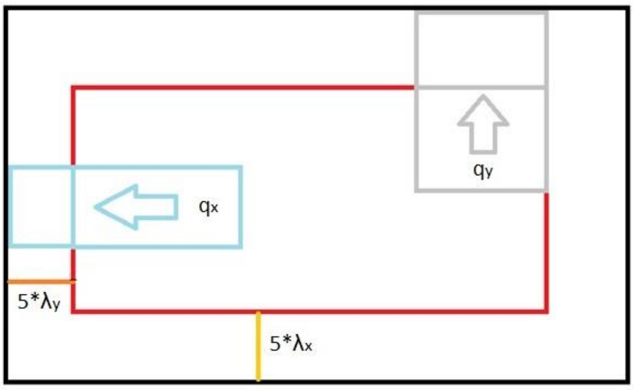

Figure 2.12: What happens when a CDW is too close to the nanostructure boundaries. If the wavevector of the modulation is perpendicular to the side of the quantum well, a tunnel process happens and the wavefunction exponentially decreases outside. On the other hand, if the wavevector is parallel to the side of the box, the lateral width of the CDW is cut in order to make it approach the side of the box with zero amplitude (i.e. with the tail of the gaussian envelop, where the wavefunction is supposed equal to zero). The last possibility is that the source is closer to the boundaries than the size of the gaussian envelop: in this case the source is translated inside as much as required to fit the whole gaussian tail.

The arrangement of nanodots forming the patterned region is lastly created: the code asks as inputs how many atoms along the x and the y directions are needed to form the nanostructure, the number of nanostructures in the x and y directions of the whole control surface and the filling factor. After being calculated in the real space the wavefunction is Fourier transformed to simulate the possible outcome of the RIXS signal.

2.2.4 Results and Discussion

The kind of simulations described are quite heavy for the computational capacity available. Therefore, in the first stages, simulations with only one nanostructure have been carried out. The periodicity of the modulation has been set equal to 0.31 r.l.u. for all the different types of simulations described here. From different configurations of the initial parameters it is possible to say that the four peaks, related to the cosines with a wavevector along each one of the two orthogonal Cu-O bonds, are always present. The trends found in the former section are confirmed, with the intensity of the peaks along the q_x and the q_y directions of the reciprocal space determined by the number of CDW having the corresponding wavevector. Concerning the anisotropy of the peaks, we see that the ratio between their widths varies inversely with the ratio of the correlation lengths along the two perpendicular directions of the real space (see chapter 1). Moreover, the width scales inversely with the size of the nanostructure and the correlation length of the domains (the bigger the area where the modulation is present, the narrower the peaks in the reciprocal space). The tunneling of the CDW outside the perimeter of the 'quantum well' and the value of the parameter λ controlling the extension of the tails (see Figure 2.13.B), turn out to affect only the peak in the origin of the reciprocal space: in fact, the bigger λ and the greater the number of tunneling events (tuned via different ratios between the dimensions of the nanostructure and the range of those of the CDW), the higher the peak related to the zero spatial frequency.

Thus, with a single structure and by changing the available set of parameters we cannot find a configuration where the peaks in the Fourier space are suppressed. The next step was to increase the number of nanostructures in the control surface: we have also to keep in mind the particular shape of the footprint of the beam which may be quite important in this context. Indeed, the spot size of the beam is 4X60 μm^2, so the shape of the nanopatterned region probed is heavily constrained by the beam properties. For this reason, simulation with both an equal and a different number of dots in the two dimensions are made. Figure 2.13 shows the result of a simulation with an array of 5X5 nanostructures. The filling factor has been imposed equal to 1/9 and every nanostructure is made by 25X25 atoms. In each quantum well 100 CDW are put: 50 with a wavevector directed along x and 50 along y. Given the big number of sources, and the small size of the domain relatively to the CDW coherence length (of the same order of the side of the nanostructure since the maximum size allowed for their ranges is the equivalent of 40 atoms) there are a lot of overlap events inside the quantum wells and this accounts for the checkerboard shape of the modulation. The peaks are symmetric because the four ranges are all equal. As it is possible to see, a weak peak is appearing in the origin due to the continuous wave signal introduced mainly by the tunnel events. The effect of the super-periodicity required to form the array of nanostructures is visible as a sort of "grid" modulating the peaks, see the inset of Figure 2.13.A .

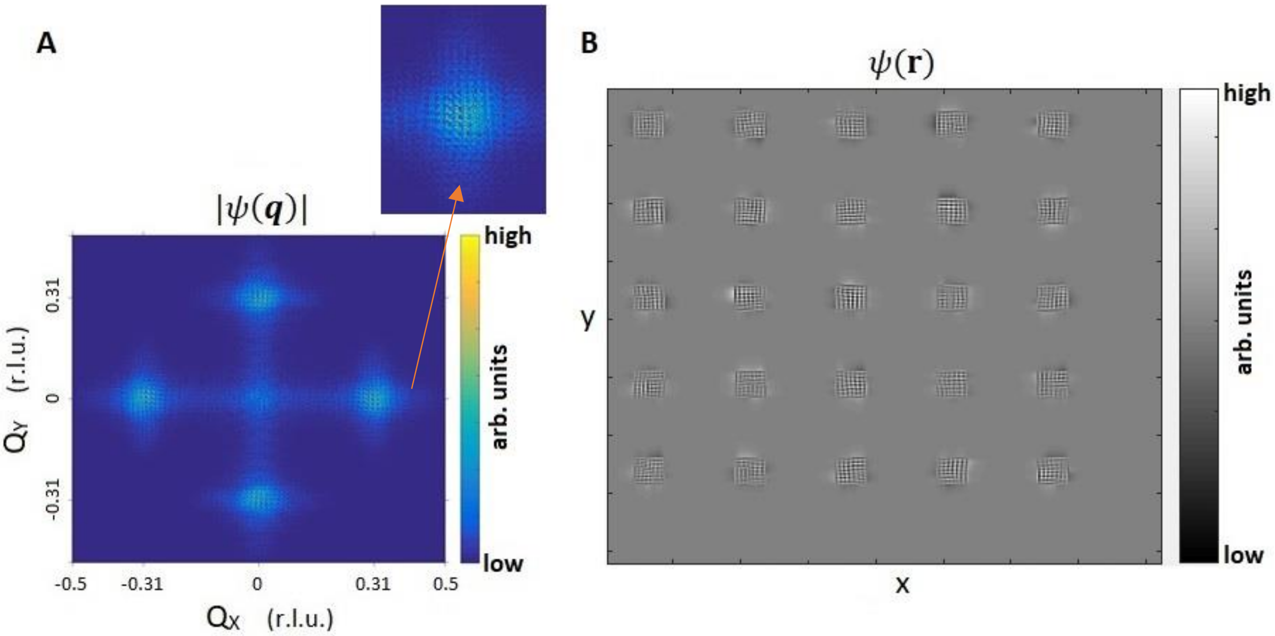

Figure 2.13: (A) Fourier transform of the real space configuration made by an array of 5X5 nanostructures of 25X25 atoms each presented in(B). In (B) it is possible to see how the wavefunction extends outside of the nanostructures with exponential decaying behavior. The filling factor is equal to 1/9.

After the simulations performed with an equal set of parameters for the inputs related to x and y directions, we tried to see what happens when a number of dots respecting the constraints imposed by the beam spot size (4X60 μm^2) is assumed. To explain the results achieved, we refer to Figure 2.14 showing the modulus of the spectral distribution obtained from an array of 2X30 nanostructures composed by 100X100 atoms each, with inside 10 CDW with a modulation directed along x and 10 with a wavevector directed along the y direction. Only 20 sources have been simulated to reduce the computational effort required (the memory was not enough). The result is a weaker signal than that coming from the simulations showed in Figure 2.13. The peaks in this case are also narrower because the size of the real space where the modulations are present is wider. Furthermore, now the ranges have been initialized with different values to reproduce the anisotropy found in the experimental data of Comin et al. [30]. In particular, we imposed a longer coherence length of the CDW along its side parallel to the wavevector than for the side orthogonal. This results is the shape of the peaks showed in Figure 2.14. Since no different ranges are introduced for the waves directed along x from those directed along y, the peaks in the H and K direction are equal (but changing the inputs it is possible to achieve the same results retrieved experimentally where the peaks along H and K direction are different (see 1.2.3.2).

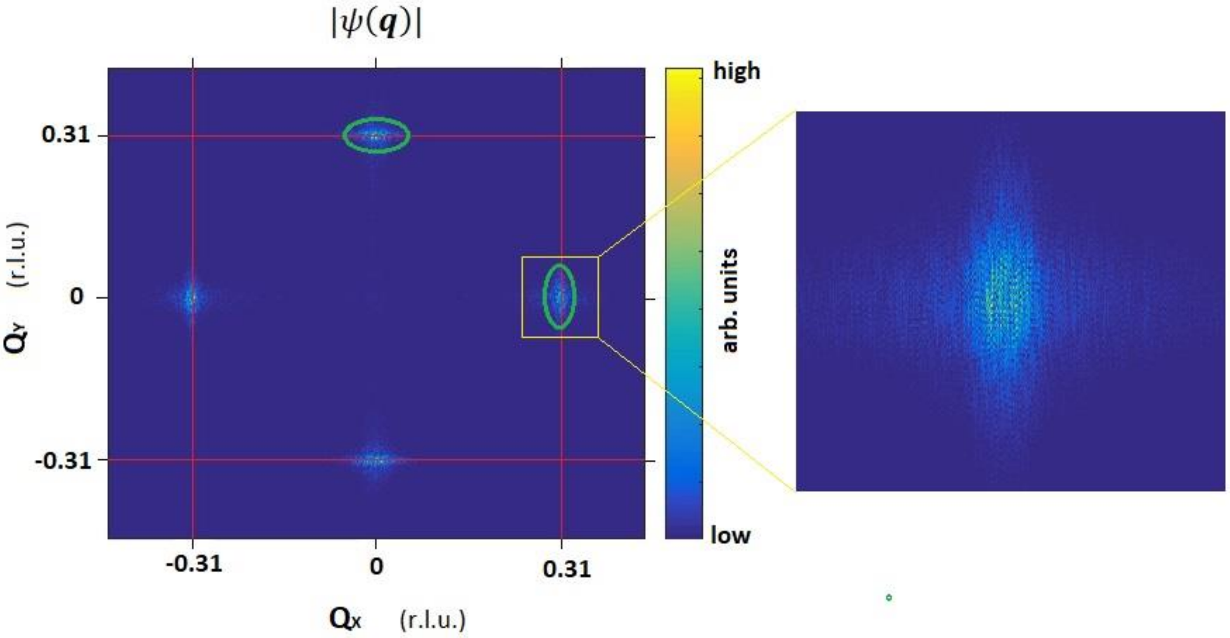

Figure 2.14: Modulus of the spectral density for the case of two rows and thirty columns of nanostructures. The ratio between the rows and the columns in this way reflects the the shape of the footprint of the beam. Inset: zoom of a peak showing its elongated shape. The simulations reproduced the results showed in paragrph 1.2.3.2, since bigger ranges for the coherence length of the CDW along the direction parallel to the wavevector have been imposed, yielding the asymmetric shape of the peak found by RIXS measurements (Comin et al. [30]). The peaks along Q_X and Q_Y are equal (see the green circles) because the ranges set for both the directions of the wavevectors are equal here.

To summarize the simulation performed are not able to explain the experimental results achieved. Nevertheless, they prove to be useful since they can reproduce with some similarity the results found in literature (for example the asymmetrical shape of the peaks). This could possibly be regarded as a further confirmation to the hypotheses on which these simulations hinge. In particular, the most relevant parameters appear to be the those related to the local size of the CDW (their coherence length) and their unidirectional character, giving peaks only along the (0,1) and (1,0) directions of the reciprocal space. Moreover, the assumption made on the way these modulations interact among each other are consistent to the real space data retrieved by STM measurements, since here we are able to find the same checkerboard-like structure (Figure 2.13.B) starting from assumptions coherent with the picture given by the diffraction probes.

Chapter 3

Experimental Methods

3.1 Soft Resonant Inelastic X-Ray Scattering

X-rays have been used for the study of the internal structure of matter since a long time ago. They are sensitive to the electronic cloud surrounding nuclei due to the radiation matter interaction. In the first realizations of x-ray based techniques the energy of the incoming photon was quite immaterial [10]. The first indications of the relevance of resonant processes, providing enhancement of the signal, came by the work of De Bergevin and Brunel [37] who managed to detect antiferromagnetic peaks in NiO, thus demonstrating the sensitivity of x-rays to spin order. After this first demonstration, x-rays started to support and complete the role of neutrons in the study of the properties of matter. Soft x-ray absorption (XAS), was one of the first experimental soft x-ray scattering techniques employed to measure the resonances of shallow core levels of rare earths compounds displaying rich multiplet features. The use of synchrotron light sources greatly increased the effectiveness of this technique, providing monochromatic beams and the intrinsic control, by the relativistic generation process, of the polarization, allowing the measurement of magnetic dichroism effects. After the first pioneering studies with hard x-ray (about 8.9 KeV) inelastic scattering on Cu K edge, Abbamonte et al. in 2002 were the first to perform x-ray scattering on cuprates in the soft energy regime: at the O-K (530-550 eV) and Cu-$L_{3,2}$ (920-960 eV) resonances of La_2CuO_4 [38]. These measurements came after the demonstration of the sensitivity of these two absorption edges to the hole doping electronics in cuprates, which actually involves exactly these orbitals (as said in paragraph 1.2.3.1) [10].

Resonant inelastic x-ray scattering (RIXS) is a *photon in – photon out* synchrotron based spectroscopic technique [8], in which photons are scattered by the charge configuration inside the material. Its peculiarities and intrinsic properties made it one of the most popular techniques for the investigation not only of high temperature superconductors and cuprates but for the study of matter in a variety of different states in general. In this chapter, we will concentrate our attention on the case of an incoming photon beam whose energy has been tuned to the Cu L_3 absorption edge (from the $2p_{3/2}$ orbital to the 3d orbital of copper), since we are interested in the study of the phenomena taking place inside the CuO_2 planes of the superconducting cuprates. Therefore, for the study of cuprates, soft-RIXS (energy of the incoming beam smaller than 1.5 KeV) rather than hard-RIXS is performed (because we are interest in phenomena involving the 931 eV wide copper L_3 resonance). The biggest drawback of soft x-rays is the fact that they cannot be analyzed through the conventional Bragg optics setup. The energy resolution achievable is thus not so high as in the hard x-ray regime. Another problem related to the soft energy range is the need for vacuum based facilities: in fact, the attenuation length of the radiation scales with the third power of the photon energy. This implies the need for vacuum chambers for photons whose energy is smaller than the indicative value of 5 KeV [10]. In fact, a beam of photons at 10 KeV (1 KeV) has an attenuation length of 3 m (3 mm). Therefore, for the typical experimental scales (of the order of few meters in conventional spectrometers), the hard x-rays regime does not require vacuum since with the high brilliance of the synchrotron sources a moderate loss of the incoming signal is acceptable (in any case vacuum must be preserved in the long pipelines carrying the light from the storage ring to the sample stage).

3.1.1 Properties of RIXS

The information that we can achieve from RIXS is both related to the electronic structure of the material and to its magnetic excitations. Thus, by means of this technique we can access lattice, charge, orbital and magnetic excitations. Moreover, compared to neutrons (which do not couple with charge excitations), it requires much smaller samples to work with, while having a greater bulk sensitivity than electronic probes such as ARPES or STM. The high resolving power of the new generation spectrometers (see next section) and the new generation synchrotron light sources, allow to use this technique to probe low energy excitations of the atoms in cuprate planes. The main difference from non-resonant techniques is that the exploitation of the resonance enhances the signal at the point that a single hole located at the Cu-L_3 or O-K absorption edges scatters as strongly as 82 electronic charges not involved in the resonant process [38]. Since the RIXS experimental signal depends on the square of the scattering amplitude the effective enhancement is of order of 82^2 [10]. This is a key point for the success of RIXS, because it combines the possibility to probe weak ordering phenomena, thanks to this huge enhancement given by resonance, with the variety of mechanisms in which radiation couples with matter.

The combination of these aspects yields a signal, for example from charge order, which strongly depends on the incoming photon energy as it is possible to see in Figure 3.1 (which represents the first direct measurement of charge order in a superconductive sample by Abbamonte et al. [39]): the intensity is strongly attenuated out of resonance, proving both the enhancement of the scattering by the resonant interaction and the fact that the CDW is coming from a modulation of charges present on the Cu-3d and O-2p orbitals. This explains the results described in paragraph 1.2.2.3 by Ghiringhelli et al., where the strong dependence of the signal on the energy of the resonance allowed to distinguish between the copper atoms in two different crystallographic positions. In the detection of weak phenomena like charge order in cuprates the resonant enhancement is vital: non-resonant techniques weight the same way all the charges in the material, so the signal from the CDW involving fractions of electrons per atom is completely overwhelmed by lattice peaks, generated by all the other electrons of the atom. Actually, charge order can be detected by non-resonant x-ray probes and by neutrons as a small shift in the position of the Bragg peaks, due to electron-phonon coupling: the charge density wave affects the lattice distorting it. Abbamonte et al. [39] proved with their work that lattice distortion in stripe ordered cuprates, is just a secondary effect due to the presence of charge order as a modulation of the electronic density located at a precise energy level. In other words, the fact that the scattered intensity varies abruptly with the energy of the incoming beam means that the origin of the peak in the reciprocal space is not given by a lattice modulation (whose intensity would be constant with the photon energy) but from the modulation of the occupation of a specific orbital (see paragraph 1.2.2.5). So, the displacement from the initial lattice positions of the atoms is just a side effect and cannot explain the RIXS intensity as pointed out also by theoretical calculations of Achkar et al. [40].

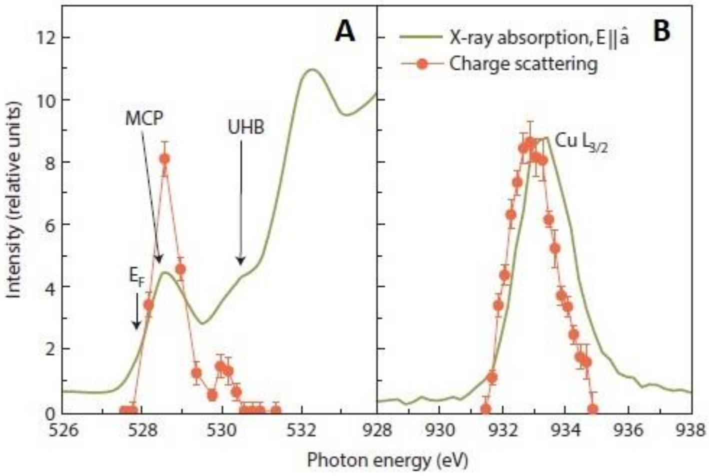

Figure 3.1: resonant soft x-ray scattering from the O-K (A) and Cu-L_3 (B) absorption edges of the stripe ordered cuprate $La_{1.875}Ba_{0.125}CuO_4$ at Q=(0.25,0,1.5). (A)-(B): the solid green line represents the x-ray absorption while the orange experimental points represent the intensity of the signal from charge scattering upon detuning the incoming beam at different energies. As it is possible to see charge scattering closely follows the absorption features of the O-K and of the Cu-L_3 edges. Figure readapted from Ref. [39].

From this example, we can see the importance that the resonant interaction has in RIXS: it provides elemental, chemical, site and orbital selectivity [10]. In fact, if the shift in energy among different absorption edges is larger than the experimental energy resolution, it is possible to differentiate among the different atomic species from which the signal arises, from different orbitals or different chemical environments causing a given energy shift. We can thus pinpoint every particular excitation to the specific element from which it arises as highlighted in paragraph 1.2.3.1, for the charge order in CuO_2 planes.

Being a *photon in – photon out* spectroscopy, RIXS guarantees the neutrality of the sample. No charging effects are perturbing the system during the measurements. This is particularly important for the case of cuprates, given the fact that undoped parent compounds are insulating strongly correlated systems and therefore there is no way for the charge to leave the sample without perturbing it.

Moreover, RIXS is a bulk sensitive probe since it is not affected too much by the conditions of the surface of the sample. In fact, the contamination of the surface, its roughness and surface effects do not constitute a main threat to the experimental results due to the relatively long distance that photons can travel inside the sample. The attenuation path of x-rays inside the material is far larger than that of electrons, ranging from tens of nm to several μm for normal incidence onto the sample, in the energy interval comprised between 100 eV and 10 KeV [8]. On the other hand, RIXS can be used to probe surfaces, by playing with the experimental geometry (for instance in grazing incidence the attenuation length is reduced by a factor of ten ensuring that the signal comes from shallower regions of the sample). It can also access buried interfaces and dislocation [10], [8]. For instance, it has been shown that it is possible to study thin films one or two unitary cells thick [35]. Although RIXS is a bulk sensitive probe, it does not require large amounts of material to yield an acceptable signal. Compared to neutrons, x-rays have much bigger cross-sections for the interaction with matter, so they do not need huge single crystalline samples (which are often a real issue when we are dealing with cuprates). The ratio between the count rate normalized to the sample volume of RIXS and of INS (inelastic neutron scattering) is of order on 10^{11} [8].

Finally, RIXS possess also momentum resolution. The momentum carried by soft by x-ray is not negligible, so we can probe regions of the reciprocal space which do not necessarily coincide with its origin. Thus, we can generate dispersion maps in a sizable portion of the momentum space following the momentum transfer from the photons to the sample.

Overall, resonant-IXS is a very flexible and powerful technique. But it presents some intrinsic disadvantages that are summarized here: limited access to the reciprocal space, incompatibility with crystal based energy or polarization analyzers (that are successfully employed in the hard x-rays regime) and the need for high vacuum. In fact, the minimum measurable periodicity in the real space is limited to 3 Å for an energy of the incoming photons equal to 2 KeV. This implies a consequent reduction of the portion of the reciprocal space accessible for all the photons with lower energies. In this case RIXS and INS can be regarded as complementary techniques, since neutrons allow bigger momentum transfer but are restricted around the (π,π) region of the reciprocal space. The incompatibility with crystal analyzers and the need for high vacuum, are major problems that spurred the fantasy of scientists and researchers throughout the world: in the next section, we will briefly present on instrument conceived to face these hurdles and which achieved best-in-class level of performances. These problems are particularly painful given the huge importance of the experimental geometry (see next section) in RIXS: in fact, the reliability of the measurement of momentum and energy is related to the precision with which we can control the position and the angles of the sample.

3.1.2 Scattering Process

By hitting the sample, the incoming beam could leave the system in an excited state from which different kinds of elementary excitations can be studied by properly analyzing the energy, momentum and polarization of the outcoming beam. In fact, the interaction with matter could change the parameters of the incoming photon: physical conservation rules impose that the difference in energy, momentum or polarization is taken by the system, therefore possibly leaving it in a final state different from the initial state. If we assume that the system initially is in its ground state, we can impose for the energy and momentum conservation the following equations:

$$\hbar\omega_i = \hbar\omega_o + E^{exc} \tag{3.1}$$

$$\hbar\boldsymbol{k}_i = \hbar\boldsymbol{k}_o + \hbar\boldsymbol{q}^{exc} \tag{3.2}$$

where the subscript "i" and "o" respectively represent the incoming and outcoming photon. "exc" indicates the excited state in which the system is left. Equation (3.1) ensures the energy is conserved through the scattering process, while (3.2) states momentum conservation before and after scattering happens. The angular momentum involving the polarization of the photon is also conserved. By properly changing the experimental geometry (which determines the relative directions of $\mathbf{k}_i$ and $\mathbf{k}_o$) it is possible to vary the amount of transferred momentum $\mathbf{q}^{exc}$ to the sample and so, to create a map of the scattered intensity versus the transferred momentum. If we consider also the energy transferred to the system, it is possible to find out the dispersion relations (momentum-energy maps) of different excitations of the material. In fact, by knowing the energy of the incoming beam and by carefully measuring the energy of the outgoing radiation, it is possible to assess the energy lost (or gained, in anti-stokes events) during the inelastic scattering process. The parameters of the incoming photons are well known, especially with the new generation synchrotron sources: energy monochromators ensure that the energy is tuned on the desired absorption edge, polarization control is ensured by the synchrotron source and momentum control comes from a well collimated beam with a spot size (4×60 μm^2) well above the diffraction limit (ensuring a well-defined value for the momentum).

Following reference [8], RIXS can be described as an energy loss spectroscopy (due to the inelastic scattering) in which three different states of the system are involved: the initial, the intermediate and the final state. Therefore, the excitation of the system is a two steps process since in between the initial and final state the system passes through an intermediate state (see Figure 3.2). The function of the intermediate state is essential because it allows momentum conservation. In fact, we could wonder how from a process based on the resonant absorption of a photon by a single localized atom, we can retrieve the momentum information. The answer relies on a pure quantum-mechanical effect: since we do not observe the intermediate state where the atomic localized absorption happens, the momentum is conserved because we do not pinpoint the precise atom absorbing the photon. This process is based on a quantum mechanical interference effect (G. Ghiringhelli, J. van der Brink, [10] and [41]).

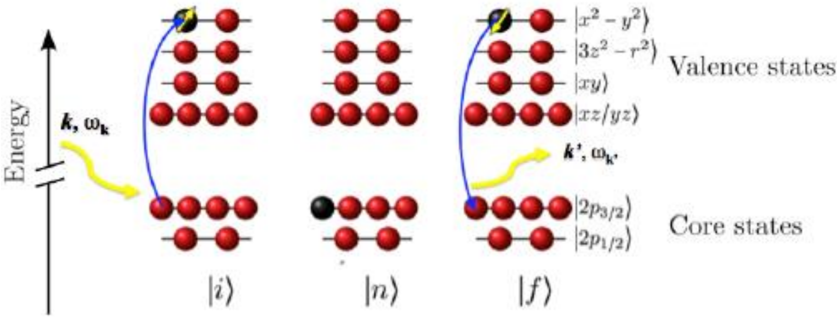

Figure 3.2: Schematic representation of the absorption by a Cu-3d^9 atom of a resonant photon at the L_3 edge (931 eV). Red spheres represent filled electronic states, yellow arrows represent the incoming (left) and outgoing (right) photons. From left to right the initial $|i\rangle$, intermediate $|n\rangle$ and final state $|f\rangle$ are represented. The figure schematizes the creation of a spin excitation with energy $\hbar\omega_{\boldsymbol{k}} - \hbar\omega_{\boldsymbol{k'}}$ and momentum $\hbar\boldsymbol{k} - \hbar\boldsymbol{k}'$. Figure reproduced from Ref. [42]

Figure 3.2 depicts a RIXS process for the Cu-L_3 absorption edge, where a magnetic excitation is created: the only hole left in the 3d valence states of copper is filled by an electron excited from a $2p_{3/2}$ core level state. The strong spin-orbit coupling of the core hole in the intermediate state bridges the transfer of angular momentum from the incoming photon to the shallow 3d hole left in the valence states. This spin flip process, which follows the third conservation rule regarding the total angular momentum (spin and orbital), allows the study of magnetic excitations in the material, with their energy and momentum dependence [43]. From the intermediate state, which is very unstable having a very short lifetime of about 1 fs, the system relaxes to the final state. However, the final state does not necessarily coincide with the initial ground state (which instead is the case for elastic scattering), but can possibly contain some low energy excitations which can be thus studied by analyzing the properties of the outcoming photon (as showed in Figure 3.2). The extremely short lifetime of the excitation allows the study of fast phenomena happening on very short timescales. For example, concentrating on the case of charge order, RIXS is able to sense CDWs at much higher temperatures than slower techniques (for instance NMR), since it does not average out fluctuating or dynamical signals slower than 1 fs.

From Equation (3.1), we see that RIXS gives the possibility to study both inelastic and elastic excitations. In fact, if the energy of the incoming and of the outgoing beam are equal, no energy is transferred to the sample and so a static component of charge or magnetic arrangement is probed. On the other side, if E^{exc} is different from zero an inelastic feature in the energy momentum map is achieved, associated with a dynamical process or a low energy excitation [10]. To be precise, in RIXS energy resolved maps we cannot be completely sure a peak is elastic, due to the finite energy resolution. Therefore, it is better to speak of quasi-elastic features for peaks in the zero energy-loss range, when the resolution and the noise in the spectra do not allow to quantify a finite reliable value for the energy loss. Thus, the quasi-elastic peak is related to excitations that are static within the characteristic time of the probing mechanism imposed by the instrumental energy resolution: $\tau \sim \hbar/\delta E$ (where δE represents the energy resolution). Actually, since we have some knowledge of the instrumental response function we can go below the limit imposed by the resolution and push our limits for the distinction quasi-elastic-inelastic features a little bit further (see for example Peng et al. [26] declaring an upper limit for the energy of quasi-elastic peak equal to 10 meV, even though the best resolution of the instrumentation is 35 meV). This highlights the importance of a good energy resolution whose main contribution is represented by the spectrometer: in the soft energy range, as mentioned above, we cannot use Bragg optics which can provide a resolution as low as 1 meV for hard x-rays, and so we are tied to a minimum of 35-30 meV [10].

While during a RIXS experiment we can distinguish the energy of different excitations, in RXS (resonant x-ray scattering) we give up this possibility and we achieve a momentum map of the energy-integrated scattered intensity. Actually, if we have weakly dispersing inelastic features, RIXS and RXS signal can provide the same momentum evolution for the ordering phenomenon measured (see for instance reference [5]). Actually, as said in chapter 2 and as we will better clarify in the following, the energy resolution is essential for weak signals since it allows to extract as much information as possible from the energy region we are interested in, out of the background represented by the usually much stronger features at different energies. Furthermore, energy resolution is fundamental to measure lattice and magnetic dispersion relations where (conversely to charge order) the energy of the excitation varies throughout the momentum space, possibly yielding strange and interesting physical insights (see for instance [44] or [45]).

3.1.3 Accessible Excitations

As already mentioned RIXS can yield information about lattice, charge, orbital and magnetic excitations. The variety of working modes, accessible states and its flexibility, make it the most used technique in the field of high-Tc superconductors. We will now concentrate on the possible excitations that can be triggered at the Cu-L_3 absorption edge by the resonant process and which can be divided in terms of the energy, momentum and polarization behavior of the outcoming photon associated.

From the energy point of view, it is possible to distinguish between Raman and fluorescence excitations. Upon slight changes of the energy of the incoming beam they behave in two different ways: Raman features are found at a constant energy loss, while fluorescence features present a constant energy of the outcoming photon, independent on the energy of the incoming photons. Raman features present two possible behaviors in the momentum space, due to the different nature of the modes probed: collective modes show a clear dispersion in the reciprocal space, meaning that the intensity of the scattered light varies as the value of the in-plane momentum transferred changes. Examples of this behavior are charge density waves, magnons and phonons. On the other hand, localized excitations, such as the ligand field (dd) peak (see Figure 3.3) associated to intra-band energy transfer, are not dispersing with different values of $\mathbf{q}^{\mathbf{exc}}$. In Figure 3.3, at a bigger energy loss than the dd excitations, there are charge transfer excitations, related to the transfer of charge between a copper atom and a ligand oxygen atom inside the same unitary cell. They present a mixed character since the electron involved moves inside the unitary cell, even though this movement does not manifest in a true dispersion in the reciprocal space. The analysis of the polarization of the scattered photons gives important clues about the origin of the elementary excitation causing the scattering event. There are two distinct channels for the polarization of the outcoming beam: cross and non-cross. Cross means that the polarization of the beam has been rotated by 90° during the interaction with the sample, from π (i.e. parallel to the scattering plane, see Figure 3.5) to σ (orthogonal to the scattering plane) or vice versa. In the non-cross channel the polarization of the beam does not change. Theoretical models and the calculated cross-sections for different experimental parameters, allow to determine the best configuration to probe different kinds of excitations. For instance, the σ incident polarization is more suitable to detect charge order, while π polarization is more sensitive to magnetic excitations [8]. The result is that it is of paramount importance the possibility to analyze the polarization also in the soft x-ray regime: this is actually feasible thanks to an instrument called *polarimeter* which will be briefly presented later.

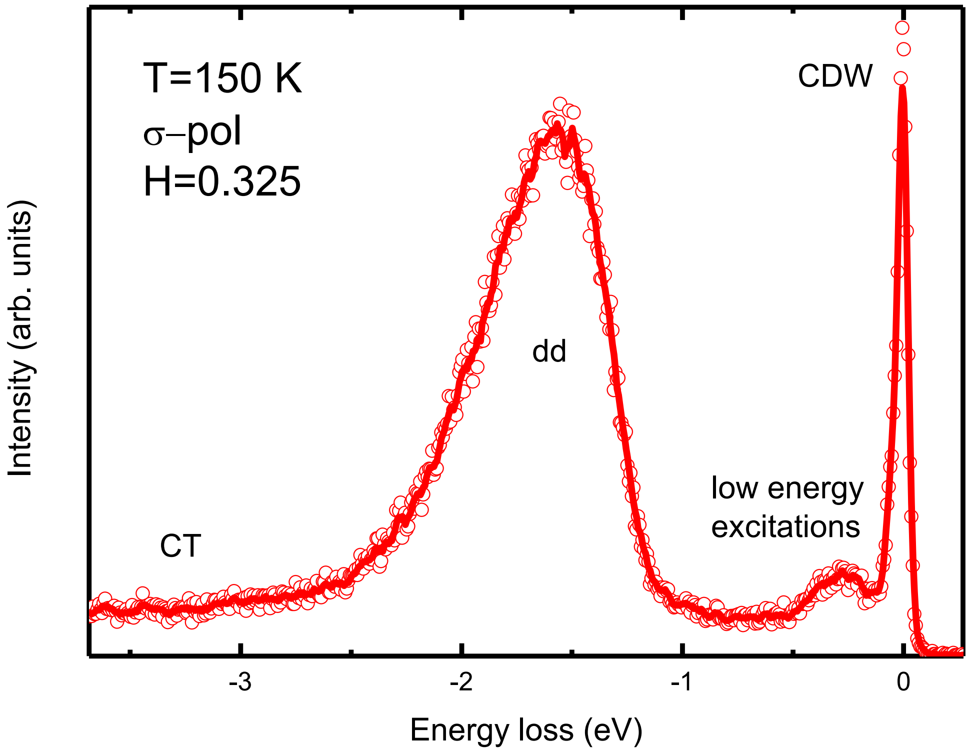

Figure 3.3: Soft resonant x-ray scattering from underdoped NBCO (T_c=60K). The spectrum has been acquired at 150 K with σ incident polarization and at a value for the transferred momentum $\boldsymbol{q}_{\parallel}$ = (0.325,0). Hollow points represent the raw data while the red solid line is the result of five points smoothing. Near each feature, it is possible to see the excitation associated.

Figure 3.3 shows the energy dependence of the scattered intensity at the point $\boldsymbol{q}_{\parallel}$ = (0.325,0) in the bidimensional reciprocal space, for an underdoped sample of NBCO. We can now better explain Figure 1.7 which represents in cascade different spectra, analogous to the one reported above, for different values of the transferred momentum. Each spectral feature is labelled with the name of the excitation associated to it. Here we can see a strong peak associated to charge order even at a quite high temperature as 150 K, denoting both the strength of the phenomenon in NBCO and the good experimental sensitivity.

The biggest part of the spectral weight is associated to dd excitations, which come from the splitting of the 3d levels due to the ligand field caused by the repulsion between 3d orbital of copper and 2p orbitals of oxygen. In fact, the different shape and elongation in space of the 3d orbitals determine different amounts of spatial overlap for their electronic density with the states of oxygen. Therefore, the 3d states split due to the distinct Coulombic repulsion each orbital feels with the adjacent oxygen atoms. One interesting comment regarding dd excitations, highlights the relevance of the intermediate state in RIXS. In fact, intra-band transitions are forbidden by dipole conservation rule (Δl=0 in this case). The intermediate state gives the possibility to probe such a transition dividing the path in two dipole allowed excitations: from the 2p core level to the 3d empty state and then down from a another 3d state with different energy to the same 2p core hole. The energy transfer is different from zero (1.5-2 eV, see Figure 3.3) and so the initial state is different from the final state. In the low energy loss region, it is possible to see clearly a peak which could be connected to a magnetic mode or to a phonon. Phonons are possibly present in the left shoulder of the sharp quasi-elastic peak too. As will be discussed in the following chapter, the quasi-elastic peak is not symmetric nor resolution limited, indicating the presence of further features at finite energy loss contributing to it. Finally, the quasi-elastic peak represents the maximum of the peak related to charge order in the momentum space. CDWs are not the only input building up this peak, since there is also the effect of the elastically diffused light from the sample. This phenomenon is maximum for specular reflection (i.e. zero momentum transfer) and decreases while moving away from this geometry even though it gives a still sizable contribution to the background elastic signal which has nothing to do with charge order and represents an annoying factor we have to cope with in the analysis of data.

3.1.4 RXS Cross-section and Theory

The following paragraph describes the theory of resonant x-ray scattering mainly following the path outlined in reference [10], but also partially drawing from ref. [43] and [41].

The theory of resonant scattering follows from a time dependent perturbative approach to the effective non-relativistic radiation-matter interaction Hamiltonian (see Equation (3.3)), that can be derived from the full electron-matter minimal coupling Hamiltonian. For a second order process, as the resonant interaction, we look for terms of second order in the vector potential: that is combinations of the kind $a_\nu(\boldsymbol{q})a_\nu^\dagger(\boldsymbol{q}-\boldsymbol{Q})$. Where $a_\nu(\boldsymbol{q})$ [$a_\nu^\dagger(\boldsymbol{q})$] represent the annihilation [creation] operator for a photon with wavevector **q**, polarization state ν and frequency $\omega = c|\boldsymbol{q}|$. In fact, in the second quantization framework the vector potential can be expressed as: $\boldsymbol{A}(\boldsymbol{r},t) \propto \sum_{\boldsymbol{q},\nu} \varepsilon_\nu[\exp(i\boldsymbol{q} * \boldsymbol{r} - i\omega t)\, a_\nu^\dagger(\boldsymbol{q}) + h.c.]$ (where ε_ν represents the polarization vector associated to the state ν). In this paragraph, we slightly change the notation to be fully coherent with the work of Comin and Damascelli [10] and since the following approximations are better expressed in this notation: indeed, the momentum of the incoming photon is written as $\boldsymbol{q}$ while the transferred momentum is indicated as $\boldsymbol{Q}$. We start from the following total Hamiltonian of the interacting system (matter and radiation):

$$\begin{aligned} H_{tot} &= \sum_j \left\{ \tfrac{1}{2m_e}\left[\mathbf{p}_j - \tfrac{e}{c}\mathbf{A}(\mathbf{r}_j,t)\right]^2 + V(\mathbf{r}_j,t) \right\} + \sum_{j\neq k} \tfrac{e^2}{|\mathbf{r}_j-\mathbf{r}_k|^2} + H_{\mathrm{EM}} \\ &= \underbrace{H_{\mathrm{el}} + H_{\mathrm{EM}}}_{H_0} + \underbrace{\frac{e}{m_e c}\sum_j \mathbf{A}(\mathbf{r}_j,t)\cdot\mathbf{p}_j}_{H_{\mathrm{int}}^{\mathrm{lin}}} + \underbrace{\frac{e^2}{2m_e c^2}\sum_j \mathbf{A}^2(\mathbf{r}_j,t)}_{H_{\mathrm{int}}^{\mathrm{quad}}} \end{aligned} \tag{3.3}$$

e and m are the electronic charge and mass, $\boldsymbol{p}_j$ and $\boldsymbol{r}_j$ are the momentum and the position of the j-th electron, $V(\boldsymbol{r},t)$ is the lattice potential and $e^2/(\boldsymbol{r}_j - \boldsymbol{r}_k)$ is the Coulomb interaction between two different electrons. The Hamiltonian of the electromagnetic field alone is $H_{EM} = \sum_{\boldsymbol{q},\nu} \hbar\omega[\, a_\nu^\dagger(\boldsymbol{q})a_\nu(\boldsymbol{q}) + 1/2]$ and the term related to the electronic energy in the second equality is $H_{el} = \sum_j {}^{1}\!/_{2m_e}\, \boldsymbol{p}_j^2 + \sum_j V\big(\boldsymbol{r}_j, t\big) +$

$\sum_{j\neq k} {e^2}/{|\boldsymbol{r}_j - \boldsymbol{r}_k|^2}$. Highlighted in the second equality of Equation (3.3) you can see the linear and quadratic terms in the vector potential representing the interaction radiation-matter. We now introduce a suitable basis set created starting from the eigenfunctions of the unperturbed part of the Hamiltonian H_0: $|\Psi_M\rangle = |\psi_m\rangle_{el} * |\phi_{n_{q,\nu}}\rangle_{EM}$ where $|\psi_m\rangle_{el}$ represents the eigenfunction of the unperturbed electronic part having eigenvalue ϵ_m and a set of quantum numbers identified by m, while $|\phi_{n_{q,\nu}}\rangle_{EM}$ indicates the eigenstate of the unperturbed electric field identified by the set of occupation numbers $\bar{n}_{\boldsymbol{q},\nu} = \{n_{\boldsymbol{q1},\nu 1}, n_{\boldsymbol{q2},\nu 2}, \ldots\}$ expressing the number of photons in each different state characterized by a definite value of the momentum and of the polarization. The label $M = \{m, \boldsymbol{q}, \nu\}$ of the total wavefunction indicates the global set of quantum numbers associated to it. We can also introduce the energy relative to each element of this set of functions as $E_M = \epsilon_m + \sum_{\boldsymbol{q},\nu}(n_{\boldsymbol{q},\nu} + \frac{1}{2})\hbar\omega_{\boldsymbol{q}}$. Since the overall Hamiltonian includes also a perturbation, this basis set does not coincide with the eigenfunctions of the system. In any case, it is useful to describe the scattering event, in which one photon with a definite momentum is annihilated and correspondingly a new photon with a different wavevector and polarization is created, therefore involving a change between the initial and the final states. The following step is to calculate the transition probability between these two states. To do so we use the generalized Fermi's golden rule [46] with the further assumption that the electronic part of the initial $|\Psi_i\rangle = |\psi_{GS}\rangle_{el} * |\phi_i\rangle_{EM}$ and of the final $|\Psi_f\rangle = |\psi_{GS}\rangle_{el} * |\phi_f\rangle_{EM}$ states involved are equal an coinciding with the electronic ground state of the system (elastic scattering, as it is the case for charge order with the present resolution):

$$w_{i\to f} = 2\pi |\langle \Psi_i | T | \Psi_f \rangle|^2 \delta\left(E_f - E_i\right) \tag{3.4}$$

With the T-matrix is equal to:

$$T = H_{\mathrm{int}} + H_{\mathrm{int}} \frac{1}{E_i - H_0 + i\eta} H_{\mathrm{int}} + H_{\mathrm{int}} \frac{1}{E_i - H_0 + i\eta} H_{\mathrm{int}} \frac{1}{E_i - H_0 + i\eta} H_{\mathrm{int}} + \ldots \tag{3.5}$$

The second term of Equation (3.5) represents the various orders of the interaction. Since we need a matrix element inside the expression of $w_{i\to f}$ of second order in the vector potential (to achieve terms proportional to $a_\nu(\boldsymbol{q})a_\nu^\dagger(\boldsymbol{q} - \boldsymbol{Q})$) we keep just the first and the second order terms of T. Therefore, the linear part of T in the interaction Hamiltonian yields a term describing the scattering from the quadratic part of the interaction (H_{int}^{quad} in Equation (3.3)), while in the quadratic part of T we keep just H_{int}^{lin} which is linear in $\boldsymbol{A}(\boldsymbol{r}, t)$. Thus, we get two terms for the perturbative transition probability:

$$w_{i\to f}^{(1)} = 2\pi \left| \frac{e^2}{2m_e c^2} \langle \Psi_i | \sum\nolimits_j \mathbf{A}^2(\mathbf{r}_j, t) | \Psi_f \rangle \right|^2 \tag{3.6}$$

$$w^{(2)}_{i\to f} = 2\pi\left|\left(\frac{e}{m_e c}\right)^2 \sum\nolimits_M \frac{\langle\Psi_i|\sum_j \mathbf{A}(\mathbf{r}_j,t)\cdot\mathbf{p}_j|\Psi_M\rangle\langle\Psi_M|\sum_k \mathbf{A}(\mathbf{r}_k,t)\cdot\mathbf{p}_k|\Psi_f\rangle}{E_i - E_M + i\Gamma_M}\right|^2 \tag{3.7}$$

The δ-function has been dropped here for convenience, after ensuring the conservation of energy during the scattering process imposing $E_i = E_f$ (for the particular case of elastic scattering). As it is possible to see, the matrix element in Equation (3.7) presents the sum over the infinite number of intermediate (excited) states defined by the set of functions Ψ_M. This summation running over all the possible virtual intermediate states M, which are not directly observed in a RIXS experiment, allows interference effects among different states to take place [41]. After expanding the square of the vector potential assuming an elastic scattering process involving only a single photon, noting that $a_\nu^\dagger(\boldsymbol{q}_{out})a_\nu(\boldsymbol{q}_{in})|\phi_i\rangle_{EM} \propto |\phi_f\rangle_{EM}$ and that $E_i = \epsilon_{GS} + (n_{\boldsymbol{q}_{in}} + \frac{1}{2})\hbar\omega_{\boldsymbol{q}_{in}}$, $E_M = \epsilon_m + (n_{\boldsymbol{q}_{in}} - 1 + \frac{1}{2})\hbar\omega_{\boldsymbol{q}_{in}}$, we can rewrite Equations (3.6) and (3.7) as:

$$w^{(1)}_{i\to f} \propto \left|\langle\psi_{\mathrm{GS}}|\sum\nolimits_j e^{-i\mathbf{Q}\cdot\mathbf{r}_j}|\psi_{\mathrm{GS}}\rangle\right|^2 \propto |\langle\psi_{\mathrm{GS}}|\,\rho(\mathbf{Q})\,|\psi_{\mathrm{GS}}\rangle|^2 \tag{3.8}$$

$$w^{(2)}_{i\to f} \propto \left|\sum_m \sum_{j,k} \frac{\langle\psi_{\mathrm{GS}}|\varepsilon_{\nu_{\mathrm{in}}}\cdot\mathbf{p}_j\cdot e^{i\mathbf{q}_{\mathrm{in}}\cdot\mathbf{r}_j}|\psi_m\rangle\langle\psi_m|\varepsilon_{\nu_{\mathrm{out}}}\cdot\mathbf{p}_k\cdot e^{-i\mathbf{q}_{\mathrm{out}}\cdot\mathbf{r}_k}|\psi_{\mathrm{GS}}\rangle}{\epsilon_{\mathrm{GS}} - \epsilon_m + \hbar\omega + i\Gamma_m}\right|^2 \tag{3.9}$$

Where $Q = \boldsymbol{q}_{in} - \boldsymbol{q}_{out}$ is the moment transferred by the electromagnetic field to the sample and $\rho(\boldsymbol{Q})$ in Equation (3.8) is the Fourier transform of the electron density operator $\rho(\boldsymbol{r}) = \sum_j \delta(\boldsymbol{r} - \boldsymbol{r}_j)$. Equation (3.9) involves the scattering of a photon in a two-step process: first a core hole is created by the absorption of the incoming photon, then the system relaxes from this intermediate state to the ground state again (following the assumptions made) re-emitting a photon in a different direction. This second equation describes the RIXS resonant scattering process. The first order transition probability (Equation (3.8) is instead a first order instantaneous process which does not involve any intermediate state: it the describes an elastic non-resonant scattering process as that happening in x-ray diffraction (XRD). As it is possible to see by looking at the two equations written above, the non-resonant event is proportional to the squared modulus of the total Fourier transformed electronic density in the ground state, and therefore, in the case of copper (Z=29), the weight of the scattering is mainly given by the greater number of localized core electrons, rather than by the valence electrons where low energy interesting excitations take place. This is the reason why XRD can probe lattice positions and excitations causing a distortion of the lattice structure. Equation (3.9) can be further simplified by considering the fact that the x-ray excitation is local, thus giving the possibility to exploit the orbital-atomic character of the electronic states of the system. So: (i) as new basis we can use the local orbitals of each particular lattice site n: $\psi_m(\boldsymbol{r}) \to \chi_l^{(n)}(\boldsymbol{r}) = \chi_l(\boldsymbol{r} - \boldsymbol{R}_n)$; (ii) the local character of the new basis implies that all the matrix elements vanish for orbitals belonging to different lattice sites: $\left\langle\chi_i^{(m)}\middle|\boldsymbol{p}\middle|\chi_l^{(n)}\right\rangle \propto \delta_{m,n}$; (iii) finally the initial core electron is localized in a region smaller than the soft x-ray wavelength so the phase of the radiation throughout the region where the electronic density is non-zero is approximately fixed: $e^{i\boldsymbol{q}\cdot\boldsymbol{r}} \sim e^{i\boldsymbol{q}\cdot\boldsymbol{R}_n}$. We introduce now the tensor called *form factor* f_{pq}:

$$f_{pq}^{(n)}(\hbar\omega) = \frac{e^2}{m^2c^2} \sum\nolimits_{i,l} \frac{\langle \chi_i^{(n)} | \mathrm{P}_q | \chi_l^{(n)} \rangle \cdot \langle \chi_l^{(n)} | \mathrm{P}_p | \chi_i^{(n)} \rangle}{\hbar\omega - (\epsilon_l^{(n)} - \epsilon_i^{(n)}) + i\Gamma_{il}} \tag{3.10}$$

This quantity depends on the photon energy and on each particular atomic site. In fact, we can recognize the atomic functions recalled above (with their eigenvalues $\epsilon_i^{(n)}$ and $\epsilon_l^{(n)}$, respectively for the initial and intermediate states) defined over the same lattice position $\boldsymbol{R}_n$ and the energy of the photon at the denominator. Γ_{il} is the inverse lifetime ($\hbar/\tau_{il}$) of the intermediate state, which is quite unstable presenting a high-energy core hole, equal to the energy broadening of the transition. Exploiting the form factor it is possible to rewrite the scattered intensity during a RIXS process as:

$$\begin{aligned} I^{\mathrm{RXS}}(\mathbf{Q}, \hbar\omega) &\propto \left| \sum\nolimits_{pq} (\varepsilon_{\nu_{\mathrm{in}}})_p \cdot \left[\sum\nolimits_n f_{pq}^{(n)}(\hbar\omega)\, e^{i\mathbf{Q}\cdot\mathbf{R}_n} \right] \cdot (\varepsilon_{\nu_{\mathrm{out}}})_q \right|^2 \\ &= \left| \sum\nolimits_{pq} (\varepsilon_{\nu_{\mathrm{in}}})_p \cdot F_{pq}(\hbar\omega) \cdot (\varepsilon_{\nu_{\mathrm{out}}})_q \right|^2 . \end{aligned} \tag{3.11}$$

The term F_{pq} is the scattering tensor defined by the second equality of Equation (3.11). It is not a local quantity (since we have the summation over different lattice vectors) and its projections along the polarization vectors of the incoming and outcoming photons are related to the physical observable during a RXS experiment (in fact, the scattered intensity I^{RXS} is defined over momentum and energy space) and select the symmetry of the state observed [27]. While the intensity of the first order process is fairly constant with the energy of the incoming photon, the two steps process describing RIXS involves a resonant enhancement, with a strong peak at given photon energies (usually near absorption edges) and a decaying behavior to zero out of resonance. Thanks to this peaked shape of the scattered intensity, RIXS gains a strong sensitivity for electronic modulations at the given absorption edge involving a precise band while XRD is sensitive to the total electronic density. As already said the enhancement can be as high as a factor of 82 in cuprates [39], [38].

We go on discussing further the physical implications of the formulas derived. As we can notice from Equation (3.10) the formulation of the form factor is responsible for the resonant enhancement of the scattered intensity at given photon energies: in fact, the denominator can be minimized for $\hbar\omega$ equal to the energy difference between the two eigenvalues of the intermediate and initial atomic states (i.e. at resonance). Note that the finite lifetime of the intermediate state avoids the divergence of the denominator thanks to the imaginary unit multiplying it. Remember also that the transition respects the energy conservation principle via the δ-function we exploited at a certain point. In a more complete version of the RIXS cross-section, taking into account also finite energy loss from the sample, the conservation of energy is always enforced (see for instance references [8] and [43]) and thus, any spectral feature associated to a certain transition is found at the same energy loss amount. From Equation (3.11) we can also see that the resonant process introduces the sensitivity to the polarization states of light, allowing the study of the local symmetry of the excitations (see for instance [27]). As said before, the two-step process involves the sum over *all* the possible intermediate states, since differently from the final state which is observed and thus well-defined, they are not. In the case of Cu atoms in the $3d^9$ oxidation state and with the assumption that the only atomic orbitals in the same lattice site are contributing to the signal, the intermediate state is only one, since there is only one available hole in the valence states. This represents a strong simplification in the calculations. It has to be said though, that this single ion model is valid for insulating parent compounds only, whereas for doped samples more complicated models are required [47]. Finally, even if the resonant behavior strongly amplifies the signal from the scattering, the small second order matrix elements cause the signal from RIXS and RXS to be very weak. For this reason, we need sources with high brilliance and extremely sensitive instrumentation, such that described in the next section.

3.2 ID32: The State-of-Art of Instrumentation

ID32 is the only beamline at the European Synchrotron Radiation Facility (ESRF) working in the soft x-ray regime [8]. Moreover, at the present moment it possesses the best performances in terms of energy resolution, thanks to the recently inaugurated European-RIXS (ERIXS) spectrometer. In the following paragraphs, we will briefly describe the synchrotron source, the scattering geometry (allowing to transfer different amounts of momentum to the sample) and finally the specific properties of the ID32 beamline and of the ERIXS spectrometer.

3.2.1 Synchrotron light source: ESRF

As stated in the former section RIXS is a very photon-hungry technique, due to its intrinsically small cross-sections. Therefore, to achieve a sizable signal from the excitations probed it is necessary to use a source providing a high photon flux in a well collimated beam. This is the reason why conventional x-ray sources are not suitable and synchrotron light is needed. In fact, the properties of this peculiar kind of light, generated as a consequence of a relativistic process, are: high brilliance, high monochromaticity (narrow spectral range), high photon flux and a naturally defined polarization [48].

The production of radiation by a synchrotron, hinges upon the physical principle that an accelerated charged particle emits radiation. When a charge travels at relativistic speed, the light created possesses the specific properties needed by the experimental research (such has high brilliance) [49]. Thus, to produce the x-rays required for instance in RIXS, the charged particles travel in bunches inside a ring, where the collisions with other particles are minimized by ultra-high vacuum (UHV) conditions. The UHV allows the stability of the beam of charges for many hours inside the ring. These particles are accelerated by electromagnets, both to continue their curved trajectory and to provide the radiation at the desired energy. The result is highly collimated, intense and monochromatic light in the continuous energy range from 1 eV to 100 KeV [50].

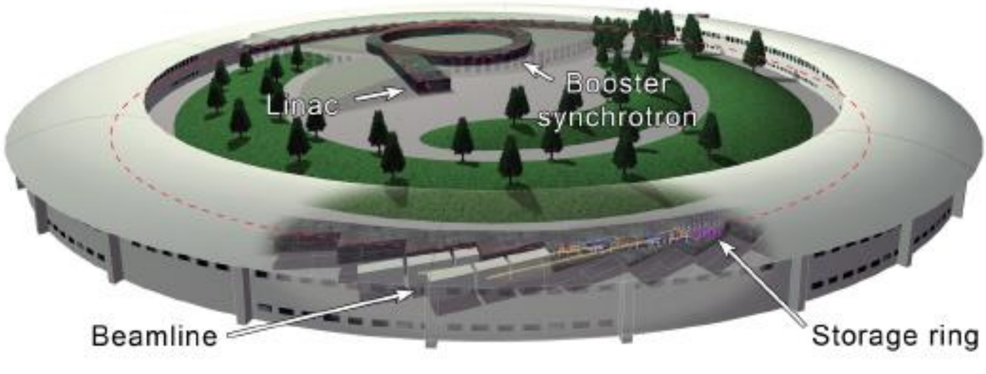

Figure 3.4: ESRF simple scheme. It is possible to notice the main components typical of a third-generation synchrotron: the linear accelerator (*linac*), the booster ring and the storage ring from which the light parts to reach the different beamlines. Figure reproduced from Ref. [50]

Referring to Figure 3.4 we now describe the specific properties of ESRF. This facility belongs to the category of third generation synchrotron light sources and it employs electrons for light generation. The life of the electrons providing x-rays starts when they are generated by an electron gun. Then they are grouped in separated bunches and accelerated to 200 MeV in the linear accelerator (*linac,* see Figure 3.4). It is worth to notice that the rest mass of the electron is 511 KeV and thus even in this first acceleration stage they already reach relativistic velocities. The linac is connected with a "small" ring called booster synchrotron, having a 300 m circumference, where the charged particles are accelerated by electric fields to 6 GeV. When the electrons reach the final energy desired inside the booster, they are injected in the storage ring which possesses a circumference 844 m long. The values that the current can reach are about 200 mA. The vacuum level in the storage ring is as high as 10^{-9} mbar, allowing charges to travel inside of it for 23 hours no stop. Along the path of the ring there are several magnets producing the light for the different beamlines. A beamline is the physical place where light coming from the storage ring, is brought to the sample under controlled conditions, to perform specific experiments. As a whole, the ring at ESRF is made by 32 straight and 32 curved sections alternated [48]: curved sections contain two large bending magnets that apply a magnetic field orthogonal to the plane of the ring to keep charges inside the circular trajectory via the Lorentz force. Straight sections instead are endowed with focusing magnets, avoiding the divergence of the beam. The beam of x-rays is produced by the *undulators*, placed in the straight sections. Undulators are composed by an array of small magnets forcing the electrons to a wavy trajectory. The acceleration that is thus enforced to the particles travelling inside these magnetic components, causes the emission of light with an energy proportional to the magnitude of the acceleration undergone. The direction of the polarization of the outcoming radiation is defined by the particular characteristics of synchrotron light and it is linear. The energy can be tuned by varying the distance between the small magnets composing the undulator. As it will be possible to appreciate in the next paragraph where the experimental layout is discussed, the characteristics of the synchrotron source are essential for the RIXS experiment. In fact, if we want to measure the amount of energy and momentum (both linear and angular) transferred during the scattering process to the sample, it is not only necessary to measure precisely the properties of the outcoming photon, but also the characteristics of the incoming beam must be under strict control. In particular, the collimation of the beam impinging onto the sample ensures that the momentum of the incoming photons is well known, the high monochromaticity of the beam (plus further monochromators along the beamline) allows energy control and the native well defined state of the polarization is used as a reference to measure the outcoming polarization by means of the *polarimeter* (see paragraph 3.2.4.1).

3.2.2 Scattering Geometry

In the following paragraph, we outline the experimental geometry employed to transfer a specific momentum vector to the sample. We follow reference [51], for the name and for the definition of the angles and vectors involved. Here we focus on the component of the total momentum transferred $(\boldsymbol{Q})$ parallel to the cuprate planes (ab planes of Figure 3.5.A), called $\boldsymbol{Q}_{\parallel}$, owing to the 2D character of the interesting physics happening in cuprate CuO_2 planes. This is the reason why we limit our discussion to a bidimensional Brillouin Zone (see Figure 3.5.C).

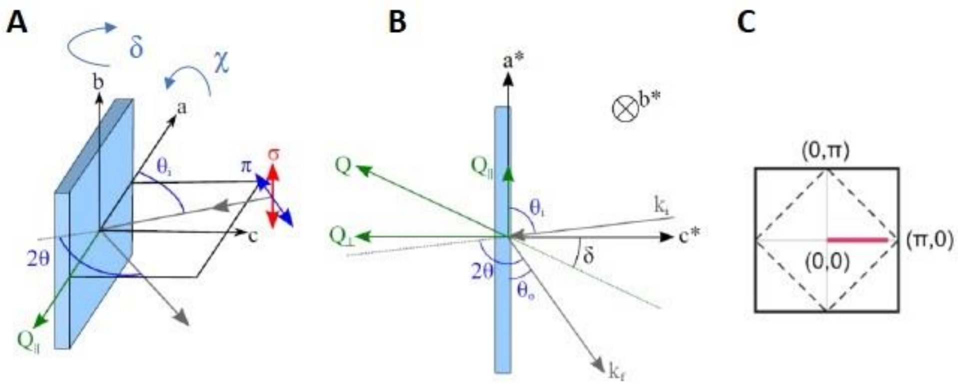

Figure 3.5: Scattering geometry. From left to right: (A) real space representation of the scattering geometry (with the reference axes denoted as a, b and c). The scattering plane is identified as the plane containing the two grey arrows ($\boldsymbol{k}_i$ and $\boldsymbol{k}_f$); (B) reciprocal space: lateral view (from b* direction) of the momentum vectors involved. The reference frame is indicated by axes a*, b* and c*. (C) 2D First Brillouin zone of a cuprate plane, with also the antiferromagnetic Brillouin zone denoted by the dashed lines. If we change δ (showed in (B)) we can move in the reciprocal space along the purple line. Figure readapted from Ref. [8].

Referring to Figure 3.5 we can now discuss the parameters determining the experimental geometry: (A) represents the real space with a, b and c being an orthogonal basis. The vectors a and b are directed like the Cu-O bonds in the cuprate plane (represented by the blue plane). θ_i is the angle of the incident beam from the cuprate plane, and it is related to δ (given by the rotation around the b axis, as indicated by the blue arrow) by $\delta = \theta_i - 2\theta/2$, where 2θ is the scattering angle which is usually fixed to a well-defined value throughout the whole duration of the experiment (for instance the data discussed in chapter 4 are taken with an angle $2\theta = 149.5°$). The same considerations made for δ, hold for χ which instead varies the value of the momentum transferred along the b* axis and identifies a rotation in the c*-b* plane measured starting from the c* axis with sign defined by the curved arrow in Figure 3.5.A. σ and π represent the directions of the polarization of the incoming photons measured with reference to the scattering plane: respectively orthogonal and parallel. (B) is a sketch of what happens in the momentum space identified by the basis (a*, b*, c*) corresponding to (2π/a, 2π/b, 2π/c). The directions identified by these three vectors coincide with those of the vectors (H, K, L) introduced in a previous chapter. θ_o is the angle of the outcoming photon, $\boldsymbol{k}_i$ and $\boldsymbol{k}_f$ are the wavevectors respectively of the incoming and of the outgoing beam, while $\boldsymbol{Q}$ is the momentum transferred to the sample, with its components orthogonal and parallel to the CuO_2 plane. Finally, (C): the solid line represents the bidimensional Brillouin zone, while the dashed line outlines the magnetic Brillouin zone. If we indicate $\boldsymbol{Q} = (H, K, L)$, we have the following formulas relating the components of $\boldsymbol{Q}_\parallel = (H, K)$ (expressed in reciprocal lattice units) to the various angles defined:

$$|\boldsymbol{Q}| = 2|\boldsymbol{k}_i|\sin(2\theta/2) \tag{3.12}$$

$$H = (|\boldsymbol{Q}|/a^*)\sin(\delta) \tag{3.13}$$

$$K = (|\boldsymbol{Q}|/b^*)\cos(\delta)\sin(\chi) \tag{3.14}$$

It follows from these equations that the maximum momentum which can be given to the sample is constrained by the scattering angle 2θ.

3.2.3 ID32

ID32 is specialized in the soft x-ray regime: it can provide photons in an energy range between 400 and 1600 eV. This energy window is suitable for the study of magnetism and electronic structure in condensed matter since it gives direct access to the K edge of oxygen, to the $L_{3,2}$ edges of transition metals and to the $M_{4,5}$ edges of rare earths.

The different experimental techniques available in this beamline are: X-ray Magnetic Circular Dichroism (XMCD), X-ray Absorption Spectroscopy (XAS), soft X-Ray Diffraction (XRD) and of course soft-RIXS. The beamline is quite long since it measures 120 m, and possess two branches (see Figure 3.6), where the light coming from the storage ring can go: one branch is for RIXS. Here the resolving power reachable is as high as 42,000. The second branch is dedicated to XMCD and to non-conventional experiments and features a lower resolving power of 5,000 and the possibility to adjust the beam size from hundreds of microns to several millimeters.

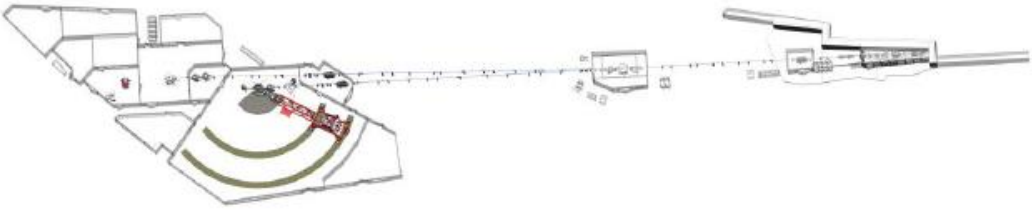

Figure 3.6: top view of the ID32 beamline at ESRF. In red you can see the ERIXS spectrometer which occupies most of the space in the beamline being 11 m long. Figure reproduced from Ref. [52].

Three APPLE II undulators, with the magnets composing them arranged with the same period [53], provide photons with energy in the range defined above with 100% controllable polarization both linear and circular. The beam spot size at the sample holder is $4\times60\ \mu m^2$ (of FWHM) for the RIXS setup. The optical elements employed to bring the light from the storage ring to the experimental stage are machined mirrors operating at grazing incidence.

3.2.4 ERIXS

The subsequent description of the ERIXS spectrometer installed in ID32 beamline follows the lines of reference [8]. ERIXS is the first fully operative new generation soft-RIXS spectrometer. It represents an evolution of the two previous RIXS spectrometers completely designed by the group of Prof. G. Ghiringhelli and Prof. L. Braicovich at Politecnico di Milano: AXES (Advanced X-ray Emission Spectrometer) and SAXES

(Super-AXES). In 2015, the commissioning of ERIXS at ID32 took place to replace AXES at ID08. As a general trend the resolving power increases proportionally to the dimensions of the scattering arm and this reflects on the total dimensions of the different machines: from AXES, which was 2.2 m long with a resolving power $\Delta E/E_0$ of 5,000 at the Cu-L_3 edge, passing through the 5 m long SAXES with a resolving power of 10,000 at the same energy, to ERIXS which is as long as 12 m with a resolving power of 30,000.

The general structure of a RIXS spectrometer encompasses the following stages: source, analyzer and detector. The source for the spectrometer is the beam of light coming from the sample (whose dimension is given by the footprint of the incident beam coming from the storage ring). The first optical element (which coincides with the analyzer) is the concave diffraction grating. It has the function of (i) focusing the scattered radiation on the detector, (ii) spatially dispersing the photons depending on their energy. The latter property of the analyzer gives the energy resolution of the instrument and since the angle of deflection imposed to different incoming energies by the grating cannot exceed a certain value, the longer the scattering arm, the wider the separation among photons with different energies (this is the reason why bigger size of the spectrometer means better resolution). The detector, placed after the analyzer, has the role of capturing each photon while recording its position, which is closely related to its energy. For this reason, the detector is represented by a 2D position sensitive charge coupled device (CCD), meant to absorb the scattered x-rays. The incident beam spot size introduced above (4×60 μm^2) represents the vertical×horizontal dimensions of the beam footprint. The asymmetry on the spot size can now be understood, since the grating disperses the photons as a function of energy along the vertical direction, therefore limiting the maximum dimension of the beam spot size in this direction. The photons collected by the CCD camera are then integrated along the horizontal direction to create a signal (the final spectrum) which depends only on one spatial coordinate, which due to the action of the grating, corresponds to the energy lost by the photons. To be precise the isoenergetic lines do not have exactly the same direction of the rows of pixels of the CCD device. This *slope* aims to avoid the error in the determination of the position of photons impinging on the detector close to the separation line between two rows of pixels.

After what has been said, it can be understood how important is the contribution of the spatial resolution of the detector to the total combined (beamline plus spectrometer) energy resolution of the instrument. Other contributions to the overall energy resolution (which is the most important figure of merit of the spectrometer) are: optical aberrations (coma), the grating shape error and the finite source size. Moreover, we have to take into account the imperfect monochromaticity of the incoming beam (determining the contribution of the beamline to the total uncertainty). The resolution of the detector (which for a commercial CCD camera is 25 μm [54]) is not limited by the pixel size [55] because the *charge cloud*, created by the huge number of electrons excited via Auger cascade process in Si, spreads over an area which is many pixel wide [56]. One possible improvement, achievable without any reconstruction algorithm, is to mount the detector at a certain angle (γ) from the direction of the incoming light, to reduce the effective exit slit, obtaining a distance between the two detected photons on the camera increased by a factor $1/\sin\gamma$. This at the price of a lower effective area of the detector. Better results can be obtained via a centroid algorithm reconstructing with a sub-pixel precision the position of the incoming photon. This algorithm works only for isolated events (single photon counting, SPC) where no charge cloud overlap is present. For the CCD camera in ERIXS this procedure becomes necessary since for this spectrometer the finite CCD resolution is a limiting factor. The final result is 6 μm of spatial resolution, which can be achieved with standard CCD devices.

Everything in the soft x-ray regime is complicated by the need for ultra-high vacuum. In fact, the chamber with the sample holder, the scattering arm and other instrumentation must be kept at a pressure of 10^{-9} mbar. This requirement adds a lot of complications to the design of the system: in particular, two of the toughest challenges are the sample position and orientation control and the cooling system under UHV conditions. Indeed, the cooling system is of primary importance given the role of temperature in the phase diagram and in the study of ordering phenomena in cuprates. Furthermore, the detection of ordered patterns requires diffraction-like experiments with a huge precision in the sample control.

As already said, the main contributions in a RIXS spectrometer to the finite energy resolution are: (i) finite source size, (ii) limited spatial resolution of the detector, (iii) grating slope error, (iv) coma aberration. These are considered independent contributions, so, to achieve the final combined resolution, we sum the variances associated to them with the squared error related to the finite energy band of the monochromator of the incoming beam, to take into account also the contribution given by the beamline. To assess the value of the resolution a polycrystalline sample of graphite is used: since it does not show any energy loss feature one measures the width of the elastic peak coming from the light scattered by this sample. The combined resolution at the Cu-L_3 edge (931 eV) of AXES was 235 meV, while for SAXES (installed at Swiss Light Source) at the same energy it is 120 meV. The factor of two in the resolution reflects the fact that SAXES is twice as long as AXES. The bigger resolution is paid in terms of count rate, since the angular acceptance is lower. This is the problem which has to be faced in general in soft-RIXS: the tradeoff between energy resolution and count rate (which impacts on the availability of beamtime), together with the sample positioning and orientation control, which, we want to stress it once again, has to be achieved in vacuum.

ERIXS is the result of an optimization process aiming to solve the problems described above: increasing the count rate and energy resolution at the same time, while providing high precision sample control. The result is an instrument with: (i) high energy resolution, since it features a combined bandwidth of 35 meV; (ii) a polarization analysis system (the polarimeter), which gives access to the symmetry of the states generating the scattering; (iii) diffractometer-quality control of the sample orientation and continuous control of the scattering angle (in UHV) (to give an idea of the huge improvements made, notice that these functions were carried out manually in AXES); (iv) high luminosity after the introduction of a collimating mirror, which increases the count rate.

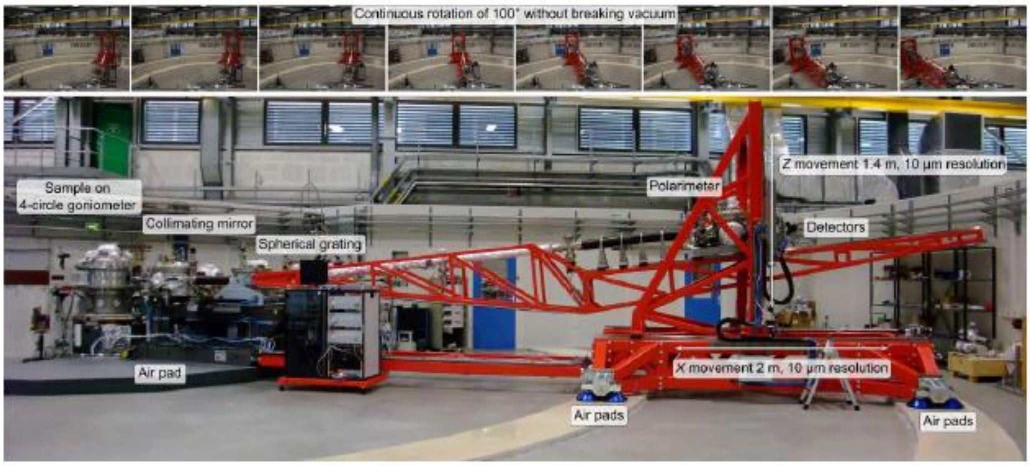

Figure 3.7: ERIXS at ID32. Top: sequence of pictures showing the 100° continuous rotation of the scattering arm, defining the value of the scattering angle 2θ. Figure taken from Ref. [52].

The scattering arm of ERIXS is 11 m long and it is capable of a 100° rotation (see Figure 3.7) without breaking the vacuum, thanks to a sliding steel ribbon placed on the vacuum chamber where the sample is mounted (designed by the Cinel Company [57]). The motion of the whole spectrometer takes place on air pads over a marble rail to reduce the friction. To allow the full control of the orientation of the sample (which in a RIXS experiment is fundamental as outlined in paragraph 3.2.2), the sample holder is locked on a 4-circle sample goniometer. A cryostat, working with liquid helium is also present, allowing to cool down the temperature of the sample to 20 K, with all the possible movements preserved.

The length of the spectrometer and the horizontal dimension of the detector determine also the angular acceptance and therefore the momentum resolution, which are anticorrelated with the count rate. So, on one side the increased length of the machine increases the energy and momentum precision, but on the other it negatively affects the count rate. To increase the count rate without giving up the energy resolution achieved, a new optical element is introduced in ERIXS: a collimating mirror. This mirror makes a huge difference, compared to the former implementations of RIXS spectrometers, because it increases the angular acceptance in one of the two dimensions of the beam coming from the sample. In this way, it worsens the momentum resolution, but it provides a big gain in terms of count rate, while leaving unaltered the energy resolution which is influenced by the spatial dispersion of the beam in the orthogonal direction (the other dimension of the beam footprint).

The competition between energy resolution and count rate in ERIXS is essential given the increased length of the scattering arm. So, other two new optical elements are introduced: two interchangeable spherical gratings. These elements, which conceptually execute the same function they had in the past versions, give us the possibility to choose between a high resolution (HR) or high efficiency (HE) mode. The HR mode is characterized by a lower count rate but by an energy combined resolution of 35 meV, whereas the HE mode slightly worsens the resolution (equal to 50 meV, by the combined contributions of the beamline and of the spectrometer) but enhances the count rate. The difference in the two gratings is given by the density of grooves they have. As said above the energy resolution can be estimated by measuring the signal from a sample of polycrystalline graphite: Figure 3.8 shows the results obtained for the HE configuration.

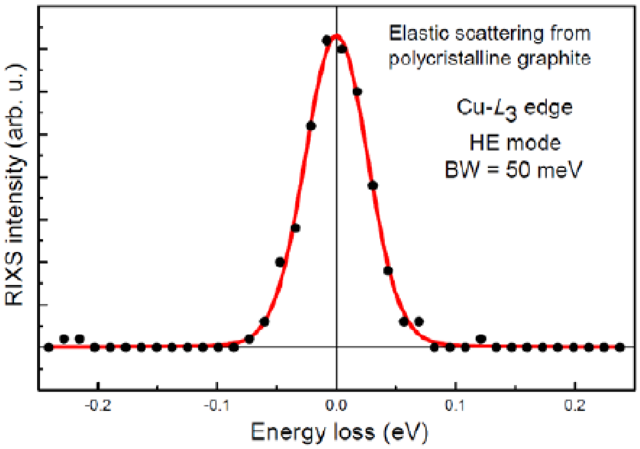

Figure 3.8: Elastic response from a sample of polycrystalline graphite at 931 eV in the high efficiency configuration. This result demonstrates a resolving power $\Delta E/E_0$ of 20,000 (ΔE being the combined resolution and E_0 the energy of the incoming photon). Figure taken from Ref. [8].

Finally, we refer to

Figure 3.9 to show an example of the improvements in performances given by the new ERIXS spectrometer compared to the results of AXES:

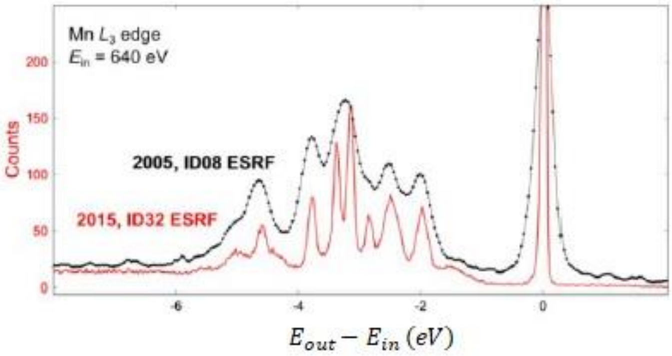

Figure 3.9: MnO spectra at the Mn L3 edge. Black: data from AXES, red: data from ERIXS. The improvement in the resolution is clearly visible. Figure from Ref. [8].

3.2.4.1 Polarimeter

Here we briefly outline the working principle of the polarization measurement in ERIXS by the introduction of the polarimeter, following reference [58]. To perform the distinction between the two outcoming polarization channels it is necessary to acquire two different signals: this is possible via a second CCD camera positioned after the deflection from a multilayered mirror (see Figure 3.10). The *parallel* measurement of the two different channels allows polarization analysis. A polarimeter was mounted on AXES back in 2011: it consisted of a multilayer able to divide the scattered light in the crossed and non-crossed channels, respectively associated to the excitation of spin-flip and non-spin-flip processes in the sample. The evolution of this first device mounted on ERIXS is able to perform the same kind of analysis with a better energy resolution, with larger band-pass and also with an improved count rate, covering the energy range of the K edge of oxygen and of the Cu-L3 edge.

The problem in polarization measurements is to avoid the deterioration of the energy resolution: in fact, while in the hard x-ray regime very efficient Bragg optics can be used, in the soft range the problem is the low efficiency of the optical elements forcing to perform these experiments with low or no energy resolution. The polarimeter designed by the group of Prof. Ghiringhelli and Prof. Braicovich overcomes these problems by exploiting the polarization dependence of the reflectivity of a multilayered mirror. This optical component is added just before the CCD camera (see Figure 3.10) and it is made in such a way that it does not affect the vertical dispersion of the beam, which determines the energy resolution, and thus it does not deteriorate the properties of the instrument.

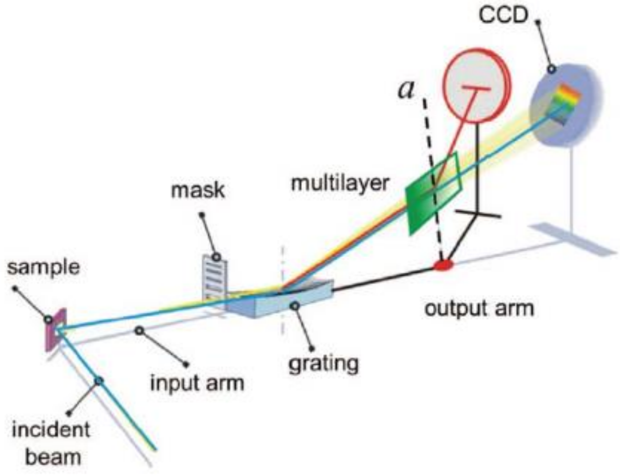

Figure 3.10: the multilayer mirror (green) is inserted before the CCD camera of the standard operating configuration of the spectrometer, along the output arm. Figure taken from Ref. [58].

The working principle of the multilayer is based on the exploitation of Bragg reflection conditions for the incoming light at a given energy: the result is that the reflectivity for the σ' component of the scattered beam is larger than the reflectivity for the π' component (this effect is maximum at the Brewster angle). Recall that the for the incident (scattered) beam the components of the polarization orthogonal and parallel to the scattering plane are named σ, π (σ', π') respectively. The polarimeter can be regarded as a low efficiency (only about 10% of the light is reflected) filter, which preferentially transmits scattered photons with a certain direction of the polarization. Thus, it is possible to decompose each spectrum in the two linear components of the polarization, which are both acquired with the same energy resolution. The reflected intensity is decreased by a factor equal to the average reflectivity of the multilayer, so by knowing that value and the values of the reflectivity for the σ' and π' components it is possible to fully decompose the initial spectrum into the two different polarization channels.

To keep a constant efficiency over the fan of different directions of the scattered light comprised in the acceptance angle, a collimating mirror is introduced. In this way, all the photons impinge on the multilayer with the same angle, for which the reflection is optimized, so the signal is strongly increased. The problem of restricted bandwidth for the polarimeter in AXES has been solved in ERIXS via the introduction of a gradient in the period of the layers along the vertical direction, along which the photons with different energies are dispersed. In fact, a grading in the spacing along the vertical direction ensures optimized reflection conditions for all the dispersed energies without distortion of the signal at different energy losses. Thus, there is no need now to cut the signal outside the energy window where the reflectivity of a multilayer with a fixed period is more or less constant with energy (as it was the case in AXES). This expedient also increases the efficiency of the instrument.

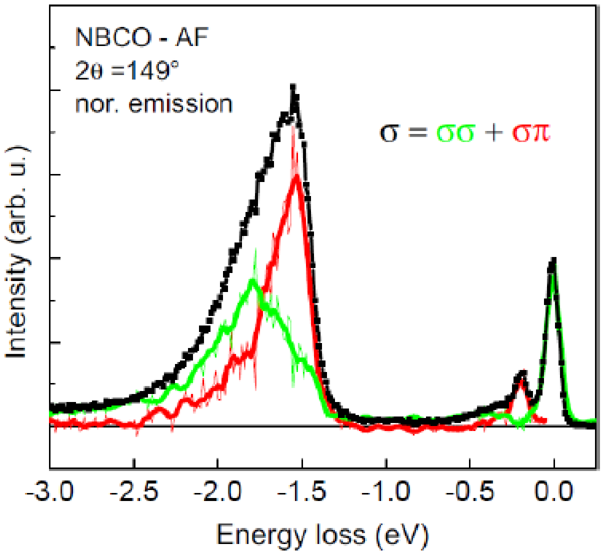

Figure 3.11: First spectrum, taken with ERIXS, with σ incident radiation, in which the polarization analysis has been performed. The sample analyzed is the antiferromagnetic parent compound NBCO. Black: total spectrum, green: non-crossed component, red: crossed component of the polarization channels. Figure reproduced from Ref. [8].

Figure 3.11 represents the first spectrum in which polarization analysis has been performed with the ERIXS polarimeter. The crossed channel in the low energy scale is associated to magnetic excitations, while the non-crossed component of the spectrum is related to the elastic peak. Compared with the old implementation on the AXES spectrometer, now the pass-band is wider without significant losses in resolution thanks to the vertical modulation of the layered mirror introduced above.

Chapter 4

Experimental Results

The experimental data presented in this section have been taken at ESRF on May 2017 during the experiment HC2999 at the beamline ID32. In addition to this set of data, we present here the analysis of the unpatterned films of $YBa_2Cu_3O_{6+\delta}$ measured during HC2393 discussed in chapter 2. This second group of data, has not been taken with the same scope of the experimental measurement performed in May (specifically to assess the onset temperature of charge order in superconducting cuprates, see next paragraph). Nonetheless, it is presented to give support and to enlarge the phenomenology of 123 superconducting materials discussed here. In the following we outline the results of the analysis of these data and we compare them both with the existent literature regarding other phenomenological findings on cuprates and with the theoretical framework provided by the group of Roma La Sapienza.

4.1 Motivation of the Experiment

The motivation of the experiment is to discover the 'real' onset temperature for the charge order (T_{CDW}) in $NdBa_2Cu_3O_{6+\delta}$. The importance of a precise assessment of this temperature is huge, both on a self-standing basis, to add another piece to the complex puzzle of charge order in high T_c superconducting cuprates and to give experimental background to the theories trying to explain this exotic phenomenon. As discussed in chapter 1, charge order and superconductivity compete, thus the apparent phase transition of CDW in underdoped cuprates (p=0.11-0.13) to a completely ordered phase upon cooling, is stopped at T_c, when superconductivity arises. Therefore, we have a maximum of the strength of charge modulations at T_c (see Figure 1.12 and Figure 1.13), and a decrease of its intensity at lower temperatures. Conversely, when a magnetic field is applied the order parameter resembles the behavior of a real phase transition.

To be more specific, the importance of an accurate determination of the real onset temperature is also connected to the precise evaluation of the relationship between charge order and the pseudogap regime, between CDWs and the Cooper pairing mechanism and with the anomalous metallic properties in the cuprates phase diagram [59]. In fact, many suggest a possible link in hole-doped cuprates of charge order with the pseudogap transition, owing to the proximity of the onset temperature $T_{CDW}(p)$, with the pseudogap temperature $T^*(p)$ (which is the doping dependent temperature below which the pseudogap opens). On the other hand, these experimental data are crucial to distinguish between two hot theoretical frameworks trying to explain charge order: one hinges on the "Mottness" (i.e. the set of typical characteristics of the Mott state) of the cuprates in the underdoped regime, the other is based on a quantum critical (QC) point of view [3]. To better illustrate, the first theory regards the charge order as a mere "epiphenomenon" naturally arising from the intrinsic properties of the non-

Fermi liquid phase characterizing the underdoped cuprates (i.e. from the "Mottness" of this state). Instead in the second case, the charge order (considering the competing action of superconductivity only via a pairing dependent scattering term [3]) undergoes a real phase transition to a static ordered state, in a precise range of doping levels and temperatures, delimited by two quantum critical points (see the light blue dome of Figure 4.1). In this last scenario, charge order is an independent phenomenon which arises, in the form of nearly critical CDW fluctuations, as the temperature and doping levels get closer to the region of the phase diagram where a truly ordered phase is present. Then, Caprara et al. [3] go on explaining how this ordering phenomenon interacts in different ways with superconductivity and with the Fermiology of the material.

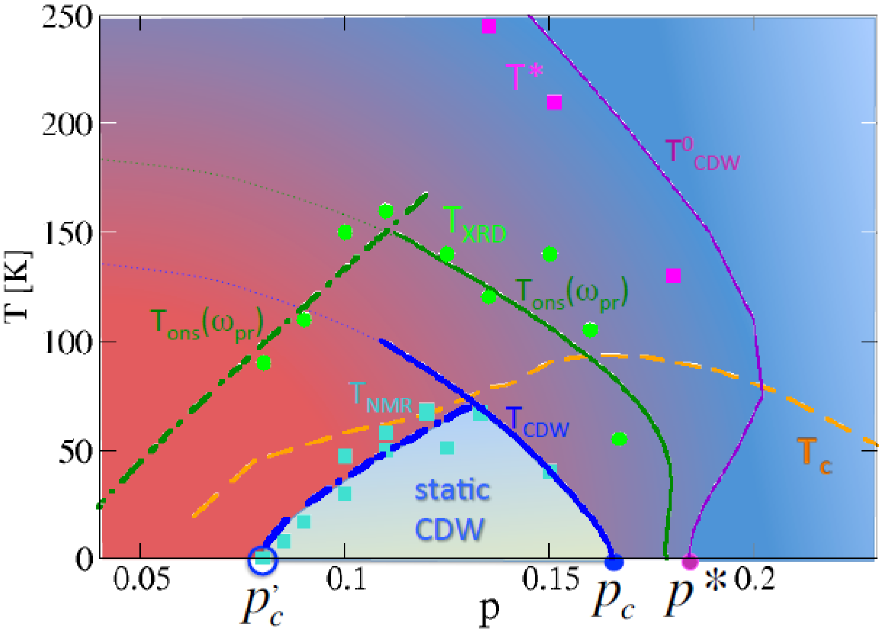

Figure 4.1: Phase diagram of YBCO. The light blue dome defines the calculated region where the charge order becomes static, and is delimited by two quantum critical points (p_c and p_c'). The red background indicates the region where the correlation of the amplitude of charge order grows, but the area of static CDWs does not coincide with this regime due to random fluctuations of the phase of the order parameter at lower dopings (see also Mesaros et al. [6] reporting increasing phase disorder for lower doping levels). The orange dashed line indicates the experimental superconducting dome, the magenta squares the measured pseudogap crossover temperature T*. Green dots represent the onset temperature seen in the fluctuating charge order regime by a fast probe like XRD (see next paragraph) whereas experimental results by a slow probe like NMR can see just the static order (light blue squares). T^0_{CDW} (purple thin line) represents the calculated mean-field onset temperature, while T_{CDW} (blue solid line) is the mean-field onset for static order when also thermal fluctuations and a small coupling between different CuO_2 planes are considered. The green solid line shows the calculated onset temperature for fluctuating charge order as seen by a probe with characteristic frequency $\omega_{pr} = 50\ K$. The blue and green dotted-dashed lines in the underdoped region, are the analogous of the solid lines with the same colors, with the difference that here the charge order is destroyed by phase and not by amplitude fluctuations. Figure reproduced from Ref. [3].

Another reason pushing this experiment, is the determination in general of the wavevector, of the correlation length and of a possible connection with Fermi arcs driven instability of charge order [59]. In fact, new experimental data can clarify the role of phase-locking discommensurations [6], or of the shape of the Fermi surface [25] in the establishment of CDWs, as already discussed in chapter 2. Moreover, a critical aspect in the experimental measurement of charge instability in cuprates is the fact that different probes (like RXS, NMR, quantum oscillations, XRD) measure different onset temperatures. A possible explanation for this circumstance is the fact that the "speed" of each specific technique is responsible for the different onset temperatures found [3] (see also Figure 4.1). In fact, following the quantum critical point of view introduced above, we can identify a relatively small region of the phase diagram where the charge order is static versus another much larger portion, extending to high temperatures, where the charge order is fluctuating. In this framework, the speed of the probe plays a relevant role in determining the onset temperature: indeed, a slow experimental technique will measure a lower onset temperature than a faster technique. When fluctuations rule the charge order state, the characteristic time of each probing mechanism becomes relevant because it must be compared with the period of the fluctuations: if the time in which the measurement is carried out is smaller than the characteristic time of the fluctuations, then we are safe since the probe is taking an "instantaneous picture" of the CDW and so we can see something, the signal is non-zero. On the other hand, if the probe is slow and thus it averages over multiple fluctuations, the signal we see is zero, besides the case in which temperatures are low enough to drag the time of the fluctuations below the characteristic time of the probe. This could be the reason why a slow probe as nuclear magnetic resonance (NMR), finds charge order at lower temperatures than a fast probe like RIXS which has a characteristic time of interaction of order of the femtosecond (which is the lifetime of the intermediate state): NMR mediates over fluctuations and detects only the static part of charge order, while RIXS is sensitive also to the dynamic part mediated over an area with micrometer size. So, another goal spurring this experiment is the determination of the dependence of T_{CDW} on the timescale of the probing technique [59], to possibly confirm the theory by Caprara et al. [3] outlined above.

Finally, in light of the discussion made above regarding the onset temperature, another objective is to evaluate the relation between the pseudogap regime and the onset of charge order. In fact, the proximity found in previous experiments in hole-doped cuprates between T_{CDW} and T* pointed at a connection between these two phenomena. The experiment described in this chapter, with the purpose of measuring with unprecedented precision the onset temperature, aims to shed light on the point introduced above, which is another crucial evidence to single out the character of charge order in cuprates: Mottness or quantum criticality? If the pseudogap marks a real transition to the peculiar non-Fermi liquid state than charge order, being a side effect of this new Fermi state, must start at the pseudogap temperature. On the other side, in the QC point of view, the pseudogap temperature is just a crossover point below which the fluctuations become stronger given the contiguity of a truly ordered phase [3].

Resonant x-ray scattering performed at the Cu-L_3 absorption edge is the right technique to perform these measurements. In fact, the resonance provides a strong enhancement of the experimental sensitivity, essential to mark correctly the onset temperature which by definition involves the measurement of weak signals. On the other hand, even though charge modulations in cuprates mainly affect the 2p orbitals of oxygen atoms [27], the Cu-L_3 edge is still suitable to probe them thanks to the strong hybridization of Cu 3d and O 2p orbitals. Previous experiments performed with RXS (energy integrated technique) [31], found charge order at temperatures not higher than 160 K in YBCO (for p~0.12, see the shape of the onset temperature in Figure 1.4). In any case in the hole-doped cuprates, charge order has never been found above 180-200 K [59]. By using RIXS the goal of this search is to focus on the quasi-elastic region of the signal which is the one related to the almost static charge order. Thus, thanks to the energy selectivity and to the unequalled resolution of the experimental setup available in ID32, the group of Prof. Ghiringhelli who designed the experiment, wanted to discover whether some residual signal related to charge order is still present at temperatures higher than 200 K. This is possible because RIXS can extract the specific amount of signal related to the charge instability form the narrow spectral range of photons scattered by CDWs. In fact, the standard procedure in energy integrated measurements is to use a scan at room temperature or at a temperature above which the signal is temperature independent [31], as background and to subtract it from the data taken at lower temperatures, to determine the elastic peak associated to charge modulations [59]. This kind of analysis is based on the assumption that at room temperature no peak associated with the charge order is present and that the inelastic part of the signal does not vary with temperature: in this way subtracting the high temperature scan we should get only the signal from charge order. In reality the inelastic background, which is the overwhelming majority in RXS, can possibly vary with temperature. In fact, for instance the dd excitations, which are taking the greatest part of the spectral weight (see Figure 3.3), are sensitive to variations of the crystal field which in turn, being associated with the lattice positions of the ligands atoms, can be affected by temperature; moreover, the inelastic part of the spectrum could also vary with the value of the momentum transferred, further complicating the analysis (see for example charge transfer excitations which are weakly dispersing [8]). Actually, the latter is a problem also for RIXS, coming into play in the normalization procedure chosen (see paragraph 4.2). Regarding temperature variations, our data show that the elastic background varies, as it is possible to see in Figure 4.3. One possible problem associated with the RXS background determination, which the selectivity of RIXS allows to avoid, is this: if there is an opposite variation of inelastic signal and CDW such that above a certain temperature they compensate each other yielding a constant signal (the background), with RXS we cannot disentangle the two contributions and we are discarding good information. So, this experiment exploiting the resolution capabilities of the new ERIXS spectrometer aims to challenge the previous measurements reporting an onset temperature bound to 200 K in the 123 family. Specifically, RIXS should be more accurate than RXS, because it can access the truly elastic intensity which is the only signal coming from the static order parameter, and highlight better the information coming from the CDW instability since it can separate it from other dispersing signals (at least for features at energy losses below the narrow integration range, see paragraph 4.2). The final goal would be the exact determination of the order-disorder transition temperature.

The samples chosen are films of NBCO, at five different doping levels from the underdoped to the optimally doped regime. The films are grown on $SiTiO_3$ (STO). This substrate guarantees that the oxygen atoms arrange in a tetragonal structure around the copper atom. Given the symmetry that is thus created it is sufficient to measure the charge order peak just along one of the two directions of the reciprocal space [59]. Moreover, these samples (which are the same kind of samples where charge order was discovered in the 123 family [5]) have flat and uniform surfaces and suffer low radiation damage, so they are suitable for this experiment in which the RIXS measurements are performed also at high temperature, where the risk of damaging the sample strongly increases.

4.2 Data Analysis and Results

The data analyzed in this paragraph are the experimental results of the measurements, performed at ID32, of an underdoped sample of NBCO with critical temperature of 60 K (called UD60), an optimally doped sample of NBCO with T_C=90 K (OP90) and an underdoped YBCO sample, T_C=81 (UD81). The two NBCO samples belong to the group of samples brought at the HC2999 experiment (May 2017) described in the former paragraph, while the data of the UD81 YBCO sample have been taken during the HC2393 experiment (January 2017) described in chapter 2 from the unpatterned films.

The experimental configuration chosen is similar to that shown in Figure 3.5, with the scattering plane orthogonal to the CuO_2 planes and passing through the c axis. Figure 4.2 represents two sketches indicating the directions of the reciprocal space probed during the two experimental sessions. The scan along the H direction (hereafter H-scan) is actuated by varying the value of the angle δ (see Figure 3.5), while for the K-scan there are two options: in the case of NBCO where the scan along K is performed at a value of H coinciding with the position of the maximum of the peak (previously found by the H-scan) different momentum transfers are achieved by changing the angle χ. On the other hand, for YBCO, where the K-scan is performed on axis (with a corresponding value of the H component of the transferred momentum equal to zero, see Figure 4.2), first the angle φ, describing a rotation around the c axis, is rotated of 90° and then the angle δ is varied in a similar way done for the H-scan.

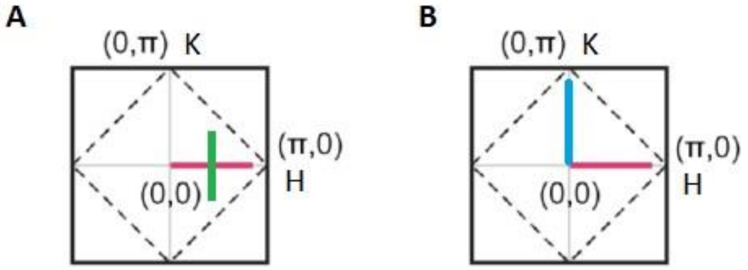

Figure 4.2: Scans of the reciprocal space performed during HC2999 (A) and HC2393 (B). In (A) only the peak along the H direction of the reciprocal space is measured due to the intrinsic symmetry of the reciprocal space induced by the tetragonal geometry of the oxygen atoms. Purple: H scan, green: K scan. (B) the peaks are asymmetric in the two directions of the reciprocal space so both the H and K (purple and blue) directions are scanned, but no off-axis scans are taken.

In the case of NBCO it is possible to calculate the volume of the peak in the H direction ~(0.31,0) (see Figure 4.7), even though in an approximate way, since we have information about both its directions. On the other hand, for YBCO this estimation is impossible because we lack half of the information regarding the shape of the peak. In fact, the anisotropic shape of YBCO peaks has been already demonstrated by Comin et al. [30]

and discussed in previous chapters, so we cannot make the assumption that the dimensions of the peak along the H and K are equal, to calculate the volume. Furthermore, to complicated the situation, in this YBCO sample the peak related to charge order doubles along the K direction due to a particular reconstruction triggered by the MgO [110] substrate (see Figure 4.3).

Figure 4.3 shows the raw data of all the scans for the three samples analyzed. As it is possible to see the elastic background presents sizable variations with temperature, specifically it increases. It is easier to spot this trend in the data of the OP90 since there the range of values in the y axis is narrower given the weaker intensity of the CDWs in the optimally doped sample. In any case the increment with temperature of the elastically scattered light by the sample, is present in all the measured data. As anticipated before, it is evident in the raw data of UD81 K-scan the presence of a double peak. In accordance with what has been reported by Blanco-Canosa et al. for YBCO [31], the scans in the underdoped NBCO present two clearly distinguishable spectral features: a very broad almost temperature independent peak, slightly shifted toward smaller values of H and a narrow peak which vanishes at temperatures higher than 190 K. The same should be valid also for the YBCO UD81 data presented here, but the splitting in two peaks along the K direction of the charge order peak, introduces a great amount of noise which makes it difficult to single out the two distinct components.

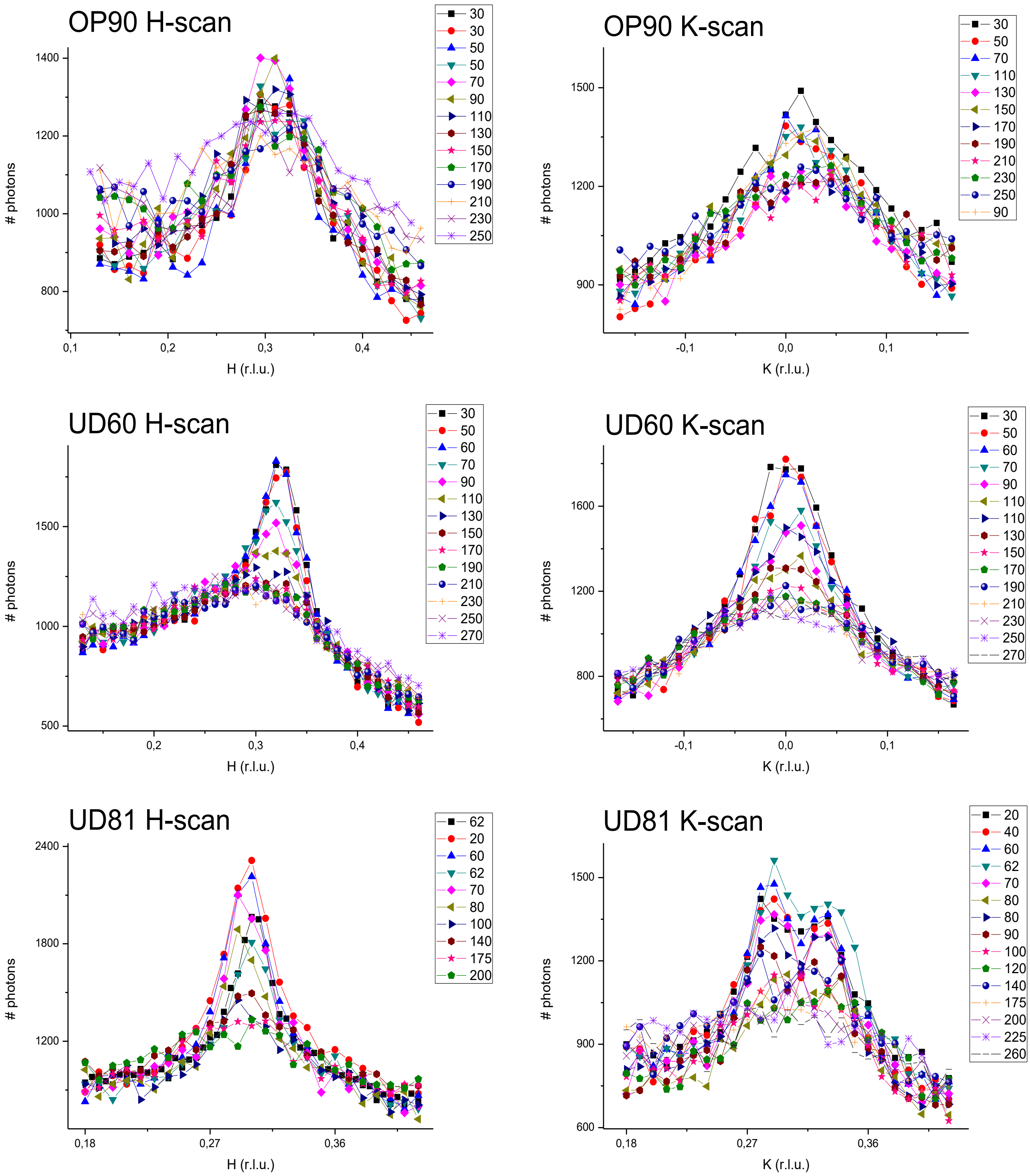

Figure 4.3: Raw data from the different samples measured. The intensity of the CDW peak is given as the total number of photons measured for each point of the reciprocal lattice integrated in the energy interval related to the quasi-elastic charge order signal (from -0.2 eV to +1.5 eV). Note that for the UD81 K-scan two peaks are distinguishable, while in the H-scan of the same material there is a single peak because we are measuring the "valley" in between the two peaks displaced in the K direction. Moreover, note that the signal of NBCO is weaker for the optimally doped sample than in the underdoped regime.

Blanco-Canosa et al. discarded the broad peak from their analysis, subtracting it as a background, and concentrated only on the narrow spectral feature, which indeed they found only up to 160 K (in the analysis reported here this peak goes to zero smoothly at 210 K, see Figure 4.6). In this work, we follow as a theoretical reference the article of Caprara et al. [3], in which two different regimes of charge order are defined: one is represented by static CDWs living in a dome enclosed between the two quantum critical points of the underdoped region of the phase diagram ([31], [10]). From this dome, quantum critical charge fluctuations start (see Figure 4.1), giving rise to a second kind charge order, which is dynamical and thus distinct from the former CDW, visible up to higher temperatures, i.e. the probe-dependent onset temperature (see the green dots and the light blue squares in Figure 4.1). For this reason, we do not subtract the broad peak, which also from our analysis seems to be quite temperature independent, as in the data taken by Blanco-Canosa et al., and we fit it to retrieve its relevant parameters.

Before showing the results of the fitting of the data displayed in Figure 4.3 we briefly explain in which way these spectra were retrieved. The experimental measurements were recorder in the single photon counting mode (SPC), introduced in paragraph 3.2.4. Thus, the raw material from which we can start is the number of photons collected for each energy loss during the time in which each point of the reciprocal lattice is measured (about two minutes in total). In other words, the value of the transferred momentum is varied adding equal steps (each one of these as wide as 0.01 or 0.015 r.l.u.) along the direction of the reciprocal space scanned, and for every point of the reciprocal space, an energy loss spectrum is taken. To have a better statistic and reject some white noise, for each point of the reciprocal space four spectra of 30 seconds each are taken and then summed up yielding the final spectrum. The quantization of the energy axis is determined by the spatial resolution of the CCD detector and for all of the data described here (which were taken in the high efficiency mode of ERIXS) it is almost equal to 10 meV. In the beamline, right after the spectra are measured, they are aligned: that means that the zero of the energy-loss has to be assigned. In the case of high efficiency mode, where the throughput of the spectrometer is quite high, there is no time to take a specific reference for the zero energy position of every spectrum and the alignment of each energy spectrum composing the energy-momentum map is made by eye. Thus, often the zero energy-loss point is not that reliable. For this reason, an automatic algorithm to align the spectra has been adopted (see

Figure 4.4): each spectrum is first linearly interpolated with an energy resolution of 1 meV, and then the half part corresponding to positive energy losses of the elastic peak is fitted with a resolution limited gaussian (50 meV FWHM). In fact, the part of the peak at positive energy losses must be given just by the broadening of the elastic peak convoluted with the response function of the instrument, if we assume that no anti-stokes processes are present (and we do so). Furthermore, it has to be stressed that this procedure is possible because of the particular shape of the spectrum we have to fit. Since we have a quite intense asymmetric quasi-elastic peak, which rises with a steep slope from the positive energy loss part and reaches almost immediately its maximum, we can easily find the range of values to fit, by finding the abscissa corresponding to the first ordinate (coming from positive energy losses) equal to 3/4 of the maximum of the signal in the quasi-elastic region. We avoid to take the maximum because it could be located at a finite energy loss value. Moreover, due to the sharpness of the peak and due to the steep slope of the signal (coming from positive energy losses) the factor 3/4 gives us sufficient confidence about the fact that we are not taking values belonging to energy loss features. Having found the best gaussian (coinciding with the line shape of the response function, see Figure 3.8) with fixed width (the energy resolution), fitting the values in our positive-energy-loss range, the vector containing the measured number of photons is shifted in a way such that the zero energy-loss point coincides with the center of the gaussian found. By doing this, we keep just one energy axis for all the spectra related to all the different momentum transfers measured. This comes handy when performing integrals in specific energy regions.

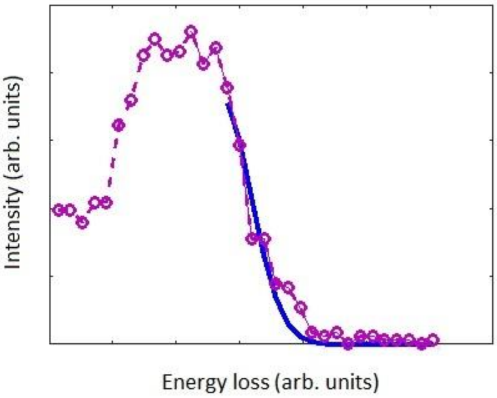

Figure 4.4: Example of the automatic alignment procedure performed with a high temperature (250 K) OP90 spectrum. In this case, we have the weakest CDW signal and elastic peak is broader (along the energy coordinate) than at lower temperatures. So, we are testing the algorithm in the worst conditions. The purple dots represent the quasi-elastic region of the experimental spectrum, while the blue solid line represents the portion of the resolution limited fitting gaussian in the range of values used for the fit. That is, from 3/4 of the maximum of the quasi-elastic region to the right.

The interpolation of the initial dataset in a larger number of energy points, allows to shift more precisely the vector of measured photons compared to the energy axis. Indeed, a shift of 10 meV (the initial distance between adjacent energy points of the spectrum) often should add more noise to the alignment of the spectra than leaving them untouched as they come from the beamline.

At this point we sum the photons in the range of energies related to charge order. In principle, if the signal associated with the CDW were completely elastic (and this is the case with the present resolution) and if the alignment were perfect, one should take only the positive energy loss part of the spectrum to retrieve the intensity of the elastically scattered photons only (as suggested by Prof. Braicovich and Mr. Fumagalli). The problem in doing this with our data is that we would retrieve too noisy results. In fact, even though the data have been realigned, the noise of the original spectra (due to the "brief" acquisition time) and the energy spacing given by the resolution in the high efficiency mode, prevent us to perform such an analysis. So, to be sure all the elastic signal from the charge order is collected, we sum in the energy range from -0.2 eV to +0.15 eV. Extending the interval toward the positive energy loss region is quite safe, because no other spectral features are present (besides some noise). Instead, the lower extreme we chose for the energy interval, does not allow to single out the signal related to charge instability from possible contributions coming from phonons or magnons or other spectral features located at a finite energy losses. Notice also that this sum of the interpolated spectra is divided by a suitable constant, depending on the number of points used for the linear interpolation, in order to conserve the original value of the sum of measured photons.

So, after all this tedious explanation we are left with a pure number of photons related to the charge order as a function of different values of the momentum transferred. Here another problem comes in: the quite long time it takes to measure each single reciprocal lattice point (>2 minutes) makes it dangerous to compare, without any correction, points belonging to the same scan, let alone comparisons among different momentum maps. In fact, each scan is made by thirty points or more. This is mainly due to the fact that the x-ray beam from the storage ring is not stable over time: each 24 hour there is a refill, new electrons are accelerated in the *linac* and then in the booster to restore the current inside the storage ring to the desired levels since it decreases exponentially over time. Moreover, there could be other problems affecting the stability of the measurement over time. To hedge in these stability problems that prevent the comparison between data taken in different moments, we perform a normalization procedure that at the same time allows to keep the information about the real number of photons measured. First we sum all the inelastic contributions below the lower extreme of the CDW integration interval, mainly composed by dd and charge transfer excitations, and then we divide the value related to charge order by this number for each spectrum. We are interested in comparing data belonging to homogeneous classes, so we divide the raw data as a function of the material (Nd123-UD60, Nd123-OP90 and Y123-UD81) and of the type of scan (H and K). After this we multiply the ratio described above (containing quantities related just to a specific spectrum) by the maximum of the averaged value (across the different momentum transfer values of every map) of the sum of the inelastic features in the class to which the specific spectrum belongs. Restated: we have various momentum-energy maps, which can be grouped into categories (for instance referring to Figure 4.5 we have that UD60 K-scan identifies a class). For each reciprocal lattice point, belonging to a map taken at a precise temperature, we calculate the sum of the inelastic features ($I_{inelastic,q}(T)$). Then we average $I_{inelastic,q}$ across all the q values of the map, obtaining $\bar{I}_{inelastic}(T)$. We repeat the procedure for all the different temperatures (i.e. for all the different maps) and we get a temperature dependent parameter characteristic of each map, which mostly depends on the incoming photon fluency of the x-ray excitation beam. As a normalization factor, we choose to take the maximum of this temperature dependent signal ($\bar{I}_{inelastic}(T)$): $\bar{I}_{inelastic,max}$, which should be related to the maximum incoming photon flux. Note that we average the values across all the q in each map to avoid to take a maximum value which could be an outlier, spoiling the comparisons among different classes. In formula:

$$I_{CDW,q} = \left({}^{I_{elastic,q}}\big/_{I_{inelastic,q}} \right) \cdot \bar{I}_{inelastic,max} \tag{4.1}$$

Where I is a number of photons. $I_{CDW,q}$ represents the value at the reciprocal lattice point q of the spectra shown in Figure 4.3, ready for the fitting. It has to be said that this kind of procedure considerably reduces the noise of the spectra. In Figure 4.5 it is possible to see the benefits brought by it: in fact, in the first set of fitting data ("not rescaled") instead of $\bar{I}_{inelastic,max}$ we multiply each map by the average inelastic sum associated to itself: $\bar{I}_{inelastic}(T)$, shown in Figure 4.5.C. The latter temperature dependent signal contains a contribution of noise linked to the different values in time that the incoming x-ray beam assumes, averaged over the time necessary to measure a complete map. This normalization procedure has been proposed by Prof. Ghiringhelli and improved by Dr. Peng.

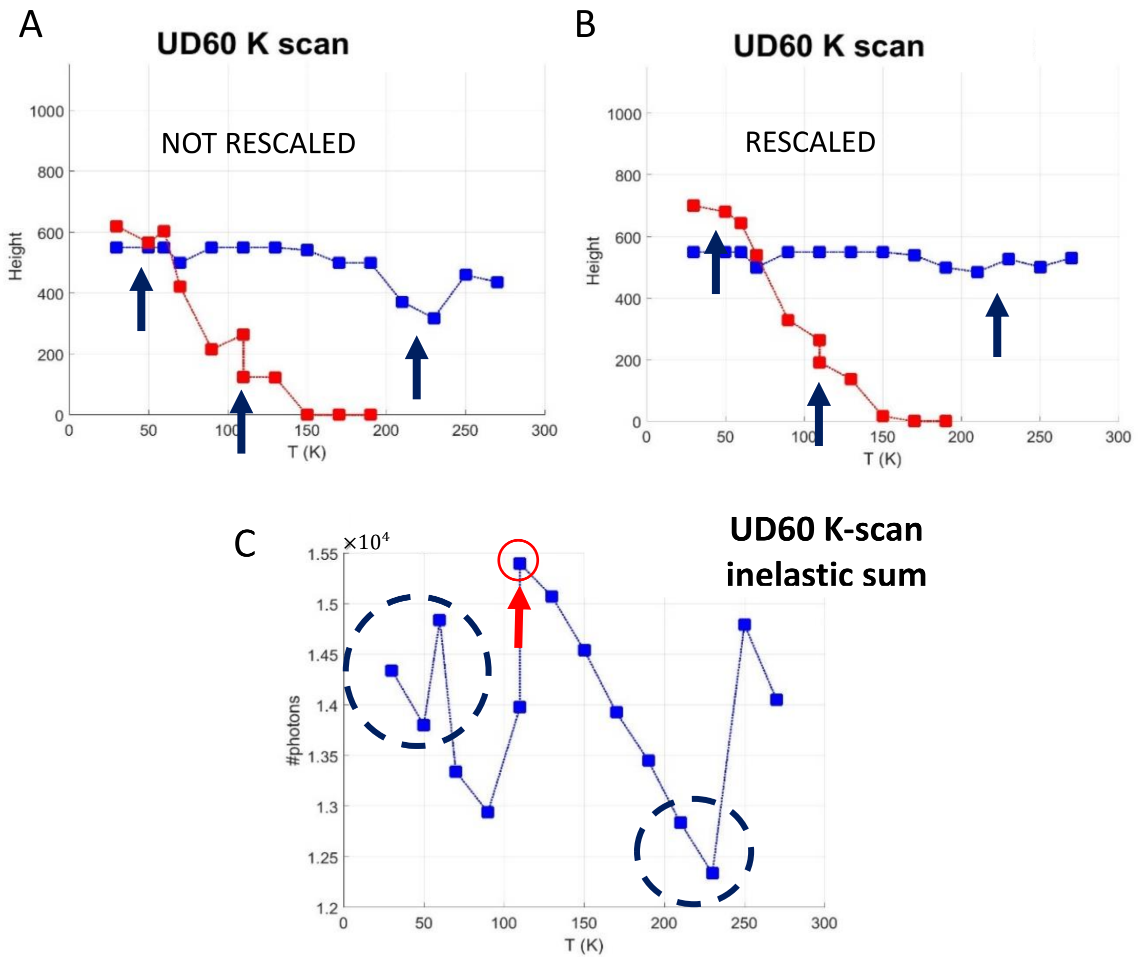

Figure 4.5: (A) and (B) represent respectively the height (expressed as a pure number of photons) of the two Lorentzian line shapes resulting from the fitting of the raw data of UD60 K-scan with two different normalization procedures. Red points indicate the temperature dependent narrow peak, blue points the constant broad peak, see Figure 4.3. In (A) the ratio $I_{elastic,q}/I_{inelastic,q}$ in each map (taken at a precise temperature T) is multiplied by $\bar{I}_{inelastic}(T)$, shown in (C), which results from the average in q of the inelastic intensities of the same map (at that given temperature). When there are two maps at the same temperature, as it happens at 110 K, we keep track of them separately and we multiply each map by its own average value. Instead, in (B) the ratio is multiplied by the maximum value (red circle) of (C). The dark blue arrows indicate the points where the noise is mostly reduced and the dashed circles in (C) represent the cause of the initial noise (found in the scattered values of the incoming beam flux over time, which are reflected on the values of $\bar{I}_{inelastic}(T)$).

Henceforth, we have a normalized number of photons for each value of the transferred momentum, which represents the intensity of the signal coming from the charge order in the quasi-elastic region of the spectrum. Thus, we are ready to fit the results and extract some information from the raw data. The OP90 has been fitted with a single Lorentzian line shape where the effect of the background has been taken into account by adding a constant and a straight line to fit it. The formula used for the Lorentzian curve is:

$$L(x) = H \cdot {(\Gamma^2/4)}\Big/{[(x - x_0)^2 + (\Gamma^2/4)]} \tag{4.2}$$

Where Γ coincides with the FWHM of the curve, and H represents the height for $x = x_0$ (x_0 being the center of the Lorentzian). During the experiment a scan along the (1,1) direction has been taken both at 60 and 250 K, as a reference for the background of the H direction. A scan orthogonal to the (1,1) direction at a distance from the origin coinciding with the distance of the CDW peak from the gamma point has been also taken, serving as a reference for the background of the K-scan. The idea was to subtract these two scans from the raw data to eliminate the background. The problem is that the two scans taken were not fitting closely the background of the measured signal and their subtraction added further noise. Especially the scan orthogonal to the (1,1) direction, which should have been used as a background for the K-scan, was not suitable because it took also some signal from the tails of the CDW peaks in (1,0) and (0,1) directions. So, after trying also different analytical formulas, the best choice to achieve a good fit of the background and keep the number of free parameters as low as possible, is the straight line plus a constant. In fact, given the relatively small amount of fitting points (about 30 for each spectrum in the momentum coordinate), a bigger number of free parameters and a more complex fitting function yielded artifacts in the fitted data. As already mentioned, for OP90 we used a plain-vanilla solution (the single Lorentzian), whereas for UD60 and UD81 data two Lorentzian curves are required. In fact, the raw spectra of the UD60 clearly show the presence of two peaks, while for the UD81 in the K direction we have two replicas of the same peak given by a surface reconstruction. Moreover, we tried a double peak fitting also for the H direction of the UD81, where apparently only a single peak is present. By looking more carefully at every spectrum, Prof. Ghiringhelli noticed that in each one of them a spectral contribution at higher values of momentum transfer than the center of the sharp peak was not well fitted. So, we tried to fit with two peaks also the H scan of UD81. While the theory by Caprara et al. [3] and a communication from Di Castro support the presence of two peaks in the 123 materials, the broad peak in YBCO H-scan was very difficult to see. Three possible reasons for this are: the sharpness and intensity of the narrow peak blurring the broad peak, the possibly too restricted range of q values scanned given the broadness of this spectral feature (and this is a problem for the fitting also in the NBCO data) and finally the fact that in YBCO H-scan we are not cutting precisely the peaks in their maximum due to the shift in the reciprocal lattice given by the surface reconstruction. In any case, adding a curve for the broad peak to the fitting in YBCO, does not influence the parameters of the other narrow Lorentzian curve fitting the narrow peak. Regarding NBCO, we must also say that the K-scans in UD60 were taken at the value of H coinciding with position of the narrow peak in the reciprocal space. For this reason, the FWHM of the broad peak in the K-scan, is not fully precise since the center of this peak is shifted towards smaller momentum values. Anyway, this error should be minor given that the difference between the positions of the two peaks in the H direction is much smaller than the estimated FWHM of the broad peak (see the positions for the broad and the narrow peak of UD60 versus its FWHM reported in Figure 4.9).

About the temperature dependence of the peaks retrieved from the double Lorentzian fitting, we used different strategies for the two materials. In YBCO we just stopped using two peaks when the fitting was not reliable anymore. Thus, at a given temperature when the two peaks broaden and their intensity decreases in a way that prevents to reliably find two fitting curves, we use only one Lorentzian. Since there is no physical reason for which the width of the two shifted peaks should be different, we imposed that the two curves used to fit the data have the same FWHM (see Figure 4.8). For the UD60 instead we acted in a different way: first of all, we arbitrarily assumed that the broad peak was constant in temperature without making any fit, just looking at the raw data of Figure 4.3. Then we subtracted a smoothed average of the spectra at the last three highest temperatures (230, 250 and 270 K) plus a free constant value to the low temperature data (we call this way of analyzing data "subtraction procedure"). The constant was found as the offset shifting the high temperature average in a way such that its tails matched the tails of the low temperature spectra. In this way, we found a set of data featuring a single peak, similar to the data used for the analysis by Blanco-Canosa et al. [31]. Then we fitted these spectra with a Lorentzian curve achieving a set of parameters as a function of temperature (till 210 K). At this point we should recognize that assuming no variation at all for the broad peak versus temperature could be a too strong hypothesis. So, we used the data of the fitting retrieved after the subtraction procedure, to help the automatic algorithm to fit the spectra with the double peak. In fact, we imposed a fixed value for the width of the narrow peak equal to the value previously found. In this way, the results from the double peak fitting are reliable till 210 K (which is the temperature up to which some residual track of the narrow peak is visible in the case of the subtraction procedure), since this strategy helps to extend the range in which the fitting with two curves is valid and to increase its reliability, as compared to the fitting with two peaks without any fixed parameter helping it to converge. Furthermore, to see whether the results of the unconstrained double fitting are consistent with the subtraction procedure, we compared the trends of the fitting parameters (especially height and width of the peak): at least for low temperatures the data are closely correlated. So, we feel confident about the choice of using the results from the subtraction procedure since it seems to be sound. To conclude we should note that also in the UD81 K-scan each peak should be composed by a broad and a narrow contribution (as could be the case for the H-scan of the same material). In reality the fact that we have two replicas does not allow to find the two contributions of each peak given the noise introduced by the partial overlap of the two spectral features.

4.2.1 Results and Discussion

In the following we present the results of the analysis performed. Figure 4.6 shows the FWHM and the intensity of the Lorentzian curves used to fit the data from NBCO. In the H-scan (first column) the intensity displays a barely visible anomaly at T_c (see paragraph 1.2.4.1) for the OP90, whereas for the UD60 broad peak it appears noisy and seemingly constant. The narrow peak decreases monotonically to zero (within the experimental error) as temperature increases. The FWHM does not show a minimum at T_c as expected, but increases with temperature becoming noisy for the highest temperature values. Regarding the K-scan (second column) we can see some evidence of the competition between superconductivity and charge order (especially in the FWHM): in fact, the intensity slightly peaks around T_c for the broad peak of UD60, while in the other cases it just decreases. But the FWHM clearly reaches a minimum at temperatures close to T_c for OP90 and for the broad peak of UD60, indicating the maximum strength of charge order. The non-monotonic behavior at higher temperatures could possibly be assigned to the noise of the data and to the too narrow interval of the reciprocal space probed, which could prevent a correct estimation of the shape of the peak when it becomes too broad. Interestingly, the signs of the competition superconductivity-CDW are present only in the broad peak of UD60 which could be associated with the fluctuating-dynamical charge order extending to high temperature (as supposed by Prof. Di Castro and Prof. Grilli), and not in the narrow peak associated to static order.

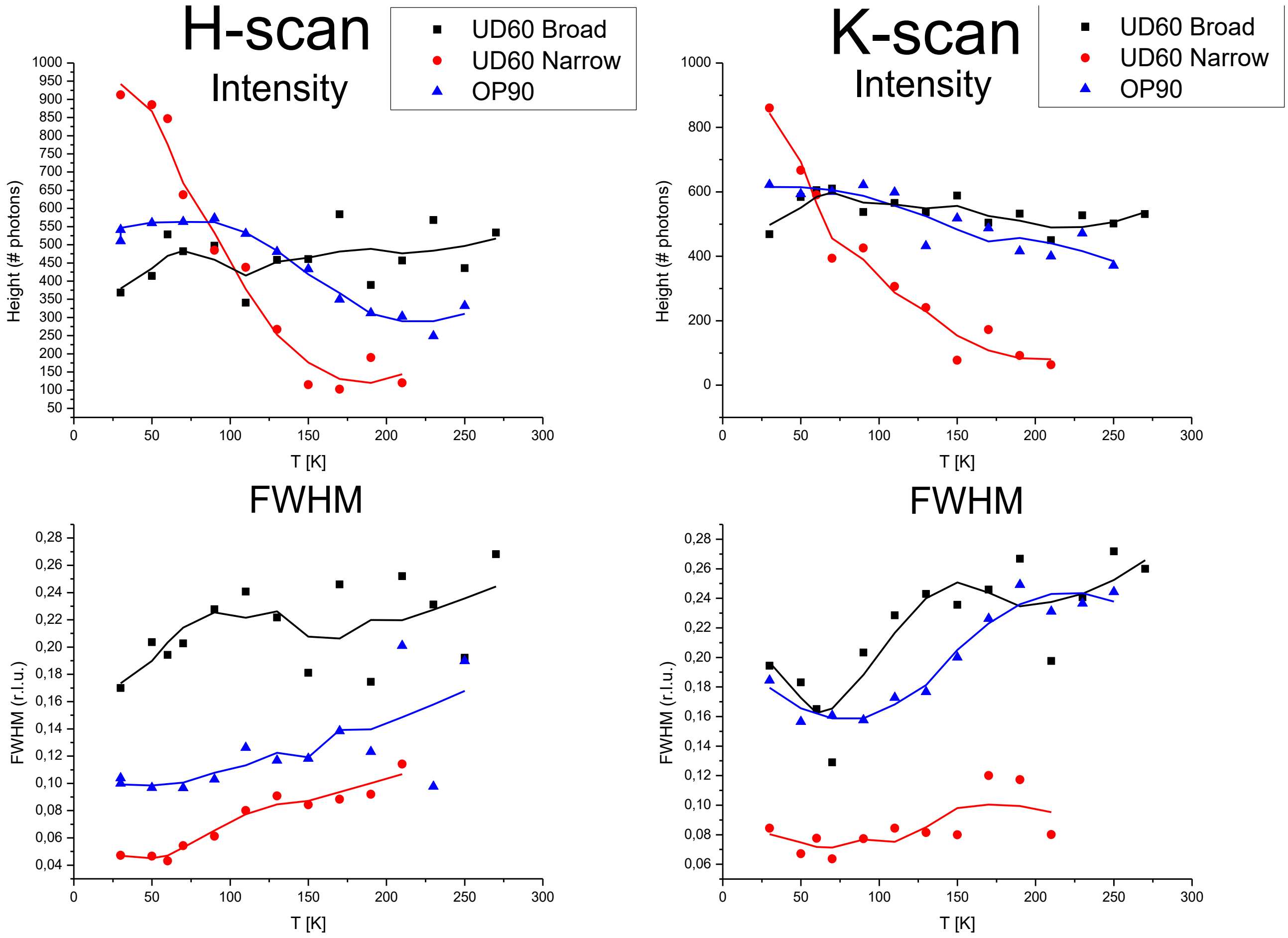

Figure 4.6: Fitting parameters of the NBCO. The column on the left shows the Intensity (the parameter H of Equation (4.2)) and the FWHM (the parameter Γ of Equation (4.2)) of the data regarding the H-scan, whereas the column on the right displays the same parameters for the K-scan. In the legend, we call the broadest of the two peaks of the UD60 "Broad" and the other "Narrow", while the OP90 is fitted with just one curve. The solid lines correspond to 7 points smoothing of the data shown.

We have enough information about the shape of the peak only for the NBCO, so we calculate the volume only for it. Figure 4.7 shows the results obtained for the two different dopings. The formula used for the volume of a peak is:

$$V = FWHM_H \cdot FWHM_K \cdot \sqrt{H_H \cdot H_K} \tag{4.3}$$

Where the subscripts H and K refer to the directions of the scan. For the OP90 there are no problems since only one peak is present. Thus, when we make the geometric average between the heights of the peak achieved in the scans along the two orthogonal directions, the formula is in principle correct, because in both cases they should coincide with the same maximum. For the UD60, where we have two peaks shifted along H, first we assume that $FWHM_K$ of the broad peak is right, even if it is measured at the value of H coinciding with the position of the maximum of the narrow peak and not of the broad peak as it should be. As mentioned above, the error should be negligible given the width of the broad peak compared to the distance between the two features. Second, we apply Equation (4.3) twice for the narrow and for the broad peak and finally we sum the results to obtain the total volume, as shown in Figure 4.7.

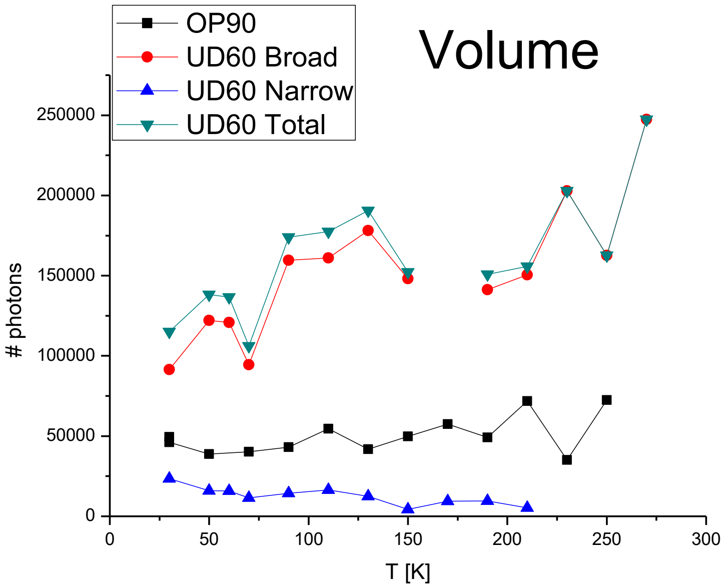

Figure 4.7: Volume of the peaks of NBCO. The point at 170 K is missing because the data are not reliable at that temperature. The Narrow peak decreases to zero with temperature, nevertheless the total volume of UD60 increases (besides the noise). This is due to the fact that by looking at the raw spectra in Figure 4.3, we give too much importance to the narrow peak, which instead being narrower in both directions, carries a way smaller spectral weight than the broad peak. The volume of OP90 seems to be almost constant with temperature.

For the YBCO it is not possible to calculate the volume: in fact, the first option for calculating the volume as done for the NBCO is not feasible, since we do not have the K-scan, which is necessary to have an approximated estimate of the asymmetry of the peak. Second, we cannot pretend that the peaks are symmetrical (see paragraph 1.2.3.2) and use the FWHM fitted in one scan for both the directions of the reciprocal space in which the peak extends. Third, for YBCO it is known that the peaks in the H and K directions are not equivalent [31], as confirmed by the intensity in Figure 4.8 whose maximum for the H-scan is ~1300 photons versus the ~650 photons of the K-scan. So, we cannot mix the information from the two scans to calculate the volume.

Moreover, this discrepancy is even bigger than what our data suggest, because also the charge order peak on the H axis splits in two spectral features along the K direction, thus we are actually measuring the intensity in between the two peaks, in a valley, achieving a smaller value than the real intensity. This is in good agreement with the experimental findings of Blanco-Canosa et al. [31] who demonstrated that in orthorhombic YBCO samples for doping levels bigger than p=0.12 (but still in the underdoped regime where the charge peak is present), the relation between the intensities of the peaks along H and K reverses compared to what happens at p<0.12, with the intensity of H taking over the one of K.

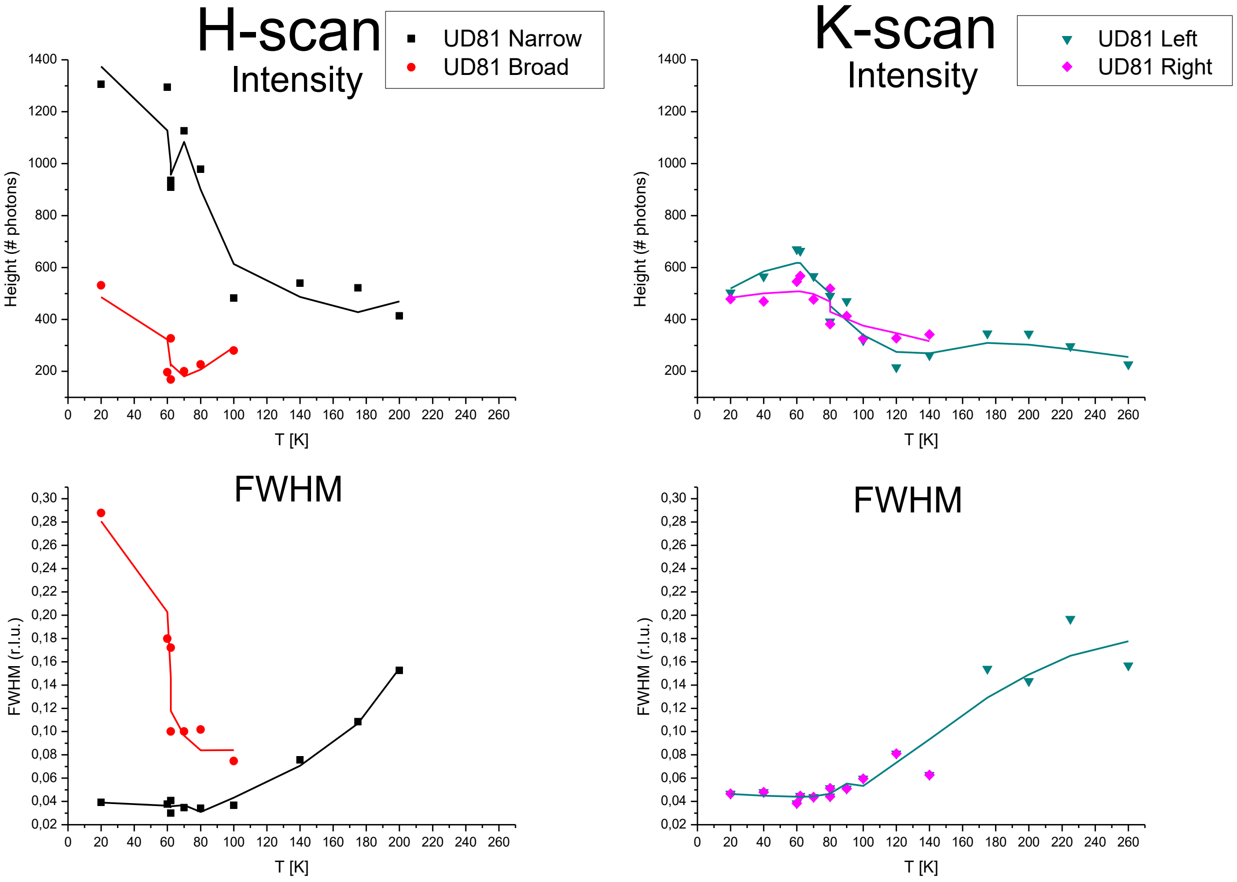

Figure 4.8: Fitting parameters of YBCO. Left: Intensity and FWHM retrieved by the fitting parameters of the H-scan. Right: Intensity and FWHM of the K-scan. In the K-scan the width of the two Lorentzian curve has been imposed to be equal so the points are overlapped, till the temperature of 140 K when the two peaks are not distinguishable anymore. Something reminding the anomaly at the critical temperature is visible in the K-scan parameters, since the intensity does not show a monotonic behavior and width seems to present a plateau at T_c=81 K. The solid lines correspond to 7 points smoothing of the data shown.

Figure 4.8 shows the results of the fitting achieved for the YBCO films. The H-scan does not present any clear indication of the relation between charge order and superconducting order. The narrow peak has an almost constant FWHM till the critical temperature while its intensity decreases steadily besides the noise. The trend shown by the broad peak is not easy to interpret especially due to the fact that upon increasing temperature the two peaks almost merge and it is not easy to disentangle the contributions related to each one of them. This effect does not influence so much the narrow peak because it is sharper and especially more intense. Indeed, slight changes on its position or FWHM combined with changes in the parameters of the straight line fitting the background, could result in a big impact on the partition of the spectral weight with the broad peak. The opposite instead is not so true as testified by the fact that the parameters of the narrow peak found when a fitting with two curves is performed, did not change greatly from the case in which a single curve is used (results not shown). Instead, in the K-scan parameters something reminding the anomaly at the critical temperature is visible, since the intensity does not show a monotonic behavior at low temperature (with a hint of a peak at a temperature slightly below T_c) and the width seems to present a plateau at Tc=81 K. Also here it is not so trivial to draw conclusions, because the two peaks present at low temperatures compete for the overall spectral weight and thus the trend seen in the intensity could be due to the tendency of one peak to steal signal from the other, together with the contribution of the tails coming from the gamma point not completely offset by the straight line used to simulate the background. This could be confirmed by the fact that in most cases the left peak, closer to the origin of the reciprocal space, is more intense than the peak on the left (see Figure 4.8). The choice to impose the widths of the two peaks to be equal mitigates this problem but does not completely solve it.

The next figure (Figure 4.9) shows the comparison of all the parameters of the Lorentzian curves used to fit the data from the three samples. This comparison is possible only along the H direction of the reciprocal space where the nature of the data is homogeneous. We can see that charge order along the H direction, is stronger in YBCO than in NBCO, as indicated by the higher intensity and by the narrower FWHM. Moreover, these characteristics should be even more relevant in a normal case when the spectral intensity of the YBCO is not divided between two different peaks.

In the 123 family, (at least for YBCO, see Figure 1.9) we expect the wavevector of the modulation to decrease with the doping. Here, for NBCO, this trend is not so clear due to the presence of a double peak in UD60. In particular, the position of the narrow peak of UD60 is located at higher wavevectors than that of OP90 while for the broad peak the opposite is true. A possible answer is that, if we assume a lower resolution not able to discern both the two peaks, the single curve used in this hypothetical case for the fitting, weighs more the sharper narrow peak located at higher wavevectors, thus confirming the usual trend. As said, while for NBCO the broad peak is positioned at lower q values than the narrow peak, the contrary is true for YBCO, in which the narrow peak is positioned closer to the origin that the broad peak. Furthermore, in this case the argument introduced above regarding the overall position of the charge order peak does not hold, since after a supposed loss of resolution, still the peak position would closely coincide with the position of the narrow peak found here: almost constant with temperature and slightly lower than 0.3 r.l.u..

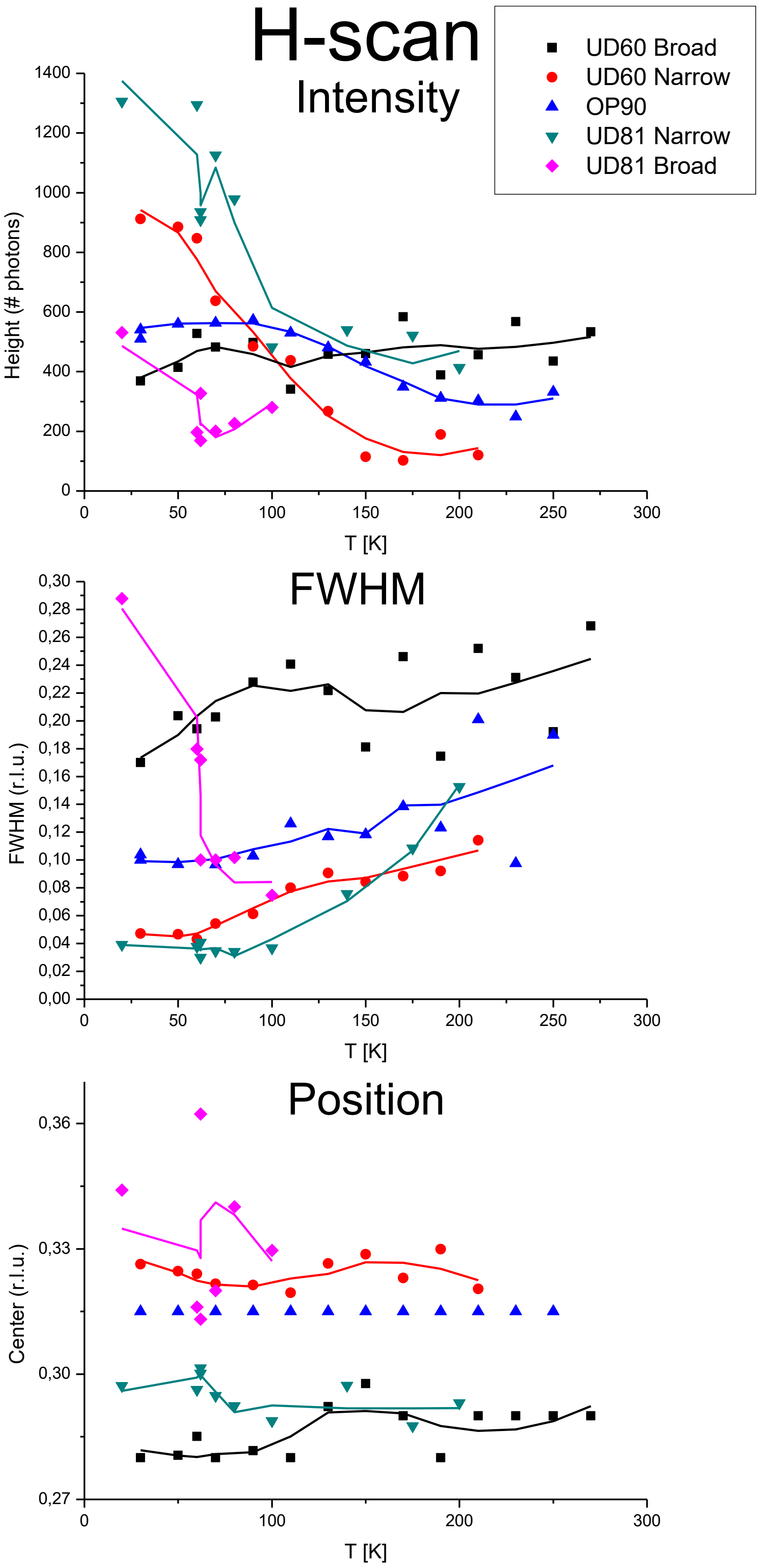

Figure 4.9: Overall comparison between the fitting parameters of the YBCO and NBCO for the H-scan direction in which the measurements are comparable. Note that after a preliminary fitting, which yielded an almost constant value for the position of the OP90 charge peak, we fixed the position in this material

to reduce the noise of the other parameters. The solid lines correspond to 7 points smoothing of the data shown.

The results shown in this chapter challenge the usual concept of onset temperature. On one side, the charge order in the samples of NBCO measured demonstrates evidences of its presence up to temperatures higher than what commonly thought for the onset temperature (see, Figure 1.4). Moreover, the intensity of the peaks analyzed does not indicate a clear reduction even at the highest temperatures (obviously, this is true only for the broad peak). This could hint that the "real" onset temperature could be located at even higher temperatures. This exceptional result has been possible thanks to the resolution capabilities of the ERIXS spectrometer. Actually, it must be pointed out that the onset temperature concept is an ill-posed problem (as suggested by Prof. Braicovich). In fact, the onset temperature is strongly dependent on the kind of probe used [3] (see Figure 4.1) and on the instrumental resolution available, since the key point is to find a signal going to zero and this task clearly depends on the signal to noise ratio of the instrument used. Nevertheless, our result show that the signal is stable and not going to zero up to 250 K. At this temperature though, the increase of the elastic background and of the width of the peak does not allow an easy analysis of the data. Possibly a larger portion of the reciprocal lattice, which completely encompasses the tails of the charge peak, should be spanned to have better results.

On the other side, we can find two different kinds of peaks, differentiated by their temperature behavior, by their width and by their volume. This result could maybe be linked to the work of Miao et al. [60], who demonstrated the presence, together with the normal charge order peak, of a CDW precursor peak in $La_{1.875}Ba_{0.125}CuO_4$. The relationship between this new spectral feature (the broad temperature independent peak) compared to the usual CDW signal (the narrow peak, visible only at low temperature) in LBCO, is similar to that demonstrated by our analysis in NBCO: the new peak is broader, lives till high temperatures and carries a greater amount of spectral density than the normal charge order peak. So, at first glance our results confirm this new experimental discovery also in NBCO.

Something that must be stressed is the fact that the intensity and the FWHM, retrieved by the analysis of the experimental data, do not show a precise behavior at T_c: the trends are not so well defined and the inversion of the strength of charge order below the critical temperature is not always so clear. A possible reason for this, could be the broadening of the superconducting transition caused by a deterioration of the samples. On the other side, it could also be possible that the broad fluctuating peak is truly independent of the superconducting critical temperature, in the same way it appears to separate from the pseudogap temperature T*. In any case, we remember that the assessment of the behavior around T_c, was not the major goal of the experiment, which principally aimed to determine an upper limit for the onset temperature of charge order in NBCO (in fact, as said, the data of YBCO come from another experiment and are put here just to give a richer view and as a possible source of comparison). Moreover, the T_c anomaly is not so clear due to the lack of experimental points around the critical temperature. Conversely the wide temperature range spanned allows to draw an exhaustive but general overview of the evolution of charge order with temperature.

The information collected during this experiment is also meant to test the different theoretical points of view. As already said, these data could be crucial to determine the intimate nature of the charge order in underdoped cuprates: an "epiphenomenon" of the Mott insulating state or a manifestation of a quantum critical behavior? Back in 2014, Blanco-Canosa et al. [31] already discussed the issue of quantum criticality affirming that the doping levels p_c and p_c' (see Figure 4.1) are not really quantum critical points since charge order never diverges. In reality, they should be projections on the B=0 plane of quantum critical points living in a 3D phase diagram, where after a certain critical field the charge order diverges. It is there that we can speak of real quantum critical points. What we actually see at zero field applied are just quantum critical fluctuations, whose inherent strength compared to the normal thermodynamic fluctuations [61], fosters charge order up to high temperatures in the phase diagram. Nonetheless, preliminary fitting of the charge order peaks with the theoretical model by Caprara et al. [3], show a good agreement between theory and experiments (Prof. Di Castro), hinting to quantum criticality as the possible explanation for the charge order instability.

4.3 Conclusions

In this section, we briefly stress the main points related to the experimental results described in this last chapter and we outline the most recent theoretical developments by the group of Prof. Grilli. The motivation behind this experiment is the precise evaluation of the temperature extension of charge order in the NBCO cuprate. The ubiquitous character of charge order in high temperature superconducting cuprates is well known, but there is still the open question of how it copes with the pseudogap regime (which is also a general feature of cuprates). The results demonstrate the presence of charge modulations well above the pseudogap temperature. Thus, the latter becomes just a crossover temperature, below which charge order gains strength. In particular, we found a dynamical fluctuating charge density wave peak persisting up to rather high temperatures. The charge order associated to this peak is short ranged and its fluctuating nature seems to be quite independent of the family of the cuprate measured. A possible way to explain the fluctuating behavior of charge order (associated to the broad temperature independent peak in the spectra), is related to a quantum critical point of view, which yields an inherently dynamical character for charge oscillations. Thus, the experimental data presented here are crucial to establish the realm of dynamical fluctuations in the temperature and doping variables. Concerning the temperature dependent, narrow peak, the possible reasons why it is quasi-static (and hence detectable by slow probing mechanisms) are quenched disorder, commensuration and surface effects and pinning (Prof. Grilli).

Another hint suggesting that the CDWs are not necessarily related to the pseudogap regime, comes from the work of Peng et al. on overdoped Bi2201 [26]. In fact, in this doped compound, strong and long-ranged charge fluctuations, persisting up to very high temperature, are found, even though the pseudogap temperature drops to zero in the region of the phase diagram probed. Moreover, for the optimally doped sample of NBCO reported here, where the pseudogap temperature is lower than in the underdoped regime, the temperature range measured during the experiment expands both above and below the pseudogap temperature. So, by looking at the analyzed data, we can say that the dynamical charge order is present up to temperatures well above the pseudogap temperature and that the latter marks only a crossover temperature below which the dynamical fluctuations become stronger. Owing to its fast interaction with the sample, RIXS is suitable to detect the dynamical fluctuating part of the charge order, which yields the information required to support or dismantle the most advanced theoretical scenarios and which constitutes the new contribution added by these data to the landscape of charge order in cuprates.

The last theoretical developments by the group of Prof. Grilli, suggest that the reason why a stronger charge order takes place in the underdoped region of all cuprates and in the particular case of the overdoped Bi2201 [26], is the enhancement of the electron density of states in these doping regimes. In fact, in the Bi2201 we have a Van Hove singularity for high doping levels, which provides a huge increase in the density of states available, while we have a similar increase in the density of states (owing to different reasons) throughout all the cuprates when the doping levels are decreased. The model used to explain charge order thus yields stronger fluctuations in these ranges of the phase diagram where more electronic states are available. If this theoretical explanation is the correct, as suggested by the experimental data collected, the dynamical behavior of the charge order could be connected to the quantum critical scenario, which predicts charge modulations up to temperatures well above the pseudogap temperature.

Bibliography

[1] W. McMillan, "Theory of discommensurations and the commensurate-incommensurate charge-density-wave phase transition," *Phys Rev B,* vol. 14, no. 4, pp. 1496-1502, 1976.

[2] "https://en.wikipedia.org/wiki/Charge_density_wave," [Online].

[3] S. Caprara, C. Di Castro, G. Seibold and M. Grilli, "Dynamical charge density waves rule the phase diagram of cuprates," *Phys Rev B,* vol. 95, p. 224511, 2017.

[4] J. M. Tranquada, B. J. Sternlieb, J. D. Axe, Y. Nakamura and S. Uchida, "Evidence for stripe correlations of spins and holes in copper oxide superconductors," *Nature,* vol. 375, pp. 561-563, 1995.

[5] G. Ghiringhelli, M. Le Tacon, M. Minola, S. Blanco-Canosa, C. Mazzoli, N. B. Brookes, G. M. De Luca, A. Frano, D. G. Hawthorn, F. He, T. Loew, M. Moretti Sala, D. C. Peets, M. Salluzzo, E. Schierle, R. Sutaro, G. A. Sawatzky, E. Weschke, B. Keimer and Braicovich, "Long-Range Incommensurate Charge Fluctuations in (Y,Nd)Ba2Cu3O6+x," *Science,* vol. 337, p. 821, 2012.

[6] A. Mesaros, K. Fujita, H. Eisaki, S. Uchida, J. Davis and al., "Topological Defects Coupling Smectic Modulations to Intra-Unit-Cell Nematicity in Cuprates," *Science*, vol. 333, pp. 426-430, 2011.

[7] J. G. Bednorz and K. A. Muller, "Possible high Tc superconductivity in the Ba-La-Cu-O system," *Zeitschrift fur Physik B Condensed Matter*, vol. 64, pp. 189-193, 1986.

[8] G. Dellea, Collective excitations in high temperature superconducting cuprates studied by resonant inelastic soft X-ray scattering, Politecnico di Milano, Doctoral program in physics, 2016.

[9] B. Keimer, S. A. Kivekson, M. R. Norman, S. Uchida and J. Zaanen, "From quantum matter to high-temperature superconductivity in copper oxides," *Nature,* vol. 518, no. 7538, pp. 179-186, 2015.

[10] R. Comin and A. Damascelli, "Resonant x-ray scattering studies of charge order in cuprates," *Annu Rev Condens Matter Phys,* vol. 7, pp. 369-405, 2016.

[11] M. Minola, "Charge fluctuations in the CuO2 planes of 123 cuprates," in *Magnetic, orbital and charge fluctuations in layered cuprates studied by resonant soft x-ray scattering*, 2013.

[12] T. Hanaguri, C. Lupien, Y. Kohsaka, D. Lee, M. Azuma and al., "A 'checkerboard' electronic crystal state in lightly hole-doped Ca2-xNaxCuO2Cl2," *Nature,* vol. 430, pp. 1001-1005, 2004.

[13] M. Vershinin, S. Misra, S. Ono, Y. Ando and A. Yazdani, "Local Ordering in the Pseudogap State of the High-Tc Superconductor Bi2Sr2CaCu2O8+δ," *Science,* vol. 303, pp. 1995-1998, 2004.

[14] K. Yamada and al., "Doping dependence of the spatially modulated dynamical spin correlations and the superconducting-transition temperature in La2-xBaxCuO4," *Phys Rev B,* vol. 58, pp. 6165-6172, 1998.

[15] G. Seibold and J. Lorenzana, "Doping dependence of spin excitations in the stripe phase of high-Tc superconductors," *Phys Rev B,* vol. 73, p. 144515, 2006.

[16] J. Lorenzana and G. Seibold, "Metallic mean-field stripes, incommensurability, and chemical potential in cuprates," *Phys Rev Lett*, vol. 89, p. 136401, 2002.

[17] J. Hoffman, E. Hudson, K. Lang, V. Madhavan, H. Eisaki and al., "A four unit cell periodic pattern of quasi-particle states surrounding vortex cores in Bi2Sr2CaCu2O8+δ," *Science,* vol. 295, pp. 466-469, 2002a.

[18] W. D. Wise, M. Boyer, K. Chatterjee, T. Kondo, T. Takeuchi and al., "Charge-density-wave origin of cuprate checkerboard visualized by scanning tunnelling microscopy," *Nat Phys,* vol. 4, pp. 696-699, 2008.

[19] D. LeBoeuf, N. Doiron-Leyraud, J. Levallois, R. Daou, J. Bonnemaison and al., "Electron pockets in the Fermi surface of hole-doped high Tc superconductors," *Nature,* vol. 450, pp. 533-536, 2007.

[20] T. Wu, H. Mayaffre, S. Kramer, M. Horvatic, C. Berthier and al., "Magnetic-field-induced charge-stripe order in the high-temperature supercoductor YBa2Cu3Oy," *Nature,* vol. 477, pp. 191-194, 2011.

[21] S. Gerber, H. Jang, H. Nojiri, S. Matsuzawa, H. Yasumura and al., "Three-Dimensional Charge Density Wave Order in YBa2Cu3O6.67 at High Magnetic Fields," *arXiv:1506.07910,* 2015.

[22] W. Tabis, Y. Li, M. Le Tacon, L. Braicovich, A. Kreyssig and al., "Connection between charge-density-wave order and charge transport in the cuprate superconductors," *Nat Comm,* vol. 5, p. 5875, 2014.

[23] E. Da Silva Neto, R. Comin, F. He, R. Sutarto, Y. Jiang and al., "Charge ordering in the electron-doped superconductor Nd2-xCexCuO4," *Science,* vol. 347, pp. 282-285, 2015.

[24] A. Chubukov, S. Sachdev and J. Ye, "Theory of two dimensional quantum Heisenberg antiferromagnets with a nearly critical groundstate," *Phys Rev B,* vol. 49, pp. 11919-11961, 1994.

[25] R. Comin, A. Frano, M. Yee, Y. Yoshida, H. Eisaki and al., "Charge Order Driven by Fermi-Arc Instability in Bi2Sr2-xLaxCuO6+δ," *Science,* vol. 343, pp. 390-392, 2014.

[26] Y. Y. Peng, R. Fumagalli, Y. Ding, M. Minola, D. Betto, G. M. De Luca, K. Kummer, E. Lefrancois, M. Salluzzo, H. Suzuki, M. Le Tacon, X. J. Zhou, N. B. Brookes, B. Keimer, L. Braicovich and G. Ghiringhelli, "Robust charge order in overdoped (Bi,Pb)2.12Sr1.88CuO6+δ outside the pseudogap regime," *Unpublished results,* 2017.

[27] R. Comin, R. Sutarto, F. He, E. Da Silva Neto, L. Chauviere and al., "Symmetry of charge order in cuprates," *Nat Mater,* vol. 14, pp. 796-800, 2015a.

[28] K. Fujita, M. Hamidian, S. Edkins, C. Kim, Y. Kohsaka and al., "Direct phase-sensitive identification of a d-form factor density wave in underdoped cuprates," *Proc Nat Acad Sci,* vol. 111, pp. E3026-E3032, 2014b.

[29] M. Hamidian, S. Edkins, C. Kim, J. Davis, A. Mackenzie and al., "Atomic-scale Electronic Structure of the Cuprate d-Symmetry Form Factor Density Wave State," *arXiv,* vol. 1507.07865, 2015.

[30] R. Comin, R. Sutarto, E. Da Silva Neto, L. Chauviere, R. Liang and al., "Broken translational and rotational symmetry via charge stripe order in underdoped YBa2Cu3O6+y," *Science,* vol. 347, pp. 1335-1339, 2015b.

[31] S. Blanco-Canosa, A. Frano, E. Schierle, J. Porras, T. Loew and al., "Resonant x-ray scattering study of charge-density wave correlations in YBa2Cu3O6+x," *Phys Rev B,* vol. 90, 2014.

[32] J. Chang, E. Blackburn, A. T. Holmes, N. B. Christensen, J. Larsen and al., "Direct observation of competition between superconductivity and charge density wave order in YBa2Cu3Oy," *Nat Phys,* vol. 8, no. 12, pp. 871-876, 2012.

[33] M. Hucker and al., "Stripe order in superconducting La2-xBaxCuO4 (0.095<=x<=0.155)," *Phys Rev B,* vol. 83, no. 10, pp. 104506-1 - 104506-16, 2011.

[34] J. He and al., "Observation of a Three-Dimensional Quasi-Long-Range Electronic Supermodulation in YBa2Cu3O7-X/La0.7Ca0.3MnO Heterostructures," *to appear in Nat Commun,* 2016.

[35] F. Lombardi, R. Arpaia, R. Baghdadi, T. Bauch, G. De Luca, M. Salluzzo, G. Ghiringhelli, Y. Peng and D. Stornaiuolo, "The effect of lateral confinement on charge order in nano-patterned RBCO superconductor," proposal ESRF, HC 2393, 2016.

[36] S. Nawaz, R. Arpaia, F. Lombardi and T. Bauch, "Microwave Response of Superconducting YBa2Cu3O7-δ Nanowire Bridges Sustaining the Critical Depairing Current: Evidence of Josephson-like Behavior," *Phys Rev Lett,* vol. 110, p. 167004, 2013.

[37] F. De Bergevin and M. Brunel, "Observation of magnetic superlattice peaks by X-ray diffraction on an antiferromagnetic NiO crystal," *Phys Lett A,* vol. 39, pp. 141-142, 1972.

[38] P. Abbamonte, L. Venema, A. Rusydi, G. Sawatzky, G. Logvenov and I. Bozovic, "A Structural Probe of the Doped Holes in Cuprates Superconductors," *Science,* vol. 297, pp. 581-584, 2002.

[39] P. Abbamonte, A. Rusydi, S. Smadici, G. Gu, G. Sawatzky and D. Feng, "Spatially modulated 'Mottness' in La2-xBaxCuO4," *Nat Phys,* vol. 1, pp. 155-158, 2005.

[40] A. Achkar, F. He, R. Sutarto, J. Geck, H. Zhang and al., "Resonant X-Ray Scattering Measurements of a Spatial Modulation of the Cu 3d and O 2p Energies in Stripe-Ordered Cuprate Superconductors," *Phys Rev Lett,* vol. 110, p. 017001, 2013.

[41] M. Blume, "Magnetic scattering of x rays," *Journ App Phys,* vol. 57, no. 8, 1998.

[42] M. P. M. Dean, "Insights into the high temperature superconducting cu-prates from resonant inelastic X-ray scattering," *Journal of Magnetism and Magnetic Materials,* vol. 376, pp. 3-13, 2015.

[43] Ament, J. Luuk and al., "Resonant inelastic x-ray scattering studies of elemen-tary excitations," *Reviews of Modern Physics,* vol. 83, no. 2, p. 705, 2011.

[44] H. H. Miao, J. Lorenzana, G. Seibold, Y. Y. Peng, A. Amorese, F. Yakhou-Harris and al., "Precursor Charge Density Waves and Spin-Charge Unlocking in La1.875Ba0.125CuO4," *arXiv,* 2017.

[45] L. Chaix, G. Ghiringhelli, Y. Y. Peng, M. Hashimoto, B. Moritz, K. Kummer, N. B. Brookes, Y. He and al., "Dispersive charge density wave excitations and temperature dependent commensuration in Bi2Sr2CaCu2O8+δ," *arXiv,* 2017.

[46] H. Bruus and K. Flensberg, Many-body quantum theory in condensed matter physics: An introduction, Oxford University Press, 2004.

[47] C. J. Jia and al., "Persistent spin excitations in doped antiferromagnets re-vealed by resonant inelastic light scattering," *Nature communications,* 2014.

[48] R. Fumagalli, "Resonant Inelastic X-ray Scattering of Iridium Fluorides," *Master thesis in Egineering Physics*, 2016.

[49] J. K. D. Vaughan, X-Ray Data Booklet, 2009.

[50] ESRF, "www.esrf.eu/about/synchrotron-science/synchrotron," [Online].

[51] M. Moretti Sala and al., "Energy and symmetry of dd excitations in undoped layered cuprates measured by Cu-L3 resonant inelastic x-ray scattering," *New Journal of Physics,* vol. 13, no. 4, 2011.

[52] F. Yakhou-Harris, K. Kummer, G. Berruyer, L. Braicovich, J. C. Cezar, F. Cianciosi, L. Eybert, P. Feder, A. Fondacaro, G. Ghiringhelli, E. Jimenez-Romero, M. Lemé, P. Marion, C. Ravary, L. Zhang and N. B. Brookes, "ID32 - The new ESRF soft X-ray beamline for spectroscopic studies with polarized light," *Poster contribution*, 2015.

[53] Sasaki, Shigemi and al., "Design of a new type of planar undulator for generat-ing variably polarized radiation," *Nuclear Instruments and Methods in Phys-ics Research Section A: Accelerators, Spectrometers, Detectors and Associat-ed Equipment,* vol. 331, no. 1, pp. 763-767, 1993.

[54] G. Ghiringhelli and al., "Saxes, a high resolution spectrometer for resonant x-ray emission in the 400–1600ev energy range," *Review of scientific instru-ments,* vol. 77, no. 11, p. 113108, 2006.

[55] V. N. Strocov and al., "High-resolution soft X-ray beamline ADRESS at the Swiss Light Source for resonant inelastic X-ray scattering and angle-resolved photoelectron spectroscopies," *Synchrotron Radiation,* vol. 17, no. 5, pp. 631-643, 2010.

[56] G. R. Hopkinson, "Charge diffusion effects in CCD x-ray detectors: I. Theory," *Nuclear Instruments and Methods in Physics Research,* vol. 216, no. 3, pp. 423-429, 1983.

[57] "http://www.cinel.com/," Cinel - Instruments for Research and Industry. [Online].

[58] L. Braicovich and al., "The simultaneous measurement of energy and linear polarization of the scattered radiation in resonant inelastic soft x-ray scat-tering," *Review of Scientific Instruments,* vol. 85, no. 11, p. 115104, 2014.

[59] G. Ghiringhelli and al., "What is the real onset temperature of CDW in Nd123?," proposal ESRF, HC 2999, 2017.

[60] H. Miao, J. Lorenzana, G. Seibold, Y. Y. Peng, A. Amorese, F. Yakhou-Harris, K. Kummer, B. N. B, R. M. Konik, V. Thampy, G. D. Gu, G. Ghiringhelli, L. Braicovich and M. P. M. Dean, "Precursor Charge Density Waves and Spin-Charge Unlocking in La1.875Ba0.125CuO4," *arXiv:1701.00022v3.*

[61] "https://en.wikipedia.org/wiki/Quantum_critical_point," [Online].

Acknowledgements

Here I want to thank all the people who helped me through my thesis and through the years at Politecnico.

First of all, I have to mention Prof. Ghiringhelli for the precious support he gave me (which I really appreciated), for all the things he taught me in this relatively brief but intense period of work together and for the opportunity of working in a team of world class researchers. Next I would like to thank Roberto for his advices and for the relation of friendship built up in these months. I cannot forget Dr. Peng and Prof. Braicovich, who guided and assisted me during my work. I express my gratitude also to Giacomo, who became my friend during the months spent together in the laboratory. To him I wish all the best for his thesis and for his future, being sure that with his skills he will achieve brilliant results.

At this point I need to thank my colleagues who became close friends during these five years together, sharing the same difficulties through this tough but beautiful path which I think gave us the possibility to grow intellectually and as persons.

Finally, I am grateful to all my friends and people who gave me the strength to pursue my objectives, which would mean nothing without them. In particular, among others, I want to say thank for everything to Federica, to my mother and my father, to Prof. Osculati, to Antonio, to Luca and Silvia.